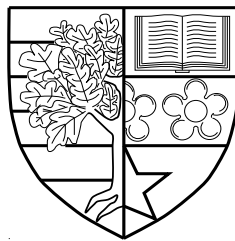


Massive MIMO Channel Modelling for 5G Wireless Communication Systems

by

Shangbin Wu



Submitted for the degree of Doctor of Philosophy
at

Heriot-Watt University

School of Engineering and Physical Sciences

October 2015

The copyright in this thesis is owned by the author. Any quotation from the thesis or use of any of the information contained in it must acknowledge this thesis as the source of the quotation or information.

Abstract

Massive Multiple-Input Multiple-Output (MIMO) wireless communication systems, equipped with tens or even hundreds of antennas, emerge as a promising technology for the Fifth Generation (5G) wireless communication networks. To design and evaluate the performance of massive MIMO wireless communication systems, it is essential to develop accurate, flexible, and efficient channel models which fully reflect the characteristics of massive MIMO channels. In this thesis, four massive MIMO channel models have been proposed.

First, a novel non-stationary wideband multi-confocal ellipse Two-Dimensional (2-D) Geometry Based Stochastic Model (GBSM) for massive MIMO channels is proposed. Spherical wavefront is assumed in the proposed channel model, instead of the plane wavefront assumption used in conventional MIMO channel models. In addition, the Birth-Death (BD) process is incorporated into the proposed model to capture the dynamic properties of clusters on both the array and time axes.

Second, we propose a novel theoretical non-stationary Three-Dimensional (3-D) wideband twin-cluster channel model for massive MIMO communication systems with carrier frequencies in the order of gigahertz (GHz). As the dimension of antenna arrays cannot be ignored for massive MIMO, nearfield effects instead of farfield effects are considered in the proposed model. These include the spherical wavefront assumption and a BD process to model non-stationary properties of clusters such as cluster appearance and disappearance on both the array and time axes.

Third, a novel Kronecker Based Stochastic Model (KBSM) for massive MIMO channels is proposed. The proposed KBSM can not only capture antenna correlations but also the evolution of scatterer sets on the *array axis*. In addition, upper and lower bounds of KBSM channel capacities in both the high and low Signal-to-Noise Ratio (SNR) regimes are derived when the numbers of transmit and receive antennas are increasing unboundedly with a constant ratio.

Finally, a novel unified framework of GBSMs for 5G wireless channels is proposed. The proposed 5G channel model framework aims at capturing key channel characteristics of certain 5G communication scenarios, such as massive MIMO systems, High Speed Train (HST) communications, Machine-to-Machine (M2M) communications, and Milli-meter Wave (mmWave) communications.

To my family and colleagues

Acknowledgments

I would like to express my special appreciation and thanks to my primary supervisor Prof. Cheng-Xiang Wang for his guidance and support. I would like to thank you for encouraging my research, for allowing me to grow as a researcher, and for providing me this precious opportunity to pursue a Ph.D. I am also grateful to my second supervisor, Prof. Harald Haas, from the University of Edinburgh, for his insightful discussions.

It is my great privilege to work with my colleagues in the Advanced Wireless Technologies (AWiTec) Group, namely, Yi Yuan, Ammar Ghazal, Yu Fu, Fourat Haider, Ahmed Al-Kinani, Piya Patcharamaneepakorn, Xian Yue Wu, Yan Zhang, and Qianru Zhou. Additionally, I would like to take this opportunity to thank members in the Wireless Research Group at Shandong University, namely, Lu Bai, Yu Liu, Jie Huang, Jiahua Song, Enqing Li, Rui Feng, Yanxin Wang, Weilun Qin, Andong Zhou, Wenzhe Qi, Yapei Zhang, Jisheng Sun, and Xiaoqing Zhang. I really enjoy the time we spent together. I thank all of you for sharing wonderful moments. I hope our friendship will last eternally.

I would also like to thank two teachers from School of Mathematical and Computer Sciences at Heriot-Watt University, including Dr. Martin Youngson for his functional analysis course and Dr. Seva Shneer for his advice on combinatorial mathematics.

Last, my special gratitude goes to my family for their unconditional love and infinite encouragement. Thank you all for supporting me in all my pursuits.

Shangbin Wu

Edinburgh, September 2015.

Declaration of Authorship

I, Shangbin Wu, declare that this thesis titled, ‘Massive MIMO Channel Modelling for 5G Wireless Communication Systems’ and the work presented in it are my own. I confirm that:

- This work was done wholly while in candidature for a research degree at Heriot-Watt University.
- Where I have consulted the published work of others, this is always clearly attributed.
- Where I have quoted from the work of others, the source is always given. With the exception of such quotations, this thesis is entirely my own work.
- I have acknowledged all main sources of help.
- Where the thesis is based on work done by myself jointly with others, I have made clear exactly what was done by others and what I have contributed myself.

Signed:

Date:

Contents

Abstract	i
Acknowledgments	iii
Declaration of Authorship	iv
List of Figures	ix
List of Tables	xiii
Abbreviations	xiv
Symbols	xviii
1 Introduction	1
1.1 Background	1
1.1.1 The 5G wireless communication systems	1
1.1.2 The role of massive MIMO in 5G	3
1.2 Motivation	5
1.3 Contributions	6
1.4 Original Publications	7
1.5 Thesis Organisation	9
2 MIMO Channel Modelling: Literature Review	11
2.1 Introduction	11
2.2 GBSMs	12
2.2.1 2-D GBSMs	12
2.2.2 3-D GBSMs	14
2.3 CBSMs	16
2.3.1 i.i.d. Rayleigh fading channel model	16

2.3.2	KBSM	16
2.3.3	Weichselberger channel model	17
2.3.4	VCR	17
2.4	Channel Measurements for Massive MIMO	18
2.4.1	Capacity	18
2.4.2	Spherical wavefront and non-stationarities	19
2.4.3	Eigenvalue properties	20
2.4.4	Other channel characteristics	21
2.4.5	Challenges on massive MIMO channel measurements	21
2.5	Research Gap	22
2.6	Summary	23
3	A Non-Stationary 2-D Ellipse Model for Massive MIMO Channels	24
3.1	Introduction	24
3.2	A Wideband Ellipse Model for Massive MIMO Systems	27
3.2.1	Array axis evolution—generation of cluster sets C_l^T and C_k^R	32
3.2.2	Space CCF analysis	36
3.3	Array-Time Evolution Model	37
3.4	A Wideband Ellipse Simulation Model for Massive MIMO	44
3.5	Numerical Analysis	45
3.6	Summary	52
4	A Non-Stationary 3-D Twin-Cluster Model for Massive MIMO Channels	53
4.1	Introduction	53
4.2	A Theoretical Non-Stationary 3-D Wideband Twin-Cluster Massive MIMO Channel Model	55
4.2.1	Channel impulse response	57
4.2.1.1	For NLOS components	58
4.2.1.2	For LOS component	60
4.2.2	Non-stationary properties	60
4.2.2.1	Survived clusters	65
4.2.2.2	Newly generated clusters	66
4.3	Statistical Properties of the Theoretical Massive MIMO Channel Model	66
4.3.1	STCF	66
4.3.2	Space CCF	67
4.3.3	Time ACF	68
4.3.4	Doppler PSD	69
4.3.5	Doppler frequency standard deviation on the antenna array	69
4.3.6	Condition number	70
4.4	A Non-Stationary 3-D Wideband Twin-Cluster Simulation Model for Massive MIMO Channels	70
4.5	Numerical Results and Analysis	72
4.6	Summary	78

5	A Novel KBSM for 5G Massive MIMO Channels	80
5.1	Introduction	80
5.2	System Model	81
5.2.1	Conventional KBSM	82
5.2.2	Proposed KBSM–BD–AA	83
5.2.3	Discussions	85
5.3	Channel Capacity Analysis	85
5.3.1	Low SNR approximation	86
5.3.1.1	Capacity upper bound ($\rho \rightarrow 0$)	87
5.3.1.2	Capacity lower bound ($\rho \rightarrow 0$)	87
5.3.2	High SNR approximation	88
5.3.2.1	Capacity upper bound ($\rho \rightarrow \infty$)	89
5.3.2.2	Capacity lower bound ($\rho \rightarrow \infty$)	89
5.4	Results and Discussions	91
5.5	Summary	93
6	A Unified Framework for 5G Wireless Channel Models	95
6.1	Introduction	95
6.1.1	Related work I: GBSMs for massive MIMO	96
6.1.2	Related work II: GBSMs for M2M and HST	96
6.1.3	Related work III: GBSMs for mmWave	97
6.1.4	Contributions	97
6.2	A Unified Framework for 5G Wireless Channel Models	98
6.2.1	Channel impulse response	102
6.2.2	Array-time cluster evolution for the unified 5G GBSM framework	105
6.2.3	Generation of new clusters	106
6.2.4	Evolution of survived clusters	108
6.2.5	Adaptation to scenarios	109
6.3	Statistical Property Analysis	111
6.3.1	Time-variant PDP	111
6.3.2	Stationary interval	111
6.3.3	Time-variant transfer function	112
6.3.4	STFCF	112
6.4	Results and Analysis	114
6.5	Summary	120
7	Conclusions and Future Work	121
7.1	Summary of Results	121
7.1.1	GBSMs for massive MIMO channels	121
7.1.2	KBSM for massive MIMO channels	122
7.1.3	A unified framework for 5G channel models	123
7.2	Future Research Directions	123
7.2.1	COST 2100 model for massive MIMO channels	123
7.2.2	Map-based massive MIMO channels	124

7.2.3	Correlation-based massive MIMO channel model	125
7.2.4	Standardised 5G channel model	125
 A Antenna Pattern Calculation		126
 B Time Evolution of Ray Mean Powers		128
 References		130

List of Figures

1.1	A diagram of massive MIMO systems.	4
2.1	Classification of MIMO stochastic channel models.	12
2.2	APS of massive MIMO [1, Fig. 6].	20
3.1	A wideband multi-confocal ellipse model for massive MIMO systems.	27
3.2	Cluster generation algorithm flowchart.	34
3.3	An example of random shuffling and pairing between the transmitter and receiver cluster indices.	35
3.4	Geometrical relationship evolution from $t = t_m$ to $t = t_{m+1}$ of the ellipse model.	38
3.5	Normalised Doppler PSD of the theoretical model, the simulation model, and simulations. ($M_R = 32, M_T = 1, t = 1\text{s}, a_1 = 100\text{m}, f = 80\text{m}, D_c^a = 30\text{m}, D_c^s = 50\text{m}, \beta_R = \beta_T = \pi/2, \lambda = 0.12\text{m}, f_{\max} = 33.33\text{Hz}, \alpha_v = \pi/6, \kappa = 9, \bar{\alpha}_n^R = \pi/3, \text{NLOS}$).	46
3.6	Absolute receiver space CCF $ \rho_{k1,k'1,1}(0, \delta_R; t) $ of the ellipse model under von Mises assumption in terms of different values of (k', k) pairs with $ k' - k = 1$. ($M_R = 32, M_T = 1, t = 1\text{s}, a_1 = 100\text{m}, f = 80\text{m}, D_c^a = 30\text{m}, D_c^s = 50\text{m}, \beta_R = \beta_T = \pi/2, \lambda = 0.12\text{m}, f_{\max} = 33.33\text{Hz}, \alpha_v = \pi/6, \kappa = 5, \bar{\alpha}_n^R = \pi/3, \text{NLOS}$).	46
3.7	Absolute space CCF $ \rho_{11,22,1}(\delta_T, \delta_R; t) $ of the ellipse model. ($M_R = M_T = 32, t = 1\text{s}, a_1 = 100\text{m}, f = 80\text{m}, D_c^a = 30\text{m}, D_c^s = 50\text{m}, \beta_R = \beta_T = \pi/2, \lambda = 0.15\text{m}, f_{\max} = 33.33\text{Hz}, \alpha_v = \pi/6, \kappa = 5, \text{NLOS}$).	47
3.8	An example of cluster evolution on the receive antenna array. (A '*' symbol in the two dimensional plane means its corresponding antenna element (coordinate on the horizontal direction) is able to observe its corresponding cluster (coordinate on the vertical direction).)	48
3.9	A snapshot example of the normalised angle power spectrum of AoA of the wideband ellipse model. ($M_R = 32, M_T = 1, a_1 = 100\text{m}, f = 80\text{m}, D_c^a = 30\text{m}, D_c^s = 50\text{m}, \beta_R = \beta_T = \pi/2, \lambda = 0.15\text{m}, \delta_R = 0.5\lambda, f_{\max} = 0\text{Hz}, \text{NLOS}, \lambda_G = 80/\text{m}, \lambda_R = 4/\text{m}, P_F = 0.3$).	49

3.10	A snapshot example of the normalised angle power spectrum of AoA of the wideband ellipse model. ($M_R = 32, M_T = 1, a_1 = 100\text{m}, f = 80\text{m}, D_c^a = 30\text{m}, D_c^s = 50\text{m}, \beta_R = \beta_T = \pi/2, \lambda = 0.15\text{m}, \delta_R = 0.5\lambda, f_{\max} = 0\text{Hz}, \text{LOS } K = 3\text{dB}, \lambda_G = 32/\text{m}, \lambda_R = 4/\text{m}, P_F = 0.3$).	49
3.11	Cumulative distribution function of average life periods of clusters on the array axis in terms of normalised antenna spacing. ($D_c^a = 30\text{m}, D_c^s = 50\text{m}, \lambda = 0.15\text{m}, \delta_R = 0.5\lambda, \text{NLOS}, \lambda_G = 80/\text{m}, \lambda_R = 4/\text{m}, P_F = 0.3$).	50
3.12	Cumulative distribution function of the maximum power difference over the antenna array under different LOS/NLOS conditions and correlation factors on array and space axes. ($M_R = 32, M_T = 1, a_1 = 100\text{m}, f = 80\text{m}, \beta_R = \beta_T = \pi/2, \lambda = 0.15\text{m}, \delta_R = 0.5\lambda, f_{\max} = 0\text{Hz}$, von Mises distributed AoA).	50
3.13	Absolute receiver space CCF $ \rho_{11,21,1}(0, \delta_R; t) $ of the wideband ellipse model. ($M_R = 32, M_T = 1, t = 1\text{s}, a_1 = 100\text{m}, f = 80\text{m}, D_c^a = 15\text{m}, D_c^s = 50\text{m}, \beta_R = \beta_T = \pi/2, \lambda = 0.15\text{m}, \delta_R = 0.5\lambda, f_{\max} = 0\text{Hz}, \text{NLOS}, \lambda_G = 80/\text{m}, \lambda_R = 4/\text{m}, P_F = 0.3, \kappa = 5$).	51
3.14	Absolute time ACF of Cluster ₁ $ \rho_{11,1}(\Delta t; t) $ in (3.56) comparison between $t = 1\text{s}$ and $t = 4\text{s}$ with BD process. ($M_R = 32, M_T = 32, a_1 = 100\text{m}, f = 80\text{m}, D_c^a = 15\text{m}, D_c^s = 50\text{m}, \beta_R = \beta_T = \pi/2, \lambda = 0.15\text{m}, \delta_R = \delta_T = 0.5\lambda, f_{\max} = 33.33\text{Hz}, v_c = 0.5\text{m/s}, \text{NLOS}, \lambda_G = 80/\text{m}, \lambda_R = 4/\text{m}, P_F = 0.3, \kappa = 5$).	51
3.15	Absolute FCF $ \rho_{11}(\Delta \xi; t) $ comparison between NLOS and LOS. ($M_R = 32, M_T = 32, a_1 = 100\text{m}, f = 80\text{m}, D_c^a = 15\text{m}, D_c^s = 50\text{m}, \beta_R = \beta_T = \pi/2, \lambda = 0.15\text{m}, \delta_R = \delta_T = 0.5\lambda, f_{\max} = 33.33\text{Hz}, v_c = 0.5\text{m/s}, \lambda_G = 80/\text{m}, \lambda_R = 4/\text{m}, P_F = 0.3, \kappa = 5$).	52
4.1	A 3-D wideband twin-cluster massive MIMO channel model.	57
4.2	Algorithm flowchart of the generation of the channel impulse response.	60
4.3	Algorithm flowchart of array-time evolution of the proposed 3-D twin-cluster model.	61
4.4	Absolute values of the space CCF $ \rho_{11,22,1}(\delta_T, \delta_R; t) $ of the 3-D twin-cluster model. ($M_R = M_T = 32, D = 200\text{m}, D_c^a = 30\text{m}, D_c^s = 50\text{m}, v_A^T = \pi/3, v_E^T = \pi/6, v_A^R = \pi/4, v_E^R = \pi/4, \bar{\theta}_1^T = -1.03, \bar{\xi}_1^T = 1.19, \bar{\theta}_1^R = 1.65, \bar{\xi}_1^R = 0.16, t = 4\text{s}, \lambda = 0.15\text{m}, f_{\max} = 33.33\text{Hz}, \alpha_v = \pi/6, \kappa = 5, \text{NLOS}$).	73
4.5	Absolute values of the receiver space CCF $ \rho_{11,12,1}(0, \delta_R; t) $ in terms of cluster elevation angles at the receiver side. ($M_R = 32, D = 200\text{m}, D_c^a = 30\text{m}, D_c^s = 50\text{m}, \varsigma = 1\text{s}, v_A^T = \pi/3, v_E^T = \pi/6, v_A^R = \pi/4, v_E^R = \pi/4, \bar{\theta}_1^T = -1.03, \bar{\xi}_1^T = 1.19, \bar{\theta}_1^R = 1.65, t = 4\text{s}, \lambda = 0.15\text{m}, f_{\max} = 33.33\text{Hz}, \alpha_v = \pi/6, \kappa = 5, \text{NLOS}$).	74
4.6	Absolute values of the time ACF $ \rho_{11,1}(\Delta t; t) $ in terms of cluster elevation angle at the receiver side ($M_R = 32, D = 200\text{m}, D_c^a = 30\text{m}, D_c^s = 50\text{m}, \varsigma = 1\text{s}, v_A^T = \pi/3, v_E^T = \pi/6, v_A^R = \pi/4, v_E^R = \pi/4, \bar{\theta}_1^T = -1.03, \bar{\xi}_1^T = 1.19, \bar{\theta}_1^R = 1.65, t = 4\text{s}, \lambda = 0.15\text{m}, \ \mathbf{v}_n^T\ = \ \mathbf{v}_n^R\ = 0.25\text{m/s}, P_F = 0.3, f_{\max} = 33.33\text{Hz}, \alpha_v = \pi/6, \kappa = 5, \text{NLOS}$).	75

4.7	The normalised Doppler PSD at different time instants ($M_R = 32$, $D = 200\text{m}$, $D_c^a = 30\text{m}$, $D_c^s = 50\text{m}$, $\varsigma = 1\text{s}$, $v_A^T = \pi/3$, $v_E^T = \pi/6$, $v_A^R = \pi/4$, $v_E^R = \pi/4$, $\bar{\theta}_1^T = -1.03$, $\bar{\xi}_1^T = 1.19$, $\bar{\theta}_1^R = 1.65$, $\lambda = 0.15\text{m}$, $\lambda_G = 80\text{m}$, $\lambda_R = 4\text{m}$, $\ \mathbf{v}_n^T\ = \ \mathbf{v}_n^R\ = 0.25\text{m/s}$, $P_F = 0.3$, $f_{\max} = 33.33\text{Hz}$, $\alpha_v = \pi/6$, $\kappa = 5$, NLOS).	75
4.8	Standard deviation of the Doppler frequencies on the antenna array ($D = 200\text{m}$, $D_c^a = 30\text{m}$, $D_c^s = 50\text{m}$, $\varsigma = 1\text{s}$, $v_A^T = \pi/3$, $v_E^T = \pi/6$, $v_A^R = \pi/4$, $v_E^R = \pi/4$, $\bar{\theta}_1^T = -1.03$, $\bar{\xi}_1^T = 1.19$, $\bar{\theta}_1^R = 1.65$, $\bar{\xi}_1^R = 0.16$, $\lambda = 0.15\text{m}$, $\ \mathbf{v}_n^T\ = \ \mathbf{v}_n^R\ = 0.25\text{m/s}$, $P_F = 0.3$, $f_{\max} = 33.33\text{Hz}$, $\alpha_v = \pi/6$, $\kappa = 5$, NLOS).	76
4.9	Comparisons of CDFs of condition numbers between the 2-D and 3-D model ($M_T = 4$, $M_R = 32$, $D = 200\text{m}$, $D_c^a = 30\text{m}$, $D_c^s = 50\text{m}$, $\varsigma = 1\text{s}$, $v_A^T = \pi/3$, $v_E^T = \pi/6$, $v_A^R = \pi/4$, $v_E^R = \pi/4$, $\bar{\theta}_1^T = -1.03$, $\bar{\xi}_1^T = 1.19$, $\bar{\theta}_1^R = 1.65$, $t = 4\text{s}$, $\lambda = 0.15\text{m}$, $\lambda_G = 80\text{m}$, $\lambda_R = 4\text{m}$, $\ \mathbf{v}_n^T\ = \ \mathbf{v}_n^R\ = 0.25\text{m/s}$, $P_F = 0.3$, $f_{\max} = 33.33\text{Hz}$, $\alpha_v = \pi/6$, $\kappa = 5$, NLOS).	76
4.10	A snap shot of the angular power spectrum of the receiver antenna array ($M_T = 1$, $M_R = 32$, $D = 200\text{m}$, $D_c^a = 30\text{m}$, $D_c^s = 50\text{m}$, $\varsigma = 1\text{s}$, $v_A^T = \pi/3$, $v_E^T = \pi/6$, $v_A^R = \pi/4$, $v_E^R = \pi/4$, $\bar{\theta}_1^T = -1.03$, $\bar{\xi}_1^T = 1.19$, $\bar{\theta}_1^R = 1.65$, $t = 4\text{s}$, $\lambda = 0.15\text{m}$, $\lambda_G = 80\text{m}$, $\lambda_R = 4\text{m}$, $f_{\max} = 0\text{Hz}$, NLOS).	77
4.11	Cluster evolution on the time axis ($D_c^s = 50\text{m}$, $\varsigma = 1\text{s}$, $\lambda = 0.15\text{m}$, $\lambda_G = 80\text{m}$, $\lambda_R = 4\text{m}$, $\ \mathbf{v}_n^T\ = \ \mathbf{v}_n^R\ = 0.25\text{m/s}$, $P_F = 0.3$, $f_{\max} = 33.33\text{Hz}$, NLOS).	78
5.1	Diagram of scatterer set evolution on the array axis for massive MIMO.	84
5.2	Number of scatterers shared with Antenna 1 in terms of antenna indices (100 initial scatterers in Antenna 1).	91
5.3	Antenna spatial correlation for the KBSM-BD-AA (isotropic scattering environment).	92
5.4	Capacity analysis in the low SNR regime for the KBSM-BD-AA ($M_R = M_T = 64$).	92
5.5	Capacity analysis in the high SNR regime for the KBSM-BD-AA ($M_R = M_T = 64$, half-wavelength ULAs, isotropic scattering environment).	93
5.6	CDFs of capacities of the KBSM-BD-AA with different values of β (SNR=25dB, $M_R = M_T = 64$, half-wavelength ULAs, isotropic scattering environment).	94
6.1	A unified framework of a 3-D 5G GBSM.	100
6.2	Flowchart of the array-time cluster evolution for the proposed unified 5G GBSM framework.	105
6.3	Pseudo codes for the new cluster generation algorithm.	108
6.4	Diagram of combinations of scenarios from the proposed unified 5G GBSM framework.	110

6.5	Comparison between the normalised ACFs of Cluster ₁ and Cluster ₂ of the normal wideband conventional MIMO channel model ($f_c = 2\text{GHz}$, $\ \mathbf{D}\ = 200\text{m}$, $M_R = M_T = 2$, $\delta_R = \delta_T = 0.5\lambda$, $\Delta v^R = \Delta v^T = 0\text{m/s}$, $ \mathbf{v}^T = 0, \mathbf{v}^R = 5\text{m/s}$, $v_E^T = \frac{\pi}{6}$, $v_A^T = \frac{\pi}{3}$, $v_E^R = v_A^R = \frac{\pi}{4}$, $D_c^a = 50\text{m}$, $M_1 = M_2 = 81$, $\varsigma = 7\text{s}$, NLOS).	115
6.6	Receiver normalised space CCFs of F2F normal wideband 3-D massive MIMO channel model and measurement in [1] ($f_c = 2.6\text{GHz}$, $\ \mathbf{D}\ = 200\text{m}$, $M_R = M_T = 32$, $\delta_R = \delta_T = 0.5\lambda$, $\Delta v^R = \Delta v^T = 0\text{m/s}$, $ \mathbf{v}^T = \mathbf{v}^R = 0$, $v_E^T = \frac{\pi}{4}$, $v_A^T = \frac{\pi}{3}$, $v_E^R = v_A^R = \frac{\pi}{4}$, $D_c^a = 30\text{m}$, $\kappa = -8\text{dB}$, polarised antennas, NLOS).	116
6.7	CCDFs of the HST normal wideband 3-D conventional MIMO channel model and measurement in [2] ($f_c = 932\text{MHz}$, $\ \mathbf{D}\ = 200\text{m}$, $M_R = M_T = 2$, $\Delta v^R = \Delta v^T = 0.5\text{m/s}$, $\ \mathbf{v}^R\ = 60\text{m/s}$, $\ \mathbf{v}^T\ = 0\text{m/s}$, $v_E^T = \frac{\pi}{4}$, $v_A^T = \frac{\pi}{3}$, $v_E^R = v_A^R = \frac{\pi}{4}$, $D_c^a = 100\text{m}$, $\varsigma = 7\text{s}$).	116
6.8	CDF of 90% coherence bandwidth of the M2M normal wideband 2-D conventional MIMO channel model and measurement (suburban scenario) in [3] ($f_c = 5.9\text{GHz}$, $\ \mathbf{D}\ = 400\text{m}$, $\Delta v^R = \Delta v^T = 0.5\text{m/s}$, $\ \mathbf{v}^T\ = \ \mathbf{v}^R\ = 25\text{m/s}$, $v_A^R = v_E^R = \frac{\pi}{4}$, $v_A^T = \frac{\pi}{3}$, $v_E^R = \frac{\pi}{4}$, $D_c^s = 10\text{m}$, $\varsigma = 5\text{s}$).	117
6.9	A snapshot of simulated normalized APS at the receiver of the mmWave 2-D massive MIMO channel model ($f_c = 58\text{GHz}$, $M_T = 2$, $M_R = 32$, $\ \mathbf{D}\ = 6\text{m}$, $\delta_R = \delta_T = 0.5\lambda$, $\Delta v^R = \Delta v^T = 0\text{m/s}$, $ \mathbf{v}^T = \mathbf{v}^R = 0$, $v_E^T = \frac{\pi}{4}$, $v_A^T = \frac{\pi}{3}$, $v_E^R = v_A^R = 0$, $D_c^a = 30\text{m}$, $D_c^s = 100\text{m}$, NLOS).	118
6.10	CCDFs of RMS delay spread of the F2F mmWave 3-D conventional MIMO channel model and measurement in [4] ($f_c = 58\text{GHz}$, $\ \mathbf{D}\ = 6\text{m}$, $\Delta v^R = \Delta v^T = 0\text{m/s}$, $\ \mathbf{v}^T\ = \ \mathbf{v}^R\ = 0\text{m/s}$, $v_A^R = v_E^R = \frac{\pi}{4}$, $v_A^T = \frac{\pi}{3}$, $v_E^T = \frac{\pi}{4}$, $D_c^s = 100\text{m}$, $\varsigma = 7\text{s}$).	118
6.11	Comparison of normalized channel capacities of the unified GBSM framework for massive MIMO channel models with normal and polarized antennas ($M_R = 8$, $M_T = 32$, $f_c = 2\text{GHz}$, $\ \mathbf{D}\ = 100\text{m}$, $v_A^R = \frac{\pi}{4}$, $v_A^T = \frac{\pi}{3}$, $D_c^s = 100\text{m}$, $\varsigma = 7\text{s}$, $v_E^R = \frac{\pi}{4}$, $v_E^T = \frac{\pi}{4}$, $\kappa = -8\text{dB}$).	119
6.12	Comparison of normalized channel capacities of massive MIMO channel models ($M_R = 8$, $M_T = 32$, $f_c = 2\text{GHz}$, $\ \mathbf{D}\ = 100\text{m}$, $v_A^R = \frac{\pi}{4}$, $v_A^T = \frac{\pi}{3}$, $D_c^s = 100\text{m}$, $\varsigma = 7\text{s}$, $v_E^R = \frac{\pi}{4}$ (3-D models only), $v_E^T = \frac{\pi}{4}$ (3-D models only)).	120
A.1	Diagram of LCS and GCS in the 3-D space.	126

List of Tables

2.1	Recent advances in massive MIMO channel measurements	19
3.1	Summary of key parameter definitions for the 2-D ellipse model.	29
4.1	Definitions of key geometry parameters for the 3-D twin-cluster model.	56
4.2	Distributions of key geometry parameters for the 3-D twin-cluster model.	63
6.1	Definitions of key geometry parameters for the 3-D 5G GBSM.	100
6.2	Distributions of Parameters of Clusters for the 3-D 5G GBSM.	107
6.3	Simulation parameters for different scenarios.	114

Abbreviations

2-D	Two-Dimensional
3-D	Three-Dimensional
3GPP	Third Generation Partnership Project
4G	Fourth Generation
5G	Fifth Generation
ACF	Autocorrelation Function
AoA	Angle of Arrival
AoD	Angle of Departure
APS	Angular Power Spectrum
ASA	Authorized Shared Access
AWGN	Additive White Gaussian Noise
BD	Birth-Death
BER	Bit Error Rate
BS	Base Station
CBSM	Correlation Based Stochastic Model
CCDF	Complementary Cumulative Distribution Function
CCF	Cross-Correlation Function
CDF	Cumulative Distribution Function
COST	European Cooperative in Science and Technology

CP	Cyclic Prefix
CSI	Channel State Information
DFT	Discrete Fourier Transform
E2E	End-to-End
F2F	Fixed-to-Fixed
F2M	Fixed-to-Mobile
FBMC	Filter Bank Multi-Carrier
FCF	Frequency Correlation Function
FDD	Frequency Division Duplex
FPGA	Field-Programmable Gate Array
GBSM	Geometry Based Stochastic Model
GCS	Global Coordinate System
HST	High Speed Train
i.i.d.	Independent and Identically Distributed
ICI	Inter-Channel Interference
IEEE	Institute of Electrical and Electronics Engineers
IMT-A	International Mobile Telecommunications Advanced
KBSM	Kronecker Based Stochastic Model
KBSM-BD-AA	KBSM with BD process on the array axis
KPIs	Key Performance Indicators
LCS	Local Coordinate System
LLN	Law of Large Numbers
LLS	Link Level Simulation

LOS	Line-of-Sight
LTE	Long Term Evolution
LTE-A	LTE-Advanced
M2M	Machine-to-Machine
MAC	Medium-Access Control
MBCM	Map-Based Channel Model
MCM	Monte Carlo Method
MEA	Method of Equal Area
MED	Method of Equal Distances
MEDS	Method of Exact Doppler Spread
METIS	Mobile and wireless communications Enablers for Twenty-twenty Information Society
MIMO	Multiple-Input Multiple-Output
mmWave	Milli-meter Wave
MS	Mobile Station
MU-MIMO	Multi-User MIMO
multi-RATs	multiple Radio Access Technologies
MUSIC	MUltiple Signal Classification
NLOS	Non-LOS
OFDM	Orthogonal Frequency Division Multiplexing
PAN	Personal Area Network
PDF	Probability Density Function
PDP	Power Delay Profile
PSD	Power Spectral Density
RF	Radio Frequency
RMS	Root Mean Square

SCM	Spatial Channel Model
SCME	SCM-Extension
SLS	System Level Simulation
SNR	Signal-to-Noise Ratio
STCF	Space-Time Correlation Function
STFCF	Space-Time-Frequency Correlation Function
SV	Saleh-Valenzuela
TDD	Time Division Duplex
TVD	Traffic Volume Density
UE	User Equipment
ULAs	Uniform Linear Arrays
US	Uncorrelated Scattering
V2V	Vehicle-to-Vehicle
VCR	Virtual Channel Representation
VRs	Visibility Regions
WiMAX	Worldwide Interoperability for the Microwave Access
WINNER	Wireless World Initiative New Radio
WINNER+	WINNER Phase +
WLAN	Wireless Local Area Network
WSS	Wide Sense Stationary

Symbols

$(\cdot)^T$	transpose of a matrix/vector
$(\cdot)^H$	Hermitian transpose of a matrix/vector
$\ \cdot\ $	Euclidean norm
$\max\{\cdot\}$	maximum value of a set
$\min\{\cdot\}$	minimum value of a set
$E[\cdot]$	statistical expectation
$J_0(\cdot)$	zeroth-order Bessel function of first kind
$I_0(\cdot)$	zeroth-order modified Bessel function
\otimes	Kronecker product of matrices
\cup	union of sets
\cap	intersection of sets
\sum	summation
$\text{card}(\cdot)$	cardinality of a set
\xrightarrow{E}	evolution on either the array or time axis
$\langle \cdot, \cdot \rangle$	inner product
$\text{trace}(\cdot)$	trace of a matrix
Pr	probability measure
\circ	Hadamard product
$\det(\cdot)$	determinant of a matrix
$\lambda_{\max}(\cdot)$	maximum eigenvalue of a matrix
$\lambda_{\min}(\cdot)$	minimum eigenvalue of a matrix

$\zeta(\cdot)$	dispersion of a matrix
M_T	number of transmit antennas
M_R	number of receive antennas
δ_T	antenna spacing of transmit antennas
δ_R	antenna spacing of receive antennas
Ant_l^T	the l th transmit antenna
Ant_k^R	the k th receive antenna
Cluster_n	the n th cluster
f_c	carrier frequency
c	speed of light
t	time
τ	delay
\mathcal{L}	dimension of an antenna array
f	semi focal length in the 2-D ellipse model
a_n	semi-major axis of the n -th ellipse
$\beta_T(\beta_R)$	tilt angles of the transmit (receive) antenna array
f_{\max}	maximum Doppler frequency
λ	carrier wavelength
κ	width control parameter of the von Mises distribution
α_v	direction of the receiver movement
D_{kl}^{LOS}	LOS distance between Ant_k^R and Ant_l^T in the 2-D ellipse model
$D_{ln,i}^T$	distance between Cluster_n and Ant_l^T via the i th ray in the 2-D ellipse model
$D_{kn,i}^R$	distance between Cluster_n and Ant_k^R via the i th ray in the 2-D ellipse model
$D_{n,i}^T$	distance between Cluster_n and the transmit array via the i th ray in the 2-D ellipse model
$D_{n,i}^R$	distance between Cluster_n and the receive array via the i th ray in the 2-D ellipse model
f_{kl}^{LOS}	Doppler frequency of the LOS component between Ant_k^R and Ant_l^T
$f_{n,i}$	Doppler frequency of Cluster_n via the i th ray
$\varphi_{kl}^{\text{LOS}}$	phase of the LOS component between Ant_k^R and Ant_l^T

$\varphi_{kl,n,i}$	phase of Cluster _{<i>n</i>} between Ant _{<i>k</i>} ^{<i>R</i>} and Ant _{<i>l</i>} ^{<i>T</i>} via the <i>i</i> th ray
$\alpha_{n,i}^T$	AoD of the <i>i</i> th ray of Cluster _{<i>n</i>} to the transmit array center
$\alpha_{n,i}^R$	AoA of the <i>i</i> th ray of Cluster _{<i>n</i>} to the receive array center
C_l^T	cluster set of Ant _{<i>l</i>} ^{<i>T</i>}
C_k^R	cluster set of Ant _{<i>k</i>} ^{<i>R</i>}
N_{total}	total number of clusters observable to at least one transmit and one receive antenna
H	channel coefficient matrix
φ_0	initial signal phase
K	LOS Rician factor
P_n	mean power of Cluster _{<i>n</i>}
τ_n	delay of Cluster _{<i>n</i>}
h_{kl}	complex gain between Ant _{<i>k</i>} ^{<i>R</i>} and Ant _{<i>l</i>} ^{<i>T</i>}
$h_{kl,n}$	complex gain of Cluster _{<i>n</i>} between Ant _{<i>k</i>} ^{<i>R</i>} and Ant _{<i>l</i>} ^{<i>T</i>}
$\varphi_{kl}^{\text{LOS}}$	phase of LOS component between Ant _{<i>k</i>} ^{<i>R</i>} and Ant _{<i>l</i>} ^{<i>T</i>}
D_l^{LOS}	phase of LOS component between Ant _{<i>l</i>} ^{<i>T</i>} and the receive array center
α_l^{LOS}	AoA of LOS component from Ant _{<i>l</i>} ^{<i>T</i>} and the receive array center
λ_G	generation rate of new clusters
λ_R	recombination rate of existing clusters
P_F	percentage of moving clusters
D_c^a	scenario-dependent correlation factor on the array axis
D_c^s	scenario-dependent correlation factor on the space axis
P_{survival}^T	survival probabilities of the clusters on the array axis at the transmitter
P_{survival}^R	survival probabilities of the clusters on the array axis at the receiver
N_{new}^T	number of newly generated clusters at the transmitter
N_{new}^R	number of newly generated clusters at the receiver
$\varphi_{c,n}$	movement direction of Cluster _{<i>n</i>} in the 2-D ellipse model
v_c	velocity of Cluster _{<i>n</i>} in the 2-D ellipse model
v	velocity of the receiver in the 2-D ellipse model
q_m	channel fluctuation measure at time instant t_m in the 2-D ellipse model
H_{kl}	transfer function of the channel in the 2-D ellipse model

$\Delta\xi$	frequency difference
Δt	time difference
Δp_{\max}^R	maximum received power difference on the receive array axis
Cluster_n^T	representative of Cluster_n at the transmitter in the 3-D twin-cluster model
Cluster_n^R	representative of Cluster_n at the receiver in the 3-D twin-cluster model
\mathbf{D}	distance vector between the transmitter and receiver in the 3-D twin-cluster model
v_E^T	elevation angle of the transmit antenna array in the 3-D twin-cluster model
v_E^R	elevation angle of the receive antenna array in the 3-D twin-cluster model
v_A^T	azimuth angle of the transmit antenna array in the 3-D twin-cluster model
v_A^R	azimuth angle of the receive antenna array in the 3-D twin-cluster model
ξ_{n,i_1}^R	elevation angle of the i_1 -th ray of Cluster_n at the receiver side in the 3-D twin-cluster model
θ_{n,i_1}^R	azimuth angle of the i_1 -th ray of Cluster_n at the receiver side in the 3-D twin-cluster model
ξ_{n,i_2}^T	elevation angle of the i_2 -th ray of Cluster_n at the transmitter side in the 3-D twin-cluster model
θ_{n,i_2}^T	azimuth angles of the i_2 -th ray of Cluster_n at the transmitter side in the 3-D twin-cluster model
\mathbf{D}_n^R	distance vector between Cluster_n and the receiver
\mathbf{D}_n^T	distance vectors between Cluster_n and the transmitter
\mathbf{D}_{n,i_1}^R	distance vector between Cluster_n and the receive array via the i_1 -th ray
\mathbf{D}_{kn,i_1}^R	distance vector between Cluster_n and Ant_k^R via the i_1 -th ray
\mathbf{D}_{n,i_2}^T	distance vector between Cluster_n and the transmit array via the i_2 -th ray
\mathbf{D}_{ln,i_2}^T	distance vector between Cluster_n and Ant_l^T via the i_2 -th ray
$\mathbf{D}_{kl}^{\text{LOS}}$	distance vector between Ant_k^R and Ant_l^T
\mathbf{v}	velocity vector of the receive antenna array
$\mathbf{v}_n^R, \mathbf{v}_n^T$	velocity vectors of Cluster_n at the receiver and transmitter side
\mathbf{A}_k^R	the k th receive antenna vector
\mathbf{A}_l^T	the l th transmit antenna vector

$\tilde{\tau}_n$	virtual delay of Cluster _{<i>n</i>}
τ_{\max}	maximum delay
ς	coherence parameter of a virtual link in the 3-D twin-cluster model
\mathbf{y}	received signal vector in the KBSM-BD-AA
\mathbf{s}	symbol vector in the KBSM-BD-AA
\mathbf{n}	AWGN vector in the KBSM-BD-AA
\mathbf{R}_T	overall spatial correlation matrix of the transmitter in the KBSM-BD-AA
\mathbf{R}_R	overall spatial correlation matrix of the receiver in the KBSM-BD-AA
\mathbf{B}_T	spatial correlation matrix of the transmitter in the KBSM-BD-AA
\mathbf{B}_R	spatial correlation matrix of the receiver in the KBSM-BD-AA
\mathbf{E}_T	survival probability matrix of the transmitter in the KBSM-BD-AA
\mathbf{E}_R	survival probability matrix of the receiver in the KBSM-BD-AA
\mathbf{H}_w	zero mean unit variance i.i.d. Gaussian matrix in the KBSM-BD-AA
β	parameter describing how fast a scatterer disappears on the array axis in the KBSM-BD-AA
$\frac{E_b}{N_0}$	energy per bit to noise ratio
S_0	slope of channel capacity in the low SNR regime
ρ	SNR in the KBSM-BD-AA
ϕ_n^E	central elevation angle between Cluster _{<i>n</i>} and the receive array in the unified framework
ϕ_n^A	central azimuth angle between Cluster _{<i>n</i>} and the receive array in the unified framework
φ_n^E	central elevation angle between Cluster _{<i>n</i>} and the transmit array in the unified framework
φ_n^A	central azimuth angle between Cluster _{<i>n</i>} and the transmit array in the unified framework
ϕ_{n,m_n}^E	central elevation angle between the m_n th ray of Cluster _{<i>n</i>} and the receive array in the unified framework
ϕ_{n,m_n}^A	central azimuth angle between the m_n th ray of Cluster _{<i>n</i>} and the receive array

	in the unified framework
φ_{n,m_n}^E	central elevation angle between the m_n th ray of Cluster _{n} and the transmit array in the unified framework
φ_{n,m_n}^A	central azimuth angle between the m_n th ray of Cluster _{n} and the transmit array in the unified framework
f_{qn,m_n}^R	Doppler frequencies of Ant _{q} ^{R} via Cluster _{n} and the m_n th ray in the unified framework
f_{pn,m_n}^T	Doppler frequencies of Ant _{p} ^{T} via Cluster _{n} and the m_n th ray in the unified framework
\mathbf{v}^R	3-D velocity vector of the receive array in the unified framework
\mathbf{v}^T	3-D velocity vector of the transmit array in the unified framework
\mathbf{v}_n^R	3-D velocity vector of the last bounce of Cluster _{n} in the unified framework
\mathbf{v}_n^T	3-D velocity vector of the first bounce of Cluster _{n} in the unified framework
P_{n,m_n}	mean power of the m_n th ray of Cluster _{n} in the unified framework
$N(t)$	time variant number of clusters in the unified framework
M_n	number of rays within Cluster _{n} in the unified framework
τ_{m_n}	relative delay of the m_n th ray within Cluster _{n} in the unified framework
Φ_0	initial phase in the unified framework
Φ_{qp}^{LOS}	phase of the LOS component between Ant _{p} ^{T} and Ant _{q} ^{R} in the unified framework
τ^{LOS}	phase of the LOS component in the unified framework
h_{qp,n,m_n}	complex gain of the m_n th ray in Cluster _{n} between Ant _{q} ^{R} and Ant _{p} ^{T} in the unified framework
Φ_{qp,n,m_n}	phase of the m_n th ray in Cluster _{n} between Ant _{q} ^{R} and Ant _{p} ^{T} in the unified framework

Chapter 1

Introduction

1.1 Background

1.1.1 The 5G wireless communication systems

It is the demand for high-speed reliable communications with significantly improved user experience that drives the development of the Fifth Generation (5G) wireless communication networks. It has been widely accepted that the capacity of 5G wireless communication systems should achieve 1000 times larger than the Fourth Generation (4G) Long Term Evolution (LTE)/LTE-Advanced (LTE-A) wireless communication system [5]–[7]. Also, spectral efficiency is required to reach 10 times with respect to current 4G LTE-A, which is equivalent to 10 Gbps peak data rate for low mobility users and 1 Gbps peak data rate for high mobility users. The Mobile and wireless communications Enablers for Twenty-twenty Information Society (METIS) project even expects 10 to 100 times higher data rates for typical users [7].

In addition to the conventional spectral efficiency requirements, other Key Performance Indicators (KPIs) have been considered in the design of 5G wireless communication networks. To enable longer battery lifetime for devices, energy efficiency, which measures the transmitted bit per Joule, needs to be improved by 10 times [5]. The Traffic Volume Density (TVD) describes data throughput per unit area. It was

reported in [7] and [8] that the goal for 5G is to increase the TVD by a factor of 1000. The ability to process a massive number of devices will be compulsory as there will be billions of connected devices in the 5G wireless communication network by 2020 [9]. The 5 times reduced End-to-End (E2E) latency will play an important role in improving user experience [9]. It is also anticipated that coexistence of multiple Radio Access Technologies (multi-RATs) is inevitable in 5G wireless communication networks [5]–[12]. In this case, the use of unlicensed spectrum will be more efficient [10]. Moreover, more scenarios such as High Speed Train (HST) communications, Machine-to-Machine (M2M) communications, and low power massive machine communication will be supported in 5G. In order to satisfy the above-mentioned requirements, advanced technologies such as advanced multiple access schemes, more spectrum, denser small cells, and high-efficiency multiple antenna techniques will be key components of 5G wireless communication networks [9]–[11].

It was reported in [10] that the Filter Bank Multi-Carrier (FBMC), an enhanced version of Orthogonal Frequency Division Multiplexing (OFDM), would be an enabling technology for 5G air interface. Each subcarrier in FBMC will be filtered by a pulse shaping filter, so that the overhead of guard band for FBMC can be reduced. Additionally, FBMC can operate without Cyclic Prefix (CP) to handle multi-path fading channels [10].

The employment of more spectrum is three-fold. First, authors in [11] suggested that underutilised allocated spectrum should be prevented. Second, spectrum flexibility can be improved by Authorized Shared Access (ASA) which is optimal for small cells and using unpaired spectrum allocations [9]. Third, higher frequency bands such as Milli-meter Wave (mmWave) bands are able to provide large bandwidths for 5G wireless communication systems [5], [10].

Denser smaller cells bring the network closer to every user. Therefore, the data rate of the network can be boosted. The application of denser small cells is straightforward and effective, which has attracted the attentions of many wireless vendors [5], [9]–[12].

Multiple antenna techniques have attracted researchers' attention for its capability of providing diversity gain, multiplexing gain, and beamforming gain without extra

spectral resources [13]. Advanced 4G wireless communication systems such as World-wide Interoperability for the Microwave Access (WiMAX) [14] and LTE-A [15] have incorporated multiple antenna techniques.

1.1.2 The role of massive MIMO in 5G

Multiple-Input Multiple-Output (MIMO) technology has been attracting researchers' attention for its capability of providing improved link reliability and system capacity without extra spectral resources [13], [16]–[18]. MIMO has been deployed in a number of advanced wireless communication systems such as WiMAX [14] and LTE. The latest LTE standard (Release-12) [19], for instance, can support up to 8-layer transmission which is equivalent to at least 8 antennas at the Base Station (BS) and 8 antennas at the mobile station Mobile Station (MS).

Recently, massive MIMO technology [20] has appealed to many researchers due to its promising capability of greatly improving spectral efficiency, energy efficiency, and robustness of the system. In a massive MIMO system, both the transmitter and receiver are equipped with a large number of antenna elements (typically tens or even hundreds) as illustrated in Fig. 1.1. It should be noticed that the transmit antennas can be co-located or distributed in different applications. Also, the enormous number of receive antennas can be possessed by one device or distributed to many devices. A massive MIMO system can not only enjoy the benefits of conventional MIMO systems, but also significantly enhance both spectral efficiency and energy efficiency [21]–[23], because Inter-Channel Interference (ICI) is averaged in massive MIMO when the number of antennas is sufficiently large according to the Law of Large Numbers (LLN). Hence, channel capacity can be achieved even with simple match filtering beamforming or receiver [23]. Furthermore, as reported in [22], a massive MIMO system can be built with low-cost components because the linear requirement of the antenna amplifiers is low when each antenna is assigned with less power. By properly using Multi-User MIMO (MU-MIMO) in massive MIMO systems, the Medium-Access Control (MAC) layer design can be simplified by avoiding complicated scheduling algorithms. Consequently, these main advantages enable the

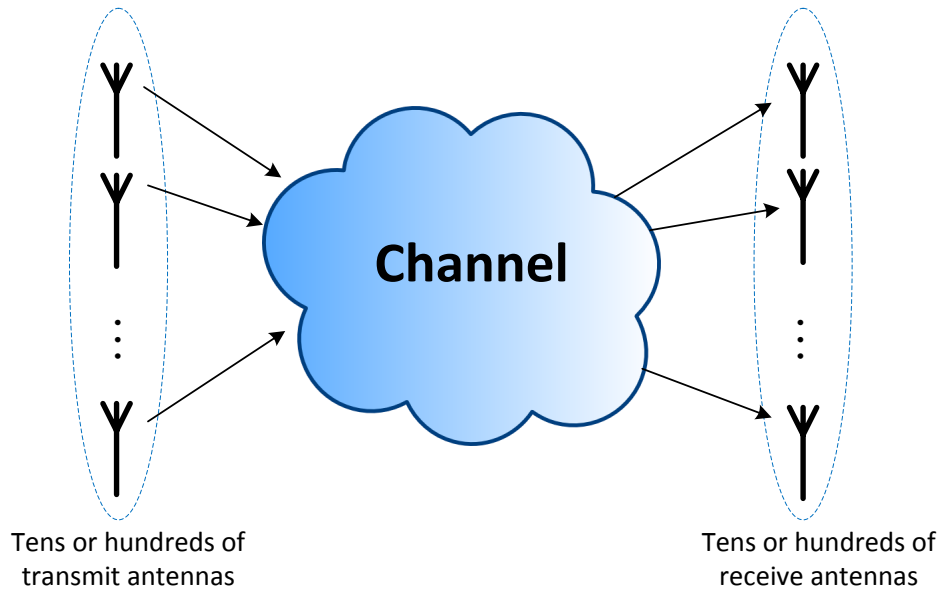


FIGURE 1.1: A diagram of massive MIMO systems.

massive MIMO system to be a promising candidate for the 5G wireless communication networks [24]–[27].

Although massive MIMO systems can offer many advantages, there are several major challenges that have to be addressed before their practical deployment. First, it is essential for the transmitter to acquire the Channel State Information (CSI) to fully enjoy the capacity gain offered by massive MIMO systems, especially for multi-user scenarios. However, as the number of antennas increases, the overhead of acquiring CSI grows accordingly. This issue can be partially solved in a Time Division Duplex (TDD) system which reduces the overhead of CSI by utilizing the reciprocity of the channel [23]. On the other hand, applications of massive MIMO to Frequency Division Duplex (FDD) systems is still an open problem under discussion. Second, in [23] it was pointed out that the complexity of precoding and detection will rise with the number of antennas. When the number of transmit antennas is much larger than the number of receive antennas, simple linear precoders and detectors are sufficient to offer nearly optimal performance. However, when the number of transmit antennas is comparable to or less than the number of receive antennas, the design of precoders and detectors with reasonable complexity becomes more challenging. Third, how we can squeeze a large number of antennas into a limited area/volume while still maintaining low

correlations remains open. Cube arrays can save space to form compact transceivers [28]. However, it was shown that only antennas on the surface of a cube array can contribute to the channel capacity gain [29]. Finally, since the increase of antennas at the transceivers introduces new phenomenon such as nearfield effects and non-stationary effects [1], conventional MIMO channel models such as the Wireless World Initiative New Radio (WINNER) II [30] and European Cooperative in Science and Technology (COST) 2100 [31]–[33] channel models fail to capture these features and therefore, cannot be directly used as massive MIMO channel models.

1.2 Motivation

To design and evaluate the performance of massive MIMO wireless communication systems, accurate and efficient channel models capturing key characteristics of massive MIMO channels are indispensable. However, certain key characteristics of massive MIMO channels such as the nearfield effect and non-stationary behaviors of cluster on the array axis are missing in existing conventional MIMO channel models. In other words, these conventional MIMO channel models are not sufficiently accurate for performance evaluation of massive MIMO wireless communication systems.

Wireless communication researchers may have diverse requirements on the wireless channel models. More accurate channel models are required for practical wireless system design and simulation. Efficient and mathematically tractable channels are useful for theoretical analysis.

Therefore, the motivation of this Ph.D project is to develop massive MIMO channel models, which are able to extract key channel characteristics, to satisfy different purposes, i.e., a more accurate channel model with the geometry-based approach for wireless communication system simulations and a more mathematically tractable channel model with the correlation-based approach for theoretical analysis.

1.3 Contributions

The key contributions of the thesis are summarised as follows:

- Review recent advances on channel measurements for massive MIMO, summarise and classify recent advances on existing stochastic models for MIMO channels.

Research on a non-stationary 2-D GBSM for massive MIMO channels

- Propose a novel non-stationary wideband Two-Dimensional (2-D) ellipse model for massive MIMO channels. The Angle of Arrival (AoA) and Angle of Departure (AoD) of each cluster are assumed dependent. Spherical wavefront is considered in the proposed model. The impacts of spherical wavefront assumption on both the Line-of-Sight (LOS) component and Non-LOS (NLOS) components are studied.
- Apply the Birth-Death (BD) process to both the array and time axes. Array-time evolution of clusters of the proposed wideband massive MIMO channel model is proposed. A novel cluster evolution algorithm is developed based on the BD process on both the array and time axes.
- Statistical properties of the proposed massive MIMO channel model such as Space-Time-Frequency Correlation Function (STFCF) and Cumulative Distribution Function (CDF) of survival probabilities of clusters and received power imbalance on the antenna array are investigated.

Research on a non-stationary 3-D GBSM for massive MIMO channels

- Propose a novel non-stationary wideband Three-Dimensional (3-D) twin-cluster model for massive MIMO channels. The impacts of elevation angles on statistical properties are investigated.

- Study the standard deviation of Doppler frequencies on the large antenna array as well as condition number of the proposed massive MIMO channel model.

Research on a novel KBSM for massive MIMO channels

- Propose a novel KBSM with BD process on the array axis (KBSM-BD-AA) for massive MIMO channels. This model is able to capture the BD process of clusters on the array axis.
- Perform channel capacity analysis of the proposed KBSM-BD-AA in both the high and low Signal-to-Noise Ratio (SNR) regimes.

Research on a unified framework for 5G wireless channel modelling

- Propose a unified Geometry Based Stochastic Model (GBSM) framework for 5G wireless channels. The proposed unified framework is sufficiently flexible to adapt to various typical scenarios in 5G wireless networks, such as HST communications, M2M communications, and mmWave communications.
- Incorporate the WINNER II channel model, the Saleh-Valenzuela (SV) channel model, and array-time evolution to establish the proposed unified framework.
- Fit statistical properties of the proposed unified framework to reported measurements.

1.4 Original Publications

This Ph.D project has led to the following publications:

Refereed Journals Papers

1. **S. Wu**, C.-X. Wang, H. Haas, el-H. M. Aggoune, M. M. Alwakeel, and B. Ai, “A non-stationary wideband channel model for massive MIMO communication

- systems,” *IEEE Trans. Wireless Commun.*, vol. 14, no. 3, pp. 1434–1446, Mar. 2015.
2. **S. Wu**, C.-X. Wang, el-H. M. Aggoune, M. M. Alwakeel, and Y. He, “A non-stationary 3-D wideband twin-cluster model for 5G massive MIMO channels,” *IEEE J. Sel. Areas Commun.*, vol. 32, no. 6, pp. 1207–1218, June 2014.
 3. **S. Wu**, C.-X. Wang, el-H. M. Aggoune, M. M. Alwakeel, and X. H. You, “A unified framework for 5G wireless channel models,” *IEEE Trans. Wireless Commun.*, 2015, submitted for publication.
 4. P. Patcharamaneepakorn, **S. Wu**, C.-X. Wang, el-H. M. Aggoune, M. M. Alwakeel, and M. Di Renzo, “Spectral, energy and economic efficiency of 5G multi-cell massive MIMO systems with generalized spatial modulation,” *IEEE Trans. Veh. Technol.*, 2015, submitted for publication.
 5. C.-X. Wang, **S. Wu**, L. Bai, X. H. You, J. Wang, and C. -L. I, “Recent advances and future challenges on massive MIMO channel measurements and models,” *Science China Information Sciences.*, 2015, submitted for publication.

Refereed Conferences Papers

1. **S. Wu**, C.-X. Wang, el-H. M. Aggoune, M. M. Alwakeel, and Y. Yang, “A novel Kronecker-based stochastic model for massive MIMO channels,” in *Proc. ICC’15*, Shenzhen, China, accepted for publication.
2. **S. Wu**, P. Patcharamaneepakorn, C. -X. Wang, el-H. M. Aggoune, M. M. Alwakeel, and Y. He, “A novel method for ergodic sum rate analysis of spatial modulation systems with maximum likelihood receiver,” invited paper, in *Proc. IWCMC’15*, Dubrovnik, Croatia, Aug. 2015, accepted for publication.
3. **S. Wu**, C.-X. Wang, A. Bo, and Y. He, “Capacity analysis of finite scatterer MIMO wireless channels,” in *Proc. ICC’14*, Sydney, Australia, June 2014, pp. 4559–4564.

4. **S. Wu**, C.-X. Wang, and el-H. M. Aggoune, “Non-stationary wideband channel models for massive MIMO systems,” in *Proc. WSCN’13*, Jeddah, Saudi Arabia, Dec. 2013, pp. 1–8.
5. **S. Wu**, C.-X. Wang, and Y. Yang, “Performance comparison of massive MIMO channel models,” in *Proc. ICC’16*, Kuala Lumpur, Malaysia, submitted for publication.

1.5 Thesis Organisation

The remainder of this thesis is organised as follows:

Chapter 2 provides literature review on stochastic models for wireless MIMO fading channels. Two approaches known as GBSM and Correlation Based Stochastic Model (CBSM) are discussed and classified. In this thesis, both GBSMs and CBSMs for massive MIMO channels will be developed, with focus on GBSMs. Also, recent advances on massive MIMO channel measurements will be reviewed, showing key channel characteristics of massive MIMO channels.

Chapter 3 investigates a non-stationary 2-D wideband ellipse model for massive MIMO channels. The array-time evolution of clusters is introduced. Statistical properties of the channel model such as AoA Angular Power Spectrum (APS), CDF of maximum power difference over the antenna array, and Frequency Correlation Function (FCF) are analysed.

Chapter 4 proposes a non-stationary 3-D wideband twin-cluster model for 5G massive MIMO channels. The array-time evolution of clusters is applied to the model. The impacts of elevation angles on statistical properties are investigated. Standard deviation of Doppler frequencies on the large antenna array and condition numbers of the proposed 5G massive MIMO channel model are studied.

Chapter 5 presents a KBSM-BD-AA for massive MIMO channels. The proposed KBSM-BD-AA abstracts the cluster evolution on the array axis by a cluster survival probability matrix. Channel capacity analysis is performed in both the high and low SNR regimes.

Chapter 6 introduces a unified framework for 5G wireless channels. Typical scenarios such as massive MIMO communications, M2M communications, HST communications, and mmWave communications are included in the proposed unified framework. Correlation functions, stationary intervals, APS of the proposed unified framework, channel capacities of the proposed unified framework and the channel models in Chapter 3–Chapter 5 are studied in this chapter.

Chapter 7 concludes the thesis and points out future directions of modelling methods for 5G massive MIMO channels.

Chapter 2

MIMO Channel Modelling: Literature Review

2.1 Introduction

Two stochastic modelling approaches known as Geometry-Based Stochastic Models (GBSMs) and Correlation-Based Stochastic Models (CBSMs) have been widely used to simulate wireless channels. GBSMs are widely applied to Multiple-Input Multiple-Output (MIMO) channel modelling as they are mathematically tractable and relatively easy to fit measured data [34]. They are also independent to the layout of antenna arrays. Namely, GBSMs can be used to model various antenna settings. GBSMs model each cluster in the scattering environment based on its geometry relationships. Hence, GBSMs are able to model channel characteristics in a more accurate manner. However, GBSMs are usually of higher computational complexity. On the other hand, CBSMs are widely used to evaluate theoretical capacity and performance of massive MIMO systems because they are of lower implementation complexity and mathematically tractable. Distributions of eigenvalues of certain CBSMs were well-known in the literature [35]–[37]. Hence, signal processing algorithm design and channel capacity analysis with CBSMs are convenient. However, the accuracy of CBSMs is

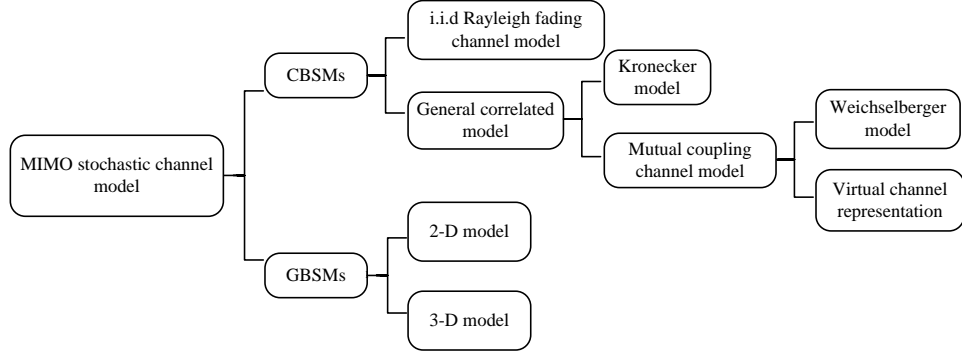


FIGURE 2.1: Classification of MIMO stochastic channel models.

usually compromised as these models are oversimplified. The classification of MIMO stochastic channel models is depicted in Fig. 2.1.

In this chapter, GBSMs and CBSMs for conventional MIMO channels will be introduced. In addition, recent advances on massive MIMO channel measurements will be reviewed, to show the research gap between massive MIMO channel characteristics and conventional MIMO GBSMs and CBSMs.

2.2 GBSMs

2.2.1 2-D GBSMs

Regular shape Two-Dimensional (2-D) GBSMs for MIMO channels assume that effective scatterers locate on regular shapes such as rings, ellipses, and rectangles. Based on the assumption that the Base Station (BS) is elevated and not surrounded by scatterers, the 2-D one-ring MIMO channel model was introduced in [34]. 2-D Two-ring MIMO GBSMs, which assumed that effective scatterers located on two circles [34], [38], [39], were particularly suitable for Machine-to-Machine (M2M) communications when both the transmitter and receiver were moving on the same horizontal level. Another key characteristic on the 2-D M2M two-ring MIMO channel is that Doppler frequencies need to be considered at both the transmitter and receiver sides. Having considered two scatter rings, a 2-D two-ring MIMO GBSM can conveniently be adapted to model dual Doppler frequencies and scattering environments. On the other

hand, when Angles of Arrival (AoAs) and Angles of Departure (AoDs) are correlated in the scattering environment, the ellipse model will be suitable to model this case. An ellipse GBSM, which was proposed to model micro-cells and pico-cells where the heights of antennas are relatively low, assumed that effective scatterers were placed on an ellipse surrounding the transmitter and receiver [34]. A 2-D ellipse GBSM was also used to develop High-Speed Train (HST) channel models [2], [40]. The geometry relationship between AoAs and AoDs was discussed in [41]. In addition, the 2-D ellipse model can easily be generalised for wideband models by adding confocal ellipses to represent other clusters [34], [40], [42].

Combinations of regular shape 2-D GBSMs appeared to be attractive to model complicated scattering environments. A 2-D two-ring GBSM and a 2-D ellipse GBSM were combined to model M2M channels in [43], [44]. In these models, the effective scatterers on the ellipse represented the scattering of buildings along a street while the effective scatterers on the two rings represented the scattering of vehicles around the transmitter and receiver. A 2-D multiple-ring model was proposed in [45] for the purpose of cooperative MIMO channel modelling, where effective scatterers located on circular rings.

Meanwhile, there are extensive standardised 2-D GBSMs for MIMO channels in the literature. The Third Generation Partnership Project (3GPP) Spatial Channel Model (SCM) [46] was proposed for System Level Simulation (SLS) and Link Level Simulation (LLS) of MIMO systems. The scattering environment between the BS and User Equipment (UE) was abstracted by a number of effective clusters. Each cluster consisted of 20 rays arriving at the same delay. The pathloss parameters of the UE, shadow fading, angular parameters, and delay of each cluster were determined stochastically based on distributions from measurements [46], [47] and assumed constant during one drop in SCM, where a drop is defined as one simulation run for a certain set of cells/sectors, BSs, and UEs, over a period of time [46]. Array responses of the BS and UE were computed based on angular parameters and geometry relationships. Therefore, spatial correlation characteristics between antenna elements were considered.

However, the maximum supported bandwidth of the SCM is 5 MHz [47]. It was not adequate to evaluate advanced wireless broadband systems. Hence, the standardised 2-D International Mobile Telecommunications Advanced (IMT-A) channel model was proposed. The IMT-A channel model followed similar modelling approaches as the SCM channel model but with higher time resolution and subpaths in certain clusters. Hence, the maximum supported bandwidth of the 2-D IMT-A channel model was enhanced to 100 MHz [48]. In addition, more scenarios were supported in the 2-D IMT-A channel model.

2.2.2 3-D GBSMs

In realistic scenarios, scatterers would disperse in the vertical plane [49]. As a result, the effect of elevation angles needs to be taken into account and only 2-D GBSMs may be insufficient to reflect full channel characteristics. Hence, Three-Dimensional (3-D) GBSMs should be developed for MIMO channels.

Extensive conventional 3-D MIMO models can be found in the literature. To begin with, 3-D twin-cluster MIMO channel models can be found in [50], [51]. In these models, each cluster consisted of two representations, one was placed at the transmitter side, the other was placed at the receiver side. The scattering environment between the two representations was abstracted by a virtual link delay. The shape of a cluster can be determined by angular spread in azimuth and elevation. It should be noticed that the COST 273 and the COST 2100 standardised models were developed based on the 3-D twin-cluster model [31], [33], [50], [52], [53]. A 3-D two-cylinder M2M narrowband GBSM was proposed in [54], where scatterers were placed on two cylinders. The impacts of elevation angles on space correlation functions were investigated. Later, this model was generalised to multiple concentric cylinders to support wideband channels [55]. In [56], [57], 3-D GBSMs combining a two-sphere model and an elliptic-cylinder model for both narrowband and wideband M2M channels were analysed. Also, a 3-D double-directional radio channel was proposed in [58]. A general description on 3-D GBSMs for 5G channel modelling was described in [59].

Regarding standardised 3-D GBSMs for MIMO channels, the 2-D SCM was extended to 3-D in [60] and [61] by computing the array responses with both azimuth and elevation angles. Although the WINNER II [30], the SCM-Extension (SCME) [61], and WINNER Phase + (WINNER+) [62] channel models followed the same modelling approach as the 2-D SCM and IMT-A models, the WINNER II channel model was improved by supporting 100 MHz bandwidth, eleven scenarios, and including 3-D modelling of clusters. Consequently, the WINNER II channel model was more extensively used for SLS of wireless systems such as Long-Term Evolution (LTE) [63], [64] and Worldwide Interoperability for the Microwave Access (WiMAX) [14].

For 60 GHz Institute of Electrical and Electronics Engineers (IEEE) 802.11ad Wireless Local Area Network (WLAN) systems, a standardised 3-D MIMO GBSM based on the SV model [65] was proposed in [66]. Because of the massive bandwidth in 60 GHz WLAN systems, the time resolution of IEEE 802.11ad systems is high, which results in resolvable rays within each cluster. The numbers of rays within cluster were modeled as Poisson-distributed random variables. Each ray had its own delay and complex gain. In addition, impacts of elevation angles were taken into account in the 802.11ad channel model.

Lately, the METIS GBSM was proposed [47] in order to model 5G wireless channels, such as channel features of M2M, millimetre wave (mmWave) communications. The METIS GBSM further improved the WINNER II channel model by supporting large antenna arrays, dual mobility, and new application scenarios such as indoor shopping mall and open air festival [47]. To better represent 3-D geometry, transformations of vectors between the Global Coordinate System (GCS) and the Local Coordinate System (LCS) were discussed. Also, the METIS GBSM pointed out potential methods for modelling time evolution of clusters and spherical wavefronts of massive antenna arrays.

2.3 CBSMs

2.3.1 Independent and Identically Distributed (i.i.d.) Rayleigh fading channel model

Classic i.i.d. Rayleigh fading channel processes were utilised as the channel model for conventional MIMO systems in [13], [17], [18], [21], [37]. Closed-form expressions for Bit Error Rate (BER) and channel capacity of conventional MIMO systems were derived. What is more, a fundamental tradeoff between diversity gain and multiplexing gain of MIMO systems in an i.i.d. Rayleigh fading channel was investigated in [67]. The analysis of MIMO performance under an i.i.d. Rayleigh fading channel is relatively simple because the eigenvalues of the product of the channel matrix and its Hermitian transpose followed the well-known Wishart distribution [35], [37]. In [68], [69], classic i.i.d. Rayleigh fading channel models were utilised to study the performance of massive MIMO systems. Since the channel coefficients are i.i.d., the central limit theorem as well as the random matrix theory can be easily applied to the analysis of massive MIMO channel matrices. When the size of the channel matrix of massive MIMO is large (the number of rows and the number of columns grow unboundedly with a constant ratio), the distribution of the eigenvalues of the product of the channel matrix and its Hermitian transpose converged to the Marčenow – Pastur density function [36], [70]. However, the i.i.d. Rayleigh fading channel model ignores correlations between antennas. Therefore, they are more suitable for widely separated antennas such as massive MIMO systems with distributed antennas than co-located antenna arrays.

2.3.2 Kronecker Based Stochastic Model (KBSM)

Compared with the i.i.d. Rayleigh channel model, KBSM utilised as the channel model for massive MIMO systems in [71] and [72] considered correlations between antennas. The total spatial correlation matrix can be obtained by the Kroncker product of spatial correlation matrices of both the transmitter and receiver sides [13]. KBSM is

popular in capacity and performance analysis of massive MIMO systems because of its simple implementation and consideration on antenna correlations. However, the underlying assumption of the KBSM is that the spatial correlation matrices of both link ends are separable. Moreover, line-of-sight (LOS) KBSMs can be found in [73] and [74].

2.3.3 Weichselberger channel model

Authors in [75] introduced the Weichselberger channel model which relaxed the separability restriction of the KBSM to analyse the performance of massive MIMO systems. This model has the ability to include antenna correlations at both the transmitter and receiver. Furthermore, it jointly considers the correlation between the transmit array and the receive array. The joint correlation is modeled by a coupling matrix, which can be acquired by measurement. Therefore, the Weichselberger channel model achieves a balance between accuracy and complexity for massive MIMO channel models. It can well model co-located antenna scenarios when the coupling effect between the transmit and receive array needs to be taken into account. Also, [75] added the LOS component to the Weichselberger model and henceforth entries of the channel matrix followed Rician fadings. Meanwhile, by eliminating the coupling effect between the transmit and receive antenna arrays, the Weichselberger channel model reduces to the KBSM in [75].

2.3.4 Virtual Channel Representation (VCR)

The VCR models the MIMO channel by predefined Discrete Fourier Transform (DFT) matrices instead of one-sided correlation matrices. As in [76], accuracy of VCR models increases with the number of antennas, as angular bins become smaller. That is to say, the VCR may play an important role in performance analysis of massive MIMO systems. Channel capacities of VCR were investigated in [77]. However, as pointed out in [78], VCR only supported single polarised Uniform Linear Arrays (ULAs).

Specifically, the Weichselberger model reduces to the VCR by forcing the eigenbases to be DFT matrices, and it reduces to the KBSM by forcing the coupling matrix to be of rank one [76].

2.4 Channel Measurements for Massive MIMO

For studying realistic characteristics of massive MIMO channels, measurements on benefits and effects caused by the increasing number of antennas are crucial. There are many papers on recent advances on massive MIMO channel measurements in the literature. For comparison convenience, measurement settings and investigated channel characteristics in these papers are listed in Table 2.1.

2.4.1 Capacity

It was demonstrated via measurements in [1], [79]–[89] that massive MIMO systems can significantly improve spectral efficiency. In [82], a scalable hardware architecture based on a Field-Programmable Gate Array (FPGA) platform was described and certain measurement results as well as implementation aspects were discussed. It was shown in [82] that the spectral capacity grew nearly linearly with massive MIMO, as suggested by theory.

In [80], [81], [84], [85], it was shown that low-complexity linear processing algorithms were able to provide sufficiently good performance in terms of capacity due to high interchannel orthogonality of massive MIMO. At the same time, high-complexity processing algorithms (e.g. dirty-paper coding) were capable of providing relatively small gains but with much higher computational complexity. Additionally, it was stated in [87] that capacity gains of massive MIMO in a realistic measured channel can be achieved with simple linear precoding and even a reasonable number of antennas.

Average mutual couplings were studied in the measurement campaign in [88] and [90] and comparisons between massive MIMO channels and i.i.d. channels were also discussed in [81], [86], [87].

TABLE 2.1: Recent advances in massive MIMO channel measurements

Ref.	Scenario	Carrier Frequency	Array Setting	Channel Characteristics
[1]	Outdoor	2.6 GHz	Virtual ULA 128×1	spatial correlation, K – factor, APS, eigenvalue distribution channel gain, etc.
[79]	Indoor	5.6 GHz	Virtual 2 – D antenna array $1 \times (12 \times 12)$	inverse condition number, RMS delay spread, etc.
[80]	Out – In In – Out – In	2.6 GHz	Planar + cylindrical 128×32	correlation function, capacity, sumrates, etc.
[81]	Outdoor	2.6 GHz	Virtual cylindrical 112×1	sum rates, correlation coefficient, capacity, condition number, etc.
[82]	Indoor	2.4 GHz	Planar 64×15	capacity, sum rates, etc.
[83]	Indoor	5.15 GHz	Patch+3–D positioner $1 \times (10 \times 10 \times 10)$	inner points, degrees of freedom, etc.
[84]	Indoor	5.3 GHz	Two moving TX+ LU Rx/TKK Rx	capacity, sum rates, etc.
[85]	Outdoor	2.6 GHz	Virtual ULA 128×1	capacity, sum rates, RMS delay spread, etc.
[86] [87]	Outdoor	2.6 GHz	Virtual ULA+ cylindrical array 128×128	achieved sum rates, capacity, singular value spreads, etc.
[88]	Indoor	2.70 GHz 2.82 GHz	24/36-port cube	mutual couplings, capacity, etc.
[89]	Outdoor	2.6 GHz	Virtual ULA/ cylindrical array $128 \times 1/128 \times 1$	capacity
[90] [91]	Outdoor	3.7 GHz	Planar 4×100	Mutual coupling, signal constellation points
[92]	Indoor	2-8 GHz	ULA 1×20	channel response, cluster number, angle spread, delay spread, angle PDF, PDP, etc.
[93]	Out – In In – Out – In	2.6 GHz	Planar + cylindrical 128×32	RMS delay spread, channel separation, interference power level, etc.
[94]	Reverberation chamber	1 GHz	Virtual ULA+ log periodic array(LPA)	average power, K – factor, coherence bandwidth, RMS delay spread, mean delay, spatial correlation, beamforming APS, etc.
[95]	Indoor	5.3 GHz	Cylindrical+ semi – spherical 64×21	path loss, PDP, capacity, etc.
[53]	Outdoor	2.6 GHz	Virtual ULA 128×1	AoA, delay, complex amplitude, etc.
[96]	Outdoor	28/38/60 GHz	ULA 12×4	throughput, reflectivities, etc.

2.4.2 Spherical wavefront and non-stationarities

Measurements on massive MIMO channels in [1] and [93] demonstrated that the channel cannot be regarded as Wide Sense Stationary (WSS) over the large antenna array. First, the farfield assumption, which is equivalent to plane wavefront approximation, is violated because the distances between the transmitter and receiver (scatterer) may not be beyond the Rayleigh distance. Second, certain clusters are not observable over the whole array. That is to say, each antenna element on the large array may have its own set of clusters. Spherical wavefronts and non-stationarities on the array axis can

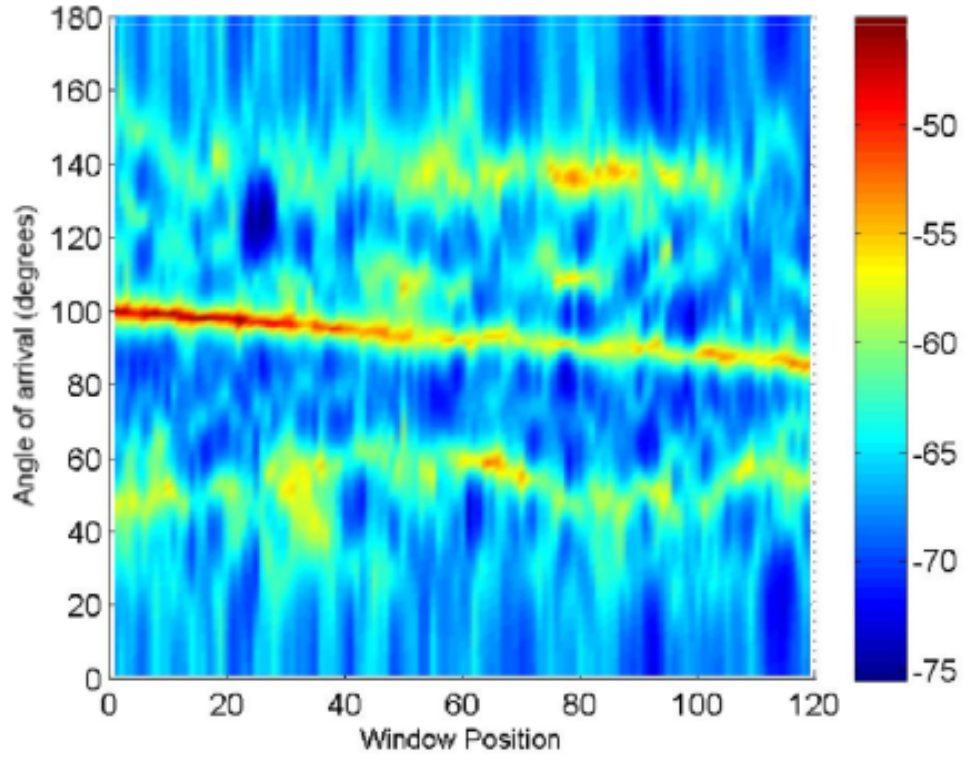


FIGURE 2.2: APS of massive MIMO [1, Fig. 6].

be seen in Fig. 2.2 [1, Fig. 6]. Also, power imbalance and Rician K-factor variation over the antenna array are seen as well. These three factors of massive MIMO channels indicate that the conventional modelling method of MIMO channels need to be extended.

2.4.3 Eigenvalue properties

Eigenvalue distribution of massive MIMO channels was measured in [1], showing that massive MIMO increased channel orthogonality between terminals by increasing the number of transmit antennas. Similar conclusions were drawn in [79] and [81] via (inverse) condition numbers, in [83] via degrees of freedom, and in [86] via singular value spreads.

2.4.4 Other channel characteristics

Other channel characteristics such as angle Probability Density Function (PDF), Root Mean Square (RMS) delay spread, Power Delay Profile (PDP), Angular Power Spectrum (APS) and correlation between subchannels were also studied in [79]–[94]. Author in [80] considered practical outdoor-to-indoor transmissions and observed that there was hardly any extra capacity gain for more than 20 antennas when linear precoding was applied. Furthermore, cell throughput and reflectivities of massive MIMO with mmWave were measured in [96].

2.4.5 Challenges on massive MIMO channel measurements

For massive MIMO channels, it is important to measure parameters related to non-stationary properties such as non-stationarities on the array axis as well as on the time axis. However, these parameters are difficult to estimate since they fluctuate from scenarios to scenarios. Hence, a large number of measurement campaigns are required to capture those parameters.

Currently, many published measurement results were obtained via virtual antenna arrays. To acquire more realistic channel characteristics, a large physical antenna array is required. In this case, the mutual coupling effect between antenna elements will be considered. However, from a realisation point of view, the increase of the number of antennas will require many Radio Frequency (RF) chains and then raise higher requirements for antenna calibrations.

Most of current measurements on massive MIMO channels focus on using ULAs. However, to utilise space compactly, other types of arrays such as planar arrays and cube arrays need to be considered.

2.5 Research Gap

Channel measurements in Section 2.4 have shown that the above mentioned conventional MIMO GBSMs in Section 2.2 are not suitable to be directly applied to modelling massive MIMO channels. Measurements on massive MIMO channels in [1] and [87] indicated that there are two characteristics making massive MIMO channels different from conventional MIMO channels. First, since the number of antennas is huge in massive MIMO systems, the farfield assumption in conventional MIMO channels may no longer be appropriate. The distance between the receiver and transmitter (or a cluster) may not be beyond the Rayleigh distance defined by $\frac{2\mathcal{L}^2}{\lambda}$ [97], where \mathcal{L} and λ are the dimension of the antenna array and carrier wavelength, respectively. For ULAs with a fixed antenna separation Δ (e.g., $\Delta = \lambda/2$), the dimension $\mathcal{L} = (\mathcal{M} - 1)\Delta$ is linearly increasing with the number of antenna elements \mathcal{M} . Therefore, the wavefront should be assumed as spherical instead of plane when the number of antennas is large. Although the impact of spherical wavefront on short-range or constant distance communications was studied in [98] and [99], its impact on massive MIMO channels has not yet been reported in the literature. Second, non-stationary properties can be observed on large antenna arrays [1], i.e., appearance and disappearance of clusters can occur on the array axis. This leads to the fact that each antenna element on the array may observe different sets of clusters, which is not characterised in conventional MIMO channels. As a result, the WSS assumption on antenna arrays does not necessarily hold for massive MIMO channels. The authors in [100], [100]–[102] modeled cluster evolution on the time axis with birth-death processes or Markov processes. However, non-stationary properties of clusters on the array axis have not been studied for massive MIMO channels in the literature.

Although GBSMs are able to capture the massive MIMO characteristic of cluster evolution on the array axis mentioned in [1] and [87], they may not be feasible for capacity analysis because of their complexity. CBSMs described in Section 2.3 cannot fully characterise massive MIMO channel characteristics. Therefore, a novel simple CBSM that considers different sets of scatterers for different antennas is necessary for capacity analysis of massive MIMO channels.

2.6 Summary

This chapter has reviewed and classified typical stochastic channel models for MIMO channels, i.e., GBSMs, CBSMs. Features of each channel model have been introduced. GBSMs are able to provide more accurate interpretations of realistic MIMO channels at the cost of higher computational complexity. CBSMs are suitable for performance analysis of MIMO systems for their simplicity. However, recent measurements of massive MIMO channel characteristics have demonstrated that channel models for conventional MIMO are insufficient for massive MIMO channels. Massive MIMO channel models should take into account specific characteristics which differ them from those in conventional MIMO channels, such as the spherical wavefront assumption and non-stationary properties. This will normally increase the complexity of massive MIMO channel models. First-order simplifications of the channel model will not be appropriate with the spherical wavefront instead of plane wavefront assumption. Also, conventional MIMO channel models cannot be directly applied to massive MIMO channels in which different antennas may observe different sets of clusters. These two important features are hardly to be embedded in CBSMs although they are simple. On the other hand, complex GBSMs can reflect massive MIMO channel characteristics but many more models for different practical scenarios are yet to be developed. 3-D massive MIMO models, which jointly consider azimuth and elevation angles, are more practical as well as complicated. In summary, new massive MIMO channel models should be developed having a good tradeoff between model accuracy and complexity and considering different practical scenarios with specific channel characteristics.

Chapter 3

A Non-Stationary 2-D Ellipse Model for Massive MIMO Channels

3.1 Introduction

A massive Multiple-Input Multiple-Output (MIMO) system is equipped with much more antennas, typically tens or hundreds, than conventional MIMO systems [22], [103]. With such a massive number of antennas, it has been demonstrated that a massive MIMO system is able to provide many benefits, such as greatly increasing the capacity, simplifying scheduling design in the frequency domain [22], and averaging interference according to the large number theorem [23]. Generally speaking, a massive MIMO system can be considered as an enhanced version of conventional MIMO by utilizing an enormous number of antennas. As a result, its system performance, in terms of capacity, efficiency, and reliability, is significantly better than conventional MIMO systems [22], [103].

To design and evaluate MIMO systems, an accurate small-scale fading MIMO channel model is necessary. Conventional small-scale fading MIMO channel models have been widely studied in the literature. Extensive Geometry-Based Stochastic Models (GB-SMs) for conventional MIMO channels known as one-ring model, two-ring model, and ellipse model can be found in [34], [104]. Also, a combined ellipse and two-ring model

was proposed in [43] and [44], a multiple circular-ring model was proposed in [45], and three-dimensional (3-D) concentric-cylinder models can be found in [56] and [105]. The authors in [50] proposed a twin cluster model which concerned only the first and the last bounces. The SCM [106], WINNER II model [30], IMT-A model [48], COST 273 model [52], and COST 2100 model [31], [33] have also been widely utilised. Besides, correlation-based conventional MIMO channel models such as the Kronecker-Based Stochastic Model (KBSM) and the Weichselberger model were used to investigate the performance of massive MIMO systems in [107] and [70].

However, according to the measurement observations in [1] and [87], the above mentioned MIMO channel models [30], [31], [33], [34], [43]–[45], [48], [50], [52], [56], [70], [104]–[107] are not sufficient to accurately capture certain characteristics of massive MIMO channels. First, conventional MIMO channel models solely assume that the distance between a scatterer and an antenna array is far beyond the Rayleigh distance [108], [109], i.e., $2\mathcal{L}^2/\lambda$, where \mathcal{L} is the dimension of the antenna array and λ is the carrier wavelength. Namely, the farfield and plane wavefront assumptions were usually applied to simplifying the channel models. However, the authors in [1] and [87] stated that as the number of antennas is massive, the plane wavefront assumption is not fulfilled for massive MIMO channels. Instead, a spherical wavefront channel model should be considered. Spherical wavefront models and plane wavefront models were compared in [110] and [99]. The authors in [110] pointed out that the plane wavefront assumption underestimates the rank of the channel matrix. However, [110] and [99] only focused on short range or constant distance communications which were not applicable for general massive MIMO systems. Second, dynamic properties of clusters such as cluster appearance and disappearance, Angle of Arrival (AoA) shifts, as well as non-stationarities were observed on the antenna array axis [1], [87]. The characterisation of non-stationarities was investigated in [100]–[102], [111], where the appearance and disappearance of clusters on the time axis were modeled using the birth-death (BD) or Markov processes. The authors in [61] and [112] analysed time-variant geometrical properties such as AoA and Angle of Departure (AoD), but they ignored the evolution of clusters. However, [61], [100]–[102], [111], [112] only took non-stationarities on the time axis into account and ignored non-stationarities on the array axis. The

authors in [113] considered nearfield effects and non-stationarities on the array axis. However, in [113], the impact of spherical wavefront on Non-Line-of-Sight NLOS components was missing, characteristics of cluster appearance and disappearance were not studied in detail, and non-stationarities on the time axis were not included. A 3-D non-stationary twin-cluster channel model was proposed in [51] for massive MIMO systems considering spherical wavefront and non-stationarities on both time and array axes. However, AoAs and AoDs were assumed independent, channel characteristics such as power imbalance on the antenna array and Space-Time-Frequency Correlation Function (STFCF) were not investigated in [51].

In this chapter, a novel 2-D non-stationary wideband multi-confocal ellipse model for massive MIMO systems is proposed. This channel model is developed aiming to capture the spherical wavefront effect and non-stationary properties on both the array and time axes. Also, AoAs and AoDs are assumed dependent in the ellipse model. The major **contributions** of this chapter are summarised as follows:

1. The plane wavefront assumption for conventional MIMO channel models is relaxed, i.e., the nearfield effect of spherical wavefront is considered in the proposed wideband ellipse model. The impacts of spherical wavefront assumption on both the LOS component and NLOS components are studied.
2. Birth-Death (BD) process is applied to the array axis in order to capture the cluster appearance and disappearance on the antenna array axis as reported in [1]. Combining the BD process modelling cluster time evolution in [100], array-time evolution of clusters of the proposed wideband massive MIMO channel model is proposed. A novel cluster evolution algorithm is developed based on the BD process on both the array and time axes.
3. Statistical properties of the proposed massive MIMO channel model such as STFCF and Cumulative Distribution Functions (CDFs) of survival probabilities of clusters and received power imbalance on the antenna array are investigated.

This chapter is organised as follows. In Section 3.2, the proposed wideband ellipse MIMO channel model is discussed in detail. This includes geometrical properties

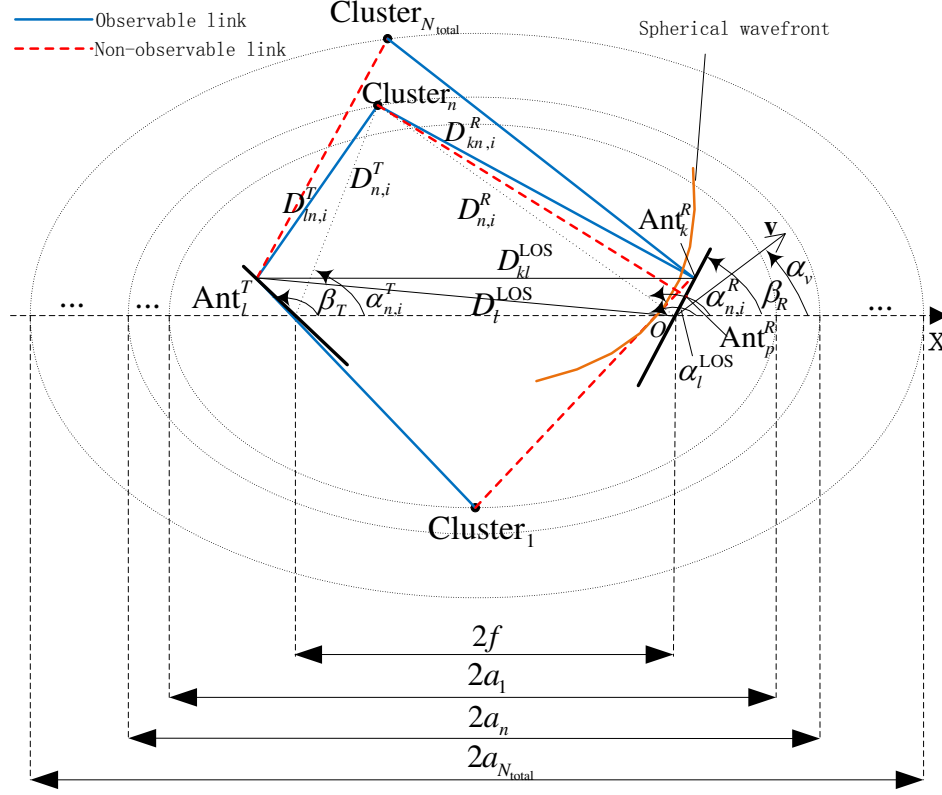


FIGURE 3.1: A wideband multi-confocal ellipse model for massive MIMO systems.

derived under the spherical wavefront assumption as well as the novel algorithm which describes the cluster evolution on the array axis. Section 3.3 presents the array-time evolution model, which describes dynamic properties of clusters on both the array and time axes. Statistical properties are investigated as well. A corresponding wideband ellipse simulation model is discussed in Section 3.4. In Section 3.5, numerical analysis is given. Conclusions are finally drawn in Section 3.6.

3.2 A Wideband Ellipse Model for Massive MIMO Systems

In this section, a novel wideband ellipse 2-D channel model for massive MIMO is proposed, including spherical wavefront and cluster evolution on the array axis as shown in Fig. 3.1. (The combination of cluster evolutions on both the time and array

axes will be presented in Section 3.3). Let us assume that the transmitter and receiver are equipped with Uniform Linear Arrays (ULAs) with M_T and M_R omnidirectional antennas, respectively. The antenna elements are spaced with separation δ_T and δ_R , and they are located at the focal points of the confocal ellipses with a distance of $2f$. One advantage of GBSMs is that the calculations of channel coefficients depend only on geometry relationships between objects in the model. As a result, although co-located antennas are used in this chapter for presentation convenience, the same modeling approach can be generalised to distributed antenna arrays.

Let Ant_l^T represent the l -th antenna of the transmit array and Ant_k^R represent the k -th antenna of the receive array. The n -th cluster is on the n -th ellipse with major axis $2a_n$. The angle β_T (β_R) denotes the tilt angle of the transmit (receive) antenna array. The angle α_v denotes the angle between the x-axis and the direction of movement of the receiver. The maximum Doppler frequency and carrier wavelength are denoted as f_{\max} and λ , respectively.

For massive MIMO channel models, there are two important properties should be noticed. First, the farfield assumption for conventional MIMO channel models [34], [43], which is equivalent to the plane wavefront assumption, is not fulfilled as the dimension of the antenna array can not be ignored when the number of antennas is massive. As a result, the wavefront emitted from the n -th cluster to the receive array is assumed to be spherical as shown in Fig. 3.1. Then, the AoA is no longer linear along the array, and it needs to be computed based on geometrical relationships. The impact of spherical wavefront will be analysed in detail in following paragraphs.

Second, as reported in [1] and [87], the behavior of clusters is not stationary on the array axis, which means that a cluster may not always be observable to all the antenna elements of an array in conventional MIMO channel models. An example is given in Fig. 3.1 that Cluster_1 is observable to Ant_l^T but it is not observable to Ant_k^R . $\text{Cluster}_{N_{\text{total}}}$ is observable to Ant_k^R but it is non-observable to Ant_l^T . Conversely, Cluster_n is observable to both Ant_k^R and Ant_l^T but not to Ant_p^R . These situations imply that *different antenna elements may observe different sets of clusters*, which is not assumed in conventional MIMO channel models. Let C_l^T (C_k^R) denote the cluster set

in which clusters are observable to Ant_l^T (Ant_k^R), the generation of C_l^T and C_k^R will be modeled as BD processes as described in Section 3.2.1. Also, let N_{total} denote the total number of clusters which are observable to at least one transmit antenna and one receive antenna, N_{total} can be expressed as [51]

$$N_{\text{total}} = \text{card} \left(\bigcup_{l=1}^{M_T} \bigcup_{k=1}^{M_R} (C_l^T(t) \cap C_k^R(t)) \right) \quad (3.1)$$

where the operator $\text{card}(\cdot)$ denotes the cardinality of a set. Then, a cluster, say Cluster_n ($n \leq N_{\text{total}}$), is observable to both Ant_l^T and Ant_k^R if and only if $\text{Cluster}_n \in \{C_l^T \cap C_k^R\}$.

TABLE 3.1: Summary of key parameter definitions for the 2-D ellipse model.

$\delta_T(\delta_R)$	antenna spacing of the transmit (receive) antenna array
$M_T(M_R)$	number of transmit (receive) antennas
$2f$	distance between the transmitter and receiver (focal length)
a_n	semi-major axis of the n -th ellipse
$\beta_T(\beta_R)$	tilt angles of the transmit (receive) antenna array
f_{\max}, λ	maximum Doppler frequency and carrier wavelength
$\text{Ant}_l^T, \text{Ant}_k^R$	the l -th transmit antenna and the k -th receive antenna
D_{kl}^{LOS}	LOS distance between Ant_k^R and Ant_l^T
$D_{ln,i}^T$	distance between the n -th cluster and Ant_l^T via the i -th ray within the cluster
$D_{kn,i}^R$	distance between the n -th cluster and Ant_k^R via the i -th ray within the cluster
f_{kl}^{LOS}	Doppler frequency of the LOS component between Ant_k^R and Ant_l^T
$f_{n,i}$	Doppler frequency of the n -cluster via the i -th ray
$\varphi_{kl}^{\text{LOS}}$	phase of the LOS component between Ant_k^R and Ant_l^T
$\varphi_{kl,n,i}$	phase of the n -th cluster between Ant_k^R and Ant_l^T via the i -th ray
$\alpha_{n,i}^T$	AoD of the i -th ray of the n -th cluster to the transmit array center
$\alpha_{n,i}^R$	AoA of the i -th ray of the n -th cluster to the receive array center

Based on the above mentioned analysis and the summary of key parameter definitions in Table 3.1, the wideband massive MIMO channel can be presented as an $M_R \times M_T$ complex matrix $\mathbf{H}(t, \tau) = [h_{kl}(t, \tau)]_{M_R \times M_T}$, where $k = 1, 2, \dots, M_R$ and $l = 1, 2, \dots, M_T$. Next, assume the initial phase of the signal at the transmitter is φ_0 , LOS Rician factor is K and the LOS component is always connected to all antennas and the first cluster to arrive at the receiver if the LOS component exists. Additionally, assume that the mean power of the n -th cluster is P_n and there are S rays within one cluster and $\alpha_{n,i}^R$ is the AoA of the i -th ray of the n -th cluster to the receive array center, $\alpha_{n,i}^T$ is the AoD of the i -th ray of the n -th cluster ($i = 1, 2, \dots, S$) to the

transmit array center, the multipath complex gains $h_{kl}(t, \tau)$ of the theoretical model ($S \rightarrow \infty$) between Ant_l^T and Ant_k^R at delay τ can be presented as

$$h_{kl}(t, \tau) = \sum_{n=1}^{N_{\text{total}}} h_{kl,n}(t) \delta(\tau - \tau_n) \quad (3.2)$$

where the complex gain $h_{kl,n}(t)$ of Cluster_n can be computed as

-if $\text{Cluster}_n \in \{C_l^T \cap C_k^R\}$,

$$h_{kl,n}(t) = \underbrace{\delta(n-1) \sqrt{\frac{K}{K+1}} e^{j(2\pi f_{kl}^{\text{LOS}} t + \varphi_{kl}^{\text{LOS}})}}_{\text{LOS}} + \underbrace{\sqrt{\frac{P_n}{K+1}} \lim_{S \rightarrow \infty} \frac{1}{\sqrt{S}} \sum_{i=1}^S e^{j(2\pi f_{n,i} t + \varphi_{kl,n,i})}}_{\text{NLOS}} \quad (3.3)$$

-if $\text{Cluster}_n \notin \{C_l^T \cap C_k^R\}$,

$$h_{kl,n}(t) = 0. \quad (3.4)$$

For the LOS component, under the spherical wavefront assumption,

$$\begin{aligned} \varphi_{kl}^{\text{LOS}} = \varphi_0 + \frac{2\pi}{\lambda} [(D_l^{\text{LOS}})^2 + \left(\frac{M_R - 2k + 1}{2} \delta_R \right)^2 \\ - (M_R - 2k + 1) \delta_R D_l^{\text{LOS}} \cos(\alpha_l^{\text{LOS}} - \beta_R)]^{1/2} \end{aligned} \quad (3.5)$$

where

$$D_l^{\text{LOS}} = [(2f)^2 + \left(\frac{M_T - 2l + 1}{2} \delta_T \right)^2 - 2f(M_T - 2l + 1) \delta_T \cos(\beta_T)]^{1/2} \quad (3.6)$$

and the AoA α_l^{LOS} of the LOS component from Ant_l^T to the receive array center can be computed as

$$\alpha_l^{\text{LOS}} = \pi - \arcsin \left[\frac{\sin \beta_T}{D_l^{\text{LOS}}} \left(\frac{M_T - 2l + 1}{2} \delta_T \right) \right]. \quad (3.7)$$

The Doppler frequency f_{kl}^{LOS} of the LOS component between Ant_k^R and Ant_l^T can be calculated as

$$f_{kl}^{\text{LOS}} = f_{\max} \cos(\pi - \arcsin \left[\frac{D_l^{\text{LOS}}}{D_{kl}^{\text{LOS}}} \sin(\alpha_l^{\text{LOS}} - \beta_R) \right]) \quad (3.8)$$

where

$$D_{kl}^{\text{LOS}} = [(D_l^{\text{LOS}})^2 + \left(\frac{M_R - 2k + 1}{2} \delta_R \right)^2 - (M_R - 2k + 1) \delta_R D_l^{\text{LOS}} \cos(\alpha_l^{\text{LOS}} - \beta_R)]^{1/2}. \quad (3.9)$$

For the NLOS components, AoAs $\alpha_{n,i}^R$ and AoDs $\alpha_{n,i}^T$ are dependent in an ellipse model, their relationship can be presented as [34]

$$\alpha_{n,i}^T = \begin{cases} g(\alpha_{n,i}^R) & \text{if } 0 < \alpha_{n,i}^R \leq \alpha_0 \\ g(\alpha_{n,i}^R) + \pi & \text{if } \alpha_0 < \alpha_{n,i}^R \leq 2\pi - \alpha_0 \\ g(\alpha_{n,i}^R) + 2\pi & \text{if } 2\pi - \alpha_0 < \alpha_{n,i}^R \leq 2\pi \end{cases} \quad (3.10)$$

where

$$g(\alpha_{n,i}^R) = \arctan \left[\frac{(k_0^2 - 1) \sin(\alpha_{n,i}^R)}{2k_0 + (k_0^2 + 1) \cos(\alpha_{n,i}^R)} \right] \quad (3.11)$$

$$\alpha_0 = \pi - \arctan \left(\frac{k_0^2 - 1}{2k_0} \right) \quad (3.12)$$

$$k_0 = a_n / f. \quad (3.13)$$

Given the semi-major axis a_1 of the first ellipse, the semi-major axis (size) of the n -th ellipse, i.e., a_n , can be determined by τ_n relative to the first ellipse as

$$a_n = c\tau_n + a_1 \quad (3.14)$$

where c is the speed of light. Accordingly, the distance between the n -th cluster and the transmitter via the i -th ray, $D_{n,i}^T$, as well as the distance between the n -th cluster and the receiver via the i -th ray, $D_{n,i}^R$, can be derived according to their geometrical

relationships:

$$D_{n,i}^R = \frac{2a_n \sin \alpha_{n,i}^T}{\sin \alpha_{n,i}^T + \sin(\pi - \alpha_{n,i}^R)} \quad (3.15)$$

$$D_{n,i}^T = \frac{2a_n \sin(\pi - \alpha_{n,i}^R)}{\sin \alpha_{n,i}^T + \sin(\pi - \alpha_{n,i}^R)}. \quad (3.16)$$

Then, the distance between the n -th cluster and Ant_l^T via the i -th ray within the cluster, $D_{ln,i}^T$, can be computed as

$$D_{ln,i}^T = [(D_{n,i}^T)^2 + \left(\frac{M_T - 2l + 1}{2} \delta_T\right)^2 - (M_T - 2l + 1) \delta_T D_{n,i}^T \cos(\beta_T - \alpha_{n,i}^T)]^{1/2}. \quad (3.17)$$

The distance between the n -th cluster and Ant_k^R via the i -th ray within the cluster, $D_{kn,i}^R$, can be computed as

$$D_{kn,i}^R = [(D_{n,i}^R)^2 + \left(\frac{M_R - 2k + 1}{2} \delta_R\right)^2 - (M_R - 2k + 1) \delta_R D_{n,i}^R \cos(\alpha_{n,i}^R - \beta_R)]^{1/2}. \quad (3.18)$$

Based on the above equations, the received phase of Ant_k^R via the i -th ray within the n -th cluster from Ant_l^T , $\varphi_{kl,n,i}$, can be expressed as

$$\varphi_{kl,n,i} = \varphi_0 + \frac{2\pi}{\lambda} (D_{ln,i}^T + D_{kn,i}^R). \quad (3.19)$$

The Doppler frequency of the i -th ray within the n -th cluster, $f_{n,i}$, is

$$f_{n,i} = f_{\max} \cos(\alpha_{n,i}^R - \alpha_v). \quad (3.20)$$

3.2.1 Array axis evolution—generation of cluster sets C_l^T and C_k^R

Thus far, all the geometrical relationships have been derived from (3.5) to (3.20). In this section, we will model the dynamic properties of clusters, i.e., the appearance and disappearance of clusters on the array axis, using a BD process. In previous

literature [100] and [114], the BD process was deployed to model the channel non-stationarity along the time axis, describing the cluster variations in terms of the change of time. For massive MIMO systems, the time axis BD process [100] will be adapted to the array axis [51]. Let λ_G (per meter) and λ_R (per meter) denote the cluster generation rate and the recombination rate. Next, by defining the scenario-dependent correlation factor D_c^a on the array axis, let the operator \xrightarrow{E} represent evolution on either array or time axis, when a cluster set evolves from Ant_{l-1}^T to Ant_l^T or from Ant_{k-1}^R to Ant_k^R , denoted as $C_{l-1}^T \xrightarrow{E} C_l^T$ or $C_{k-1}^R \xrightarrow{E} C_k^R$, the survival probabilities of the clusters inside the cluster set at the transmitter P_{survival}^T and at the receiver P_{survival}^R can be modeled as [115]

$$P_{\text{survival}}^T = e^{-\lambda_R \frac{\delta_T}{D_c^a}} \quad (3.21)$$

$$P_{\text{survival}}^R = e^{-\lambda_R \frac{\delta_R}{D_c^a}}. \quad (3.22)$$

According to the BD process, the duration between two cluster appearances and the duration between two cluster disappearances are exponentially distributed [111] [115], the average number of newly generated clusters N_{new}^T and N_{new}^R based on the Poisson process can be computed as [115]

$$E[N_{\text{new}}^T] = \frac{\lambda_G}{\lambda_R} \left(1 - e^{-\lambda_R \frac{\delta_T}{D_c^a}}\right) \quad (3.23)$$

$$E[N_{\text{new}}^R] = \frac{\lambda_G}{\lambda_R} \left(1 - e^{-\lambda_R \frac{\delta_R}{D_c^a}}\right) \quad (3.24)$$

where $E[\cdot]$ designates the expectation. Cluster sets of each antenna are generated based on BD process on the array axis. The flowchart of the cluster generation algorithm is shown in Fig. 3.2.

First, let the initial number of clusters be N , the initial cluster set of Ant_1^T be $C_1^T = \{c_1^T, c_2^T, c_x^T, \dots, c_N^T\}$, and the initial cluster set of Ant_1^R be $C_1^R = \{c_1^R, c_2^R, c_x^R, \dots, c_N^R\}$, where c_x^T and c_x^R denote cluster members of cluster sets of the transmitter and the receiver, and the subscript x ($x = 1, 2, \dots, N$) of c_x^T and c_x^R denotes the cluster indices. The cluster sets of the rest of antennas at the transmitter side C_l^T ($l = 2, 3, \dots, M_T$)

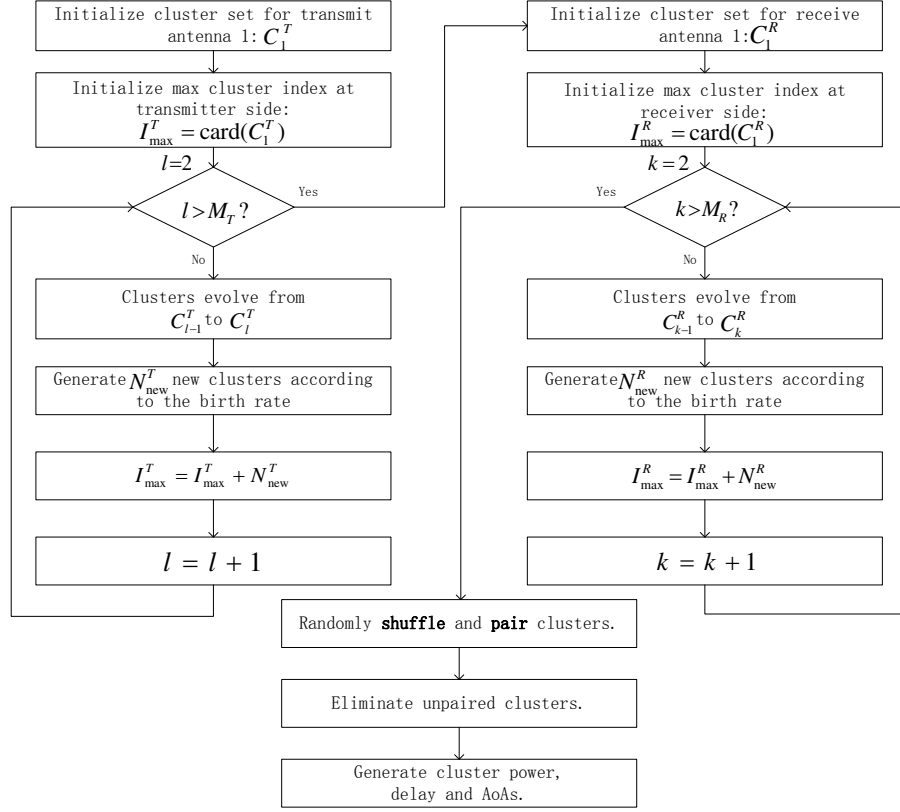


FIGURE 3.2: Cluster generation algorithm flowchart.

and the receiver side C_k^R ($k = 2, 3, \dots, M_R$) can be generated from the evolution of C_1^T and C_1^R , respectively. The survival probability of clusters to the next antenna is calculated according to (3.21) and (3.22). At the same time, new clusters are generated based on Poisson process with mean numbers as (3.23) and (3.24). These newly generated clusters are added to the cluster sets of corresponding antennas. Since each cluster evolves gradually on the antenna array, i.e., it will not appear again after its disappearance, antenna correlations have been naturally embedded in the generation process.

Second, after obtaining cluster sets of each antenna, $\bigcup_{l=1}^{M_T} C_l^T$ and $\bigcup_{k=1}^{M_R} C_k^R$ are the full collections of clusters observable to the transmitter and receiver, respectively. To mimic the arbitrariness of the propagation environment, the cluster indices in $\bigcup_{l=1}^{M_T} C_l^T$ and $\bigcup_{k=1}^{M_R} C_k^R$ are shuffled and arranged in a random order. Then, cluster indices of the transmitter and receiver are paired. This process determines to which transmit and receive antennas each cluster is observable. An example of the random shuffling and

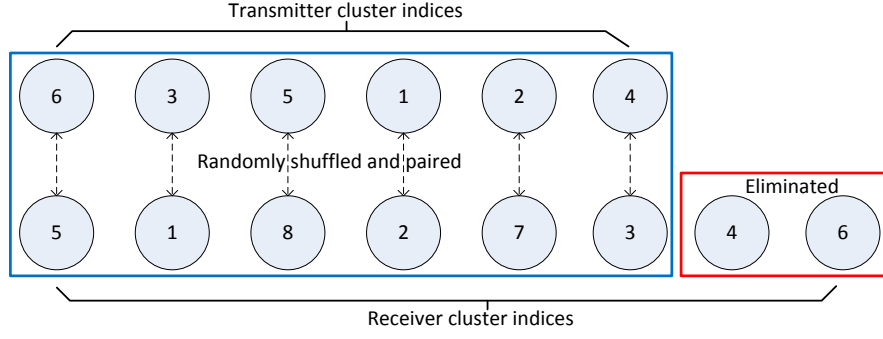


FIGURE 3.3: An example of random shuffling and pairing between the transmitter and receiver cluster indices.

pairing process has been illustrated in Fig. 3.3. In this example, transmit antennas who can observe c_6^T share a common cluster with receiver antennas who can observe c_5^R . Other clusters can be determined in the same way. Meanwhile, it is possible that the cardinalities of $\bigcup_{l=1}^{M_T} C_l^T$ and $\bigcup_{k=1}^{M_R} C_k^R$ are not equal, i.e., there are clusters that are not observable to either the transmit array or the receive array. It can be seen in Fig. 3.3 that two more clusters are observable to the receiver than the transmitter. In this case, after random shuffling and pairing, two clusters are eliminated from the full receiver cluster set. Then, the cluster indices of these remained clusters are reassigned from 1 to N_{total} .

Last, the delays and mean power of clusters are generated according to the urban macro-cell scenario in [30] where delays and mean power are drawn randomly obeying the exponential distributions. After delays are obtained, the semi-major axes can be determined via (3.14). Since mean power is related to delay in [30], the mean power of a cluster is then related to the size of its corresponding ellipse. In addition, AoAs are modeled as the von Mises distribution [116]. As von Mises distribution can be easily adapted to other distributions such as uniform distribution and wrapped Gaussian distribution, it is widely utilised in the literature [34], [43], [44] to model angular dispersions.

3.2.2 Space Cross-Correlation Function (CCF) analysis

Regarding the analysis of the spatial properties of the wideband model for massive MIMO with cluster evolution on the antenna arrays, the space CCF is introduced in this section. The normalised space CCF $\rho_{kl,k'l',n}(\delta_T, \delta_R; t)$ between the link connecting Ant_k^R and Ant_l^T and the link connecting $\text{Ant}_{k'}^R$ and $\text{Ant}_{l'}^T$ of the n -th cluster at time t is defined as [34] [117]

$$\rho_{kl,k'l',n}(\delta_T, \delta_R; t) = \text{E} \left[\frac{h_{kl,n}(t)h_{k'l',n}^*(t)}{|h_{kl,n}(t)||h_{k'l',n}^*(t)|} \right] \quad (3.25)$$

where $h_{k'l',n}^*(t)$ denotes the conjugate of $h_{k'l',n}(t)$. The LOS component and the NLOS components are independent to each other. As a result, the space CCF can be rewritten as the sum of the spatial correlation of the LOS component $\rho_{kl,k'l',n}^{\text{LOS}}(\delta_T, \delta_R; t)$ and the spatial correlation of the NLOS components $\rho_{kl,k'l',n}^{\text{NLOS}}(\delta_T, \delta_R; t)$.

$$\rho_{kl,k'l',n}(\delta_T, \delta_R; t) = \rho_{kl,k'l',n}^{\text{LOS}}(\delta_T, \delta_R; t) + \rho_{kl,k'l',n}^{\text{NLOS}}(\delta_T, \delta_R; t). \quad (3.26)$$

For the spatial correlation of the LOS component,

$$\rho_{kl,k'l',n}^{\text{LOS}}(\delta_T, \delta_R; t) = \frac{K\delta(n-1)}{K+1} e^{j(2\pi f_{kl}^{\text{LOS}}t + \varphi_{kl}^{\text{LOS}} - 2\pi f_{k'l'}^{\text{LOS}}t - \varphi_{k'l'}^{\text{LOS}})}. \quad (3.27)$$

For the spatial correlation of the NLOS components, a cluster observable to Ant_l^T and Ant_k^R has a probability of $e^{-\lambda_R|l-l'|\delta_T/D_c^a} e^{-\lambda_R|k-k'|\delta_R/D_c^a}$ to survive to connect $\text{Ant}_{l'}^T$ and $\text{Ant}_{k'}^R$. Since the number of rays is infinite in the theoretical model, the discrete AoAs $\alpha_{n,i}^R$ can be represented by a continuous random variable α_n^R . Therefore, given the Probability Density Function (PDF) of the AoA $p_{\alpha_n^R}(\alpha_n^R)$, $\rho_{kl,k'l',n}^{\text{NLOS}}(\delta_T, \delta_R; t)$ can be computed as

$$\rho_{kl,k'l',n}^{\text{NLOS}}(\delta_T, \delta_R; t) = \frac{e^{\lambda_R \frac{-|l-l'|\delta_T - |k-k'|\delta_R}{D_c^a}}}{K\delta(n-1) + 1} \times \int_{-\pi}^{\pi} e^{j[\varphi_{kl,n}(\alpha_n^R) - \varphi_{k'l',n}(\alpha_n^R)]} p_{\alpha_n^R}(\alpha_n^R) d\alpha_n^R. \quad (3.28)$$

Equations (3.27) and (3.28) indicate that the difference between $\varphi_{kl,n}$ and $\varphi_{k'l',n}$, $\varphi_{kl,n} - \varphi_{k'l',n}$ does not only depend on the difference between subscripts $l - l'$ and $k - k'$. This means the process on the array axis is not Wide Sense Stationary (WSS).

3.3 Array-Time Evolution Model

To describe the cluster evolution on both array and time axes, the proposed wideband ellipse model is further improved by combining the BD process on the time axis in [100]. As a result, an array-time evolution model is established. Additionally, geometrical relationships among the transmitter, the receiver, and the clusters need to be updated with time. An example of a cluster evolving on time axis is illustrated in Fig. 3.4. Both clusters and the Mobile Station (MS) are moving. Cluster_{*n*} and the receive antenna array move to new positions from $t = t_m$ to $t = t_{m+1}$. Distances and angle properties have to be updated based on geometrical relationships. It can be seen that AoD, AoA, and transmission distance will be time-variant because of the movement of the cluster and the terminal. Consequently, α_n^T , α_n^R , D_n^T , D_n^R , D_{ln}^T , D_{kn}^R , a_n , f , α_v , and τ_n become time-variant as $\alpha_n^T(t)$, $\alpha_n^R(t)$, $D_n^T(t)$, $D_n^R(t)$, $D_{ln}^T(t)$, $D_{kn}^R(t)$, $a_n(t)$, $f(t)$, $\alpha_v(t)$, and $\tau_n(t)$ correspondingly. Although there exists situations when Base Station (BS), MS, and clusters are all moving, it should be noticed that those situations can be equivalent to a static BS situation using the principles of relative motion.

In this case, assume Cluster_{*n*}, ($n = 1, 2, \dots, N$) moves in an arbitrary direction $\varphi_{c,n}$ with a speed of v_c at time instance $t = t_m$ ($m = 1, 2, \dots$), then at $t = t_{m+1}$, the instant distance between two focal points $f(t_{m+1})$ can be calculated as

$$2f(t_{m+1}) = [[2f(t_m)]^2 + [v(t_{m+1} - t_m)]^2 + 4f(t_m)v(t_{m+1} - t_m) \cos [\alpha_v(t_m)]]^{1/2}. \quad (3.29)$$

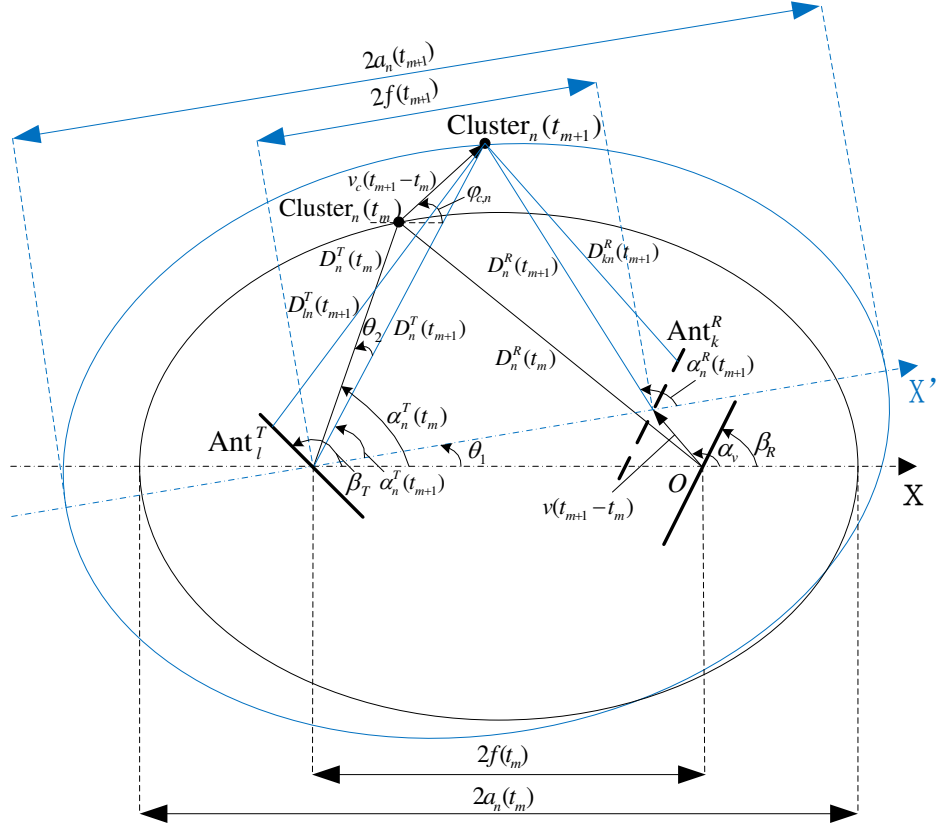


FIGURE 3.4: Geometrical relationship evolution from $t = t_m$ to $t = t_{m+1}$ of the ellipse model.

Accordingly, the distance between the transmitter and Cluster_{*n*}, $D_n^T(t)$, needs to be updated at $t = t_{m+1}$ as

$$D_n^T(t_{m+1}) = \left[\left[D_n^T(t_m) \right]^2 + v_c^2(t_{m+1} - t_m)^2 + 2D_n^T(t_m)v_c(t_{m+1} - t_m) \cos(\alpha_n^T(t_m) - \varphi_{c,n}) \right]^{1/2}. \quad (3.30)$$

Referencing the instant ellipse of Cluster_{*n*}(t_{m+1}), the instant AoD and the distance between Ant_{*l*}^{*T*} and Cluster_{*n*}, $D_{ln}^T(t_{m+1})$ can be obtained as

$$\alpha_n^T(t_{m+1}) = \alpha_n^T(t_m) - \theta_1 - \theta_2 \quad (3.31)$$

$$\theta_1 = \arcsin \left[\frac{v(t_{m+1} - t_m) \sin(\pi - \alpha_v(t_m))}{2f(t_{m+1})} \right] \quad (3.32)$$

$$\theta_2 = \arcsin \left[\frac{v_{c,n}(t_{m+1} - t_m) \sin(\pi - \alpha_n^T(t_m) + \varphi_{c,n})}{D_n^T(t_{m+1})} \right] \quad (3.33)$$

$$D_{ln}^T(t_{m+1}) = [D_n^T(t_{m+1})^2 + \left(\frac{M_T - 2l + 1}{2}\delta_T\right)^2 - D_n^T(t_{m+1})(M_T - 2l + 1)\delta_T \cos(\beta_T - \alpha_n^T(t_{m+1}))]^{1/2}. \quad (3.34)$$

Similarly, the distance between the receiver and Cluster_{*n*}, $D_n^R(t)$, the corresponding instant delay $\tau_n(t_{m+1})$, and the instant movement direction $\alpha_v(t_{m+1})$ of the receiver are derived as

$$D_n^R(t_{m+1}) = [[2f(t_{m+1})]^2 + [D_n^T(t_{m+1})]^2 - 4f(t_{m+1})D_n^T(t_{m+1})\cos(\alpha_n^T(t_{m+1}))]^{1/2} \quad (3.35)$$

$$2a_n(t_{m+1}) = D_n^T(t_{m+1}) + D_n^R(t_{m+1}) \quad (3.36)$$

$$\tau_n(t_{m+1}) = \tau_n(t_m) + \frac{2a_n(t_{m+1}) - 2a_n(t_m)}{c} \quad (3.37)$$

$$\alpha_v(t_{m+1}) = \alpha_v(t_m) - \theta_1. \quad (3.38)$$

Next, according to the law of sines, the AoA of Cluster_{*n*} at $t = t_{m+1}$, $\alpha_n^R(t_{m+1})$, the distance between Ant_{*k*}^{*R*} and Cluster_{*n*}, $D_{kn}^R(t_{m+1})$, and Doppler frequency $f_n(\alpha_n^R(t_{m+1}))$ are computed as

$$\alpha_n^R(t_{m+1}) = \arcsin \left[\frac{D_n^T(t_{m+1}) \sin[\alpha_n^T(t_{m+1})]}{D_n^R(t_{m+1})} \right] \quad (3.39)$$

$$D_{kn}^R(t_{m+1}) = [D_n^R(t_{m+1})^2 + \left(\frac{M_R - 2k + 1}{2}\delta_R\right)^2 - D_n^R(t_{m+1})(M_R - 2k + 1)\delta_R \cos(\alpha_n^R(t_{m+1}) - \beta_R + \theta_1)]^{1/2} \quad (3.40)$$

$$f_n(\alpha_n^R(t_{m+1})) = f_{\max} \cos(\alpha_n^R(t_{m+1}) - \alpha_v(t_{m+1})). \quad (3.41)$$

Besides geometrical relationships, cluster sets of each antenna evolve with time as well. Thus, the time-variant C_l^T , C_k^R , and N_{new} are denoted as $C_l^T(t)$, $C_k^R(t)$, and $N_{\text{new}}(t)$, respectively. The evolution of clusters on the time axis is modeled as a BD process [100]. Here, let $C_l^T(t_m)$ ($l = 1, 2, \dots, M_T; m = 0, 1, 2, \dots$) and $C_k^R(t_m)$ ($k = 1, 2, \dots, M_R; m = 0, 1, 2, \dots$) denote the cluster set for Ant_{*l*}^{*T*} and the cluster set

for Ant_k^R at time instant t_m . Then at the next time instant, each cluster member in set $\left\{ \left(\bigcup_{l=1}^{M_T} C_l^T(t_m) \right) \cup \left(\bigcup_{k=1}^{M_R} C_k^R(t_m) \right) \right\}$ evolves according to the BD process on the time axis. A survived cluster member will remain in cluster sets. On the other hand, a disappeared cluster member will be eliminated from all the cluster sets. Newly generated cluster members will be added to certain cluster sets according to the BD process on the array axis. To sum up, the algorithm is based on two main operations, the array-axis evolution and the time-axis evolution, an example is described as follows.

At the initial time instant $t = t_m$, array-axis evolution will be first operated. As Fig. 3.2 indicates, given $C_1^T(t_m)$ and $C_1^R(t_m)$, the cluster set of Ant_l^T is evolved from the cluster set of Ant_{l-1}^T , the cluster set of Ant_k^R is evolved from the cluster set of Ant_{k-1}^R

$$C_{l-1}^T(t_m) \xrightarrow{\text{E}} C_l^T(t_m) \quad 2 \leq l \leq M_T \quad (3.42)$$

$$C_{k-1}^R(t_m) \xrightarrow{\text{E}} C_k^R(t_m) \quad 2 \leq k \leq M_R. \quad (3.43)$$

Then, at the next time instant $t = t_{m+1}$, time-axis evolution is operated as proposed in [100]

$$C_l^T(t_m) \xrightarrow{\text{E}} C_l^T(t_{m+1}) \quad (3.44)$$

$$C_k^R(t_m) \xrightarrow{\text{E}} C_k^R(t_{m+1}). \quad (3.45)$$

To perform the evolution process of clusters on the time axis as (3.44) and (3.45) show, define channel fluctuation in time domain at $t = t_{m+1}$ as q_{m+1} . The channel fluctuation is a measure of how much the scattering environment has changed. Assuming that the receiver and clusters are moving with a constant velocity, q_{m+1} is defined as [100]

$$q_{m+1} = q_{x,m+1} + q_{t,m+1} \quad (3.46)$$

where $q_{x,m+1}$ is the fluctuation caused by the movement of receiver, which is defined as the distance the receiver moved with the time interval [100]

$$q_{x,m+1} = v(t_{m+1} - t_m) \quad (3.47)$$

and $q_{t,m+1}$ is the fluctuation caused by the movement of clusters (P_F is the percentage

of moving clusters, v_c is the velocity of clusters), which is defined as the distance the cluster moved with the time interval [100]

$$q_{t,m+1} = P_F v_c (t_{m+1} - t_m). \quad (3.48)$$

Given the scenario-dependent correlation factor D_c^s on the space axis, each cluster survives with probability P_{survival} , which can be calculated as [115]

$$P_{\text{survival}}(q_{m+1}) = e^{-\frac{\lambda_R q_{m+1}}{D_c^s}}. \quad (3.49)$$

New clusters are generated according the Poisson process. The mean number of newly generated clusters at time instant $t = t_{m+1}$ on the time axis $E[N_{\text{new}}(t_{m+1})]$ is presented as [115]

$$E[N_{\text{new}}(t_{m+1})] = \frac{\lambda_G}{\lambda_R} (1 - e^{-\frac{\lambda_R q_{m+1}}{D_c^s}}). \quad (3.50)$$

For survived clusters, their geometrical relationships are computed as from (3.29) to (3.41). On the other hand, the delays, mean power of newly generated clusters are randomly drawn according to [30], where delays and mean power are exponentially distributed. The AoAs of newly generated clusters obey the von Mises distribution. To decide which transmit (receive) antennas are able to observe a newly generated cluster, the newly generated cluster is first attached to one transmit (receive) antenna with a randomly drawn index, say the ν -th transmit (receive) antenna. Second, this cluster evolves to both ends of the transmit (receive) antenna array, $\nu + 1$ to M_T and $\nu - 1$ to 1 (or $\nu + 1$ to M_R and $\nu - 1$ to 1), based on the survival probabilities on the array axis P_{survival}^T (P_{survival}^R). Third, this cluster is added to antenna cluster sets if it survives on those corresponding antennas. Finally, all cluster sets $C_l^T(t_{m+1})$ and $C_k^R(t_{m+1})$ have been updated before entering the next time instant.

Prior to the derivation of STFCE, the time-variant transfer function $H_{kl}(\xi, t)$ of the channel can be expressed as [34]

$$H_{kl}(\xi, t) = \int_{-\infty}^{\infty} h_{kl}(t, \tau) e^{-j2\pi\xi\tau} d\tau$$

$$\begin{aligned}
 &= \int_{-\infty}^{\infty} \sum_{n=1}^{N_{\text{total}}} h_{kl,n}(t) \delta(\tau - \tau_n) e^{-j2\pi\xi\tau} d\tau \\
 &= \sum_{n=1}^{N_{\text{total}}} h_{kl,n}(t) e^{-j2\pi\xi\tau_n}
 \end{aligned} \tag{3.51}$$

where ξ is frequency. The normalised STFCF $\rho_{kl,k'l'}(\delta_T, \delta_R, \Delta\xi, \Delta t; \xi, t)$ can be calculated as [34]

$$\begin{aligned}
 \rho_{kl,k'l'}(\delta_T, \delta_R, \Delta\xi, \Delta t; \xi, t) &= \text{E} \left[\frac{H_{kl}^*(\xi, t) H_{k'l'}(\xi + \Delta\xi, t + \Delta t)}{|H_{kl}^*(\xi, t)| |H_{k'l'}(\xi + \Delta\xi, t + \Delta t)|} \right] \\
 &= \text{E} \left[\frac{\sum_{m=1}^{N_{\text{total}}} \sum_{n=1}^{N_{\text{total}}} h_{kl,m}^*(t) h_{k'l',n}(t + \Delta t) e^{j2\pi\xi\tau_m - j2\pi(\xi + \Delta\xi)\tau_n}}{|H_{kl}^*(\xi, t)| |H_{k'l'}(\xi + \Delta\xi, t + \Delta t)|} \right].
 \end{aligned} \tag{3.52}$$

With the Uncorrelated Scattering (US) assumption, i.e., clusters are mutually independent

$$\text{E} [h_{kl,m}^*(t) h_{k'l',n}(t + \Delta t)] = 0 \tag{3.53}$$

for $m \neq n$, the STFCF in (3.52) reduces to

$$\begin{aligned}
 \rho_{kl,k'l'}(\delta_T, \delta_R, \Delta\xi, \Delta t; t) &= \text{E} \left[\frac{\sum_{n=1}^{N_{\text{total}}} h_{kl,n}^*(t) h_{k'l',n}(t + \Delta t) e^{j2\pi\Delta\xi\tau_n}}{|H_{kl}^*(\xi, t)| |H_{k'l'}(\xi + \Delta\xi, t + \Delta t)|} \right] \\
 &= \sum_{n=1}^{N_{\text{total}}} \text{E} \left[\frac{h_{kl,n}^*(t) h_{k'l',n}(t + \Delta t) e^{j2\pi\Delta\xi\tau_n}}{|H_{kl}^*(\xi, t)| |H_{k'l'}(\xi + \Delta\xi, t + \Delta t)|} \right] \\
 &= \sum_{n=1}^{N_{\text{total}}} w_n \rho_{kl,k'l',n}(\delta_T, \delta_R, \Delta\xi, \Delta t; t)
 \end{aligned} \tag{3.54}$$

where $\{w_n\}$ are normalisation weights such that $\sum_{n=1}^{N_{\text{total}}} w_n \rho_{kl,k'l',n}(0, 0, 0, 0; t) = 1$ and the normalised STFCF for the n -th cluster $\rho_{kl,k'l',n}(\delta_T, \delta_R, \Delta\xi, \Delta t; t)$ is defined by

$$\rho_{kl,k'l',n}(\delta_T, \delta_R, \Delta\xi, \Delta t; t) = \mathbb{E} \left[\frac{h_{kl,n}^*(t)h_{k'l',n}(t + \Delta t)e^{j2\pi\Delta\xi\tau_n}}{|h_{kl,n}^*(t)||h_{k'l',n}(t + \Delta t)|} \right]. \quad (3.55)$$

By setting $l = l'$, $k = k'$, and $\Delta\xi = 0$, since a cluster has a probability of $e^{-\lambda_R \frac{v\Delta t + P_F v_c \Delta t}{D_c^s}}$ to survive from t to $t + \Delta t$, the time Autocorrelation Function (ACF) of the wideband ellipse massive MIMO of the n -th cluster with considerations on cluster evolution on the time axis, $\rho_{kl,n}(\Delta t; t)$, can be computed as

$$\begin{aligned} \rho_{kl,n}(\Delta t; t) &= \rho_{kl,k'l',n}(0, 0, 0, \Delta t; t) = \mathbb{E} \left[\frac{h_{kl,n}^*(t)h_{kl,n}(t + \Delta t)}{|h_{kl,n}^*(t)||h_{kl,n}(t + \Delta t)|} \right] \\ &= e^{-\lambda_R \frac{v\Delta t + P_F v_c \Delta t}{D_c^s}} \times \\ &\quad \int_{-\pi}^{\pi} e^{j[2\pi f_n(\alpha_n^R(t+\Delta t))(t+\Delta t) - 2\pi f_n(\alpha_n^R(t))t + \varphi_{kl,n}(t+\Delta t) - \varphi_{kl,n}(t)]} p_{\alpha_n^R}(\alpha_n^R) d\alpha_n^R \quad (3.56) \end{aligned}$$

where $\varphi_{kl,n}(t)$ and $f_n(\alpha_n^R(t))$ can be respectively calculated as given by (3.19) and (3.20) including time variations. As can be seen in (3.56), the time correlation function is time t dependent, hence the model is not WSS on the time axis.

By setting $l = l'$, $k = k'$, and $\Delta t = 0$, the STFCF in (3.52) reduces to the Frequency Correlation Function (FCF) $\rho_{kl}(\Delta\xi; t)$

$$\begin{aligned} \rho_{kl}(\Delta\xi; t) &= \rho_{kl,k'l'}(0, 0, \Delta\xi, 0; t) = \mathbb{E} \left[\frac{\sum_{n=1}^{N_{\text{total}}} h_{kl,n}^*(t)h_{k'l'}(t)e^{j2\pi\Delta\xi\tau_n}}{|H_{kl}^*(\xi, t)||H_{k'l'}(\xi + \Delta\xi, t)|} \right] \\ &= \mathbb{E} \left[\frac{\sum_{n=1}^{N_{\text{total}}} |h_{kl,n}(t)|^2 e^{j2\pi\Delta\xi\tau_n}}{|H_{kl}^*(\xi, t)||H_{kl}(\xi + \Delta\xi, t)|} \right]. \quad (3.57) \end{aligned}$$

3.4 A Wideband Ellipse Simulation Model for Massive MIMO

The purpose of a simulation model is to obtain a reasonable trade-off between the accuracy of the model and the complexity, i.e., approaching channel characteristics (space CCF and time ACF) as precise as possible with a limited number of rays within a cluster. As a result, in a NLOS scenario, (3.3) becomes

$$h_{kl,n}(t) = \sqrt{\frac{P_n}{S}} \sum_{i=1}^S e^{j(2\pi f_{n,i}t + \varphi_{kl,n,i})}. \quad (3.58)$$

As $f_{n,i}$ and $\varphi_{kl,n,i}$ are all functions of AoA, we need to find S rays with different AoAs to achieve the simulation model. Given that AoAs obey the von Mises distribution which can be characterised by its PDF [118]

$$p_{\alpha_n^R}(\alpha_n^R) = \frac{\exp[\kappa \cos(\alpha_n^R - \bar{\alpha}_n^R)]}{2\pi I_0(\kappa)} \quad \alpha_n^R \in [-\pi, \pi] \quad (3.59)$$

where $I_0(\cdot)$ is the zero-th order modified Bessel function, $\bar{\alpha}_n^R$ is the mean and $\kappa \geq 0$ controls the width of the distribution. In the theoretical model, let $g(\alpha_n^R) = \frac{h_{kl,n}^*(t)h_{k'l',n}(t+\Delta t)}{|h_{kl,n}^*(t)||h_{k'l',n}(t+\Delta t)|}$ with α_n^R distributed according to the von Mises distribution whose PDF is as (3.59) shows. Furthermore, denote the CDF of the von Mises distribution as $F(\alpha_n^R)$. Then, the space-time correlation function equals The expectation of $g(\alpha_n^R)$ which can be calculated as

$$\rho_{kl,k'l',n}(\delta_T, \delta_R, \Delta t; t) = \mathbb{E}[g(\alpha_n^R)] = \int g(\alpha_n^R) dF(\alpha_n^R). \quad (3.60)$$

On the other hand, a simulation model aims at approximating $\rho_{kl,k'l',n}(\delta_T, \delta_R, \Delta t; t)$ with S discrete AoAs $\{\alpha_{n,i}^R\}_{i=1}^S$. Each $\alpha_{n,i}^R$ follows the CDF $F(\alpha_n^R)$. Then, the approximated value $\hat{\rho}_{kl,k'l',n}(\delta_T, \delta_R, \Delta t; t)$ can be expressed as

$$\hat{\rho}_{kl,k'l',n}(\delta_T, \delta_R, \Delta t; t) = \frac{1}{S} \sum_{i=1}^S g(\alpha_{n,i}^R). \quad (3.61)$$

The problem remains to determine the $\{\alpha_{n,i}^R\}$ with reasonable computational complexity to approximate $\rho_{kl,k'l',n}$ with $\hat{\rho}_{kl,k'l',n}$. With the Method of Equal Area (MEA) [34], $F(\alpha_n^R)$ is divided into S intervals with same probabilities, then $\alpha_{n,i}^R$ can be computed as $\alpha_{n,i}^R = F^{-1}(\frac{i}{S})$, where $F^{-1}(\cdot)$ is the inverse function of $F(\cdot)$. Although the CDF and inverse CDF of the von Mises distribution is not analytic, $\alpha_{n,i}^R$ can be determined numerically.

3.5 Numerical Analysis

In this section, numerical results of the proposed model will be analysed. To perform numerical analysis, delays and mean power of clusters are assumed to be generated according to the urban macro-cell scenario in [30] where both of them follow the exponential distributions. AoAs of clusters to the receive array center are assumed to be von Mises distributed.

The normalised Doppler Power Spectral Density (PSD) of the proposed model is shown in Fig. 3.5. It should be noticed that the normalised Doppler PSD of the proposed massive MIMO channel model is not symmetric with respect to 0, because the decreasing correlation factor on temporal ACF resulting from cluster evolution serves as a shift in the Fourier transform domain. Doppler PSD of simulations and simulation models align well with the theoretical model, demonstrating the correctness of derivations of the theoretical model.

The receiver absolute space CCF $|\rho_{k1,k'1,1}(0, \delta_R; t)|$ of the ellipse model under spherical assumption in terms of different values of (k', k) pairs with $|k' - k| = 1$ is illustrated in Fig. 3.6. It can be observed that the receive antenna correlation slowly decreases as the normalised antenna spacing increases. The numerical results of the receive antenna correlation curves of the proposed model are compared with measurement on receiver correlation of massive MIMO in [1], showing that they share a similar trend. It should be noted that the measurement on receiver correlation in [1] was obtained via single experiment. Most importantly, it can be realised that correlation functions of different values of k' and k with $|k' - k| = 1$ are different. The correlation function

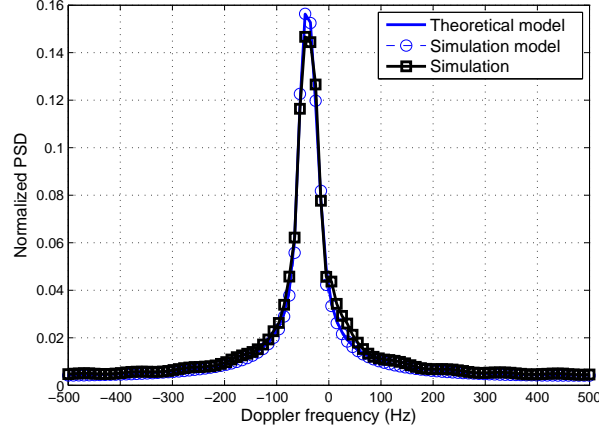


FIGURE 3.5: Normalised Doppler PSD of the theoretical model, the simulation model, and simulations. ($M_R = 32, M_T = 1, t = 1\text{s}, a_1 = 100\text{m}, f = 80\text{m}, D_c^a = 30\text{m}, D_c^s = 50\text{m}, \beta_R = \beta_T = \pi/2, \lambda = 0.12\text{m}, f_{\max} = 33.33\text{Hz}, \alpha_v = \pi/6, \kappa = 9, \bar{\alpha}_n^R = \pi/3, \text{NLOS}$).

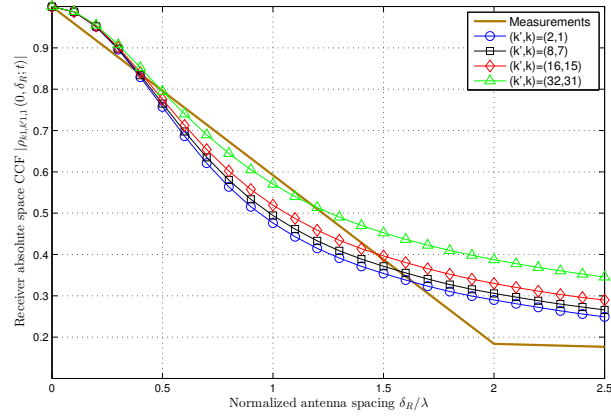


FIGURE 3.6: Absolute receiver space CCF $|\rho_{k1,k'1,1}(0, \delta_R; t)|$ of the ellipse model under von Mises assumption in terms of different values of (k', k) pairs with $|k' - k| = 1$. ($M_R = 32, M_T = 1, t = 1\text{s}, a_1 = 100\text{m}, f = 80\text{m}, D_c^a = 30\text{m}, D_c^s = 50\text{m}, \beta_R = \beta_T = \pi/2, \lambda = 0.12\text{m}, f_{\max} = 33.33\text{Hz}, \alpha_v = \pi/6, \kappa = 5, \bar{\alpha}_n^R = \pi/3, \text{NLOS}$).

does not only depend of the absolute difference between antenna indices but also the indices of reference antennas, which means the WSS properties on the antenna array axis are not valid under the spherical wavefront assumption. The absolute space CCF $|\rho_{11,22,1}(\delta_T, \delta_R; t)|$ of the ellipse model under spherical assumption has been illustrated in Fig. 3.7. It can be observed that the spatial correlation gradually drops when the normalised antenna spacing increases.

Furthermore, an example of cluster evolution on the array axis has been depicted

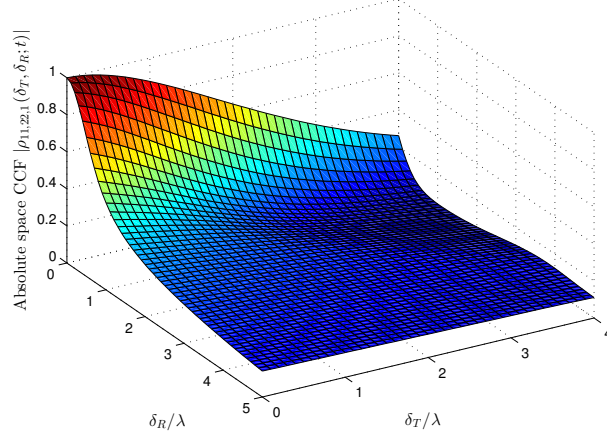


FIGURE 3.7: Absolute space CCF $|\rho_{11,22,1}(\delta_T, \delta_R; t)|$ of the ellipse model. ($M_R = M_T = 32$, $t = 1\text{s}$, $a_1 = 100\text{m}$, $f = 80\text{m}$, $D_c^a = 30\text{m}$, $D_c^s = 50\text{m}$, $\beta_R = \beta_T = \pi/2$, $\lambda = 0.15\text{m}$, $f_{\max} = 33.33\text{Hz}$, $\alpha_v = \pi/6$, $\kappa = 5$, NLOS).

in Fig. 3.8. Originally there are 20 clusters (Cluster₁ to Cluster₂₀) observable to the first antenna element. Then, these clusters evolve according to the BD process and probabilities described in Section 3.2.1. It can be observed that 4 (Cluster₁₀, Cluster₁₄, Cluster₁₅ and Cluster₂₀) of the original 20 clusters disappear during the evolution process and 5 new clusters (Cluster₂₁ to Cluster₂₅) have been generated. As a result, different antenna elements may observe different cluster sets. The cluster sets of the 4th and the 31st receive antennas C_4^R and C_{31}^R , for instance, share 18 common clusters. It should be noticed that, unlike conventional MIMO channel models, only a total cluster number of a cluster set is not sufficient to represent the properties of the cluster. The cluster members inside a cluster set as well as their properties such as delay, AoA and cluster power should be considered when calculating the channel coefficients in (3.3).

Fig. 3.9 and Fig. 3.10 show the normalised Angular Power Spectrum (APS) of AoA of the wideband ellipse model for both NLOS and LOS scenarios. The value of λ_R is set as $4/\text{m}$, the values of λ_G are chosen as $80/\text{m}$ and $32/\text{m}$ for NLOS and LOS cases, respectively. Hence, the mean numbers of clusters are aligned with NLOS (20 clusters) and LOS (8 clusters) cases in the WINNER II model. The AoAs are estimated using the well-known Multiple Signal Classification (MUSIC) algorithm [119], [120] with a sliding window formed by 3 consecutive antennas. This sliding window is

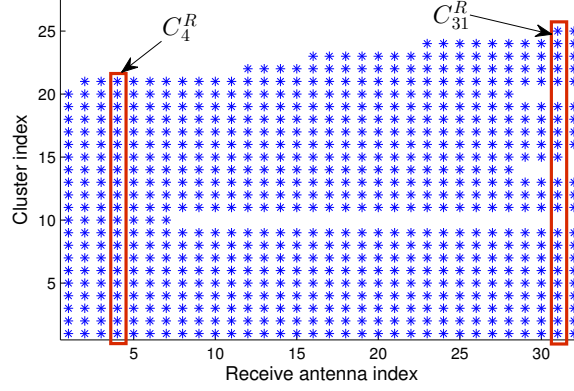


FIGURE 3.8: An example of cluster evolution on the receive antenna array. (A ‘*’ symbol in the two dimensional plane means its corresponding antenna element (coordinate on the horizontal direction) is able to observe its corresponding cluster (coordinate on the vertical direction).)

shifted by 1 antenna at a time, from the first antenna to the last antenna. Therefore, for a 32-element antenna array, there are in total 30 window positions as Fig. 3.9 and Fig. 3.10 illustrate. Three properties can be observed via these two figures. First, it can be observed that several estimated AoAs gradually change along the array axis. This phenomenon is mainly caused by the spherical wavefront assumption when the distances between their corresponding clusters and the antenna array do not fulfill the farfield assumption. Consequently, the AoAs of these clusters are no longer constant on every antenna element. Second, it is the BD process that models the dynamic properties of clusters and the non-stationarities on the array axis, where the appearance and disappearance of clusters can be seen in both figures. Different antenna elements may observe different sets of clusters, and the life periods of these clusters are continuous on the array axis.

The CDF of the average life periods of clusters on the array axis is illustrated in Fig. 3.11. It shows the survival probability of a cluster decreases exponentially as evolving on the array axis. Third, the power variations of each cluster result in imbalanced received power on the array axis. To study this phenomenon, let p_k ($k = 1, \dots, M_R$) denote the received power of Ant_k^R , then the maximum received power difference Δp_{\max}^R is defined as

$$\Delta p_{\max}^R (\text{dB}) = 10 \log_{10} \frac{\max \{p_1, p_2, \dots, p_{M_R}\}}{\min \{p_1, p_2, \dots, p_{M_R}\}}. \quad (3.62)$$

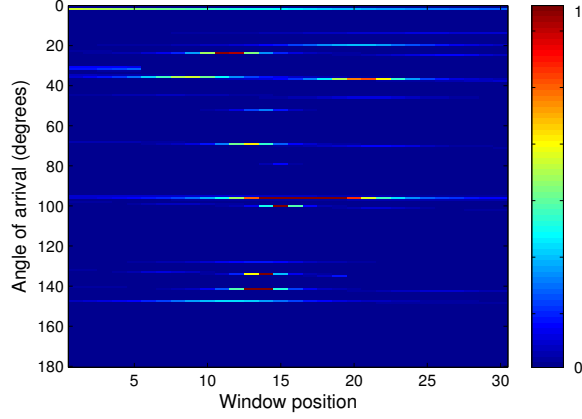


FIGURE 3.9: A snapshot example of the normalised angle power spectrum of AoA of the wideband ellipse model. ($M_R = 32, M_T = 1, a_1 = 100\text{m}, f = 80\text{m}, D_c^a = 30\text{m}, D_c^s = 50\text{m}, \beta_R = \beta_T = \pi/2, \lambda = 0.15\text{m}, \delta_R = 0.5\lambda, f_{\max} = 0\text{Hz}$, NLOS, $\lambda_G = 80/\text{m}$, $\lambda_R = 4/\text{m}, P_F = 0.3$).

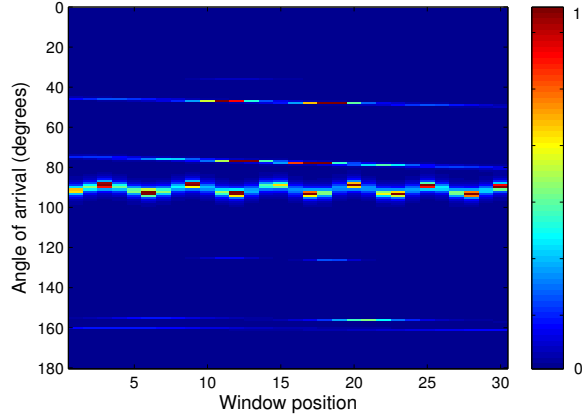


FIGURE 3.10: A snapshot example of the normalised angle power spectrum of AoA of the wideband ellipse model. ($M_R = 32, M_T = 1, a_1 = 100\text{m}, f = 80\text{m}, D_c^a = 30\text{m}, D_c^s = 50\text{m}, \beta_R = \beta_T = \pi/2, \lambda = 0.15\text{m}, \delta_R = 0.5\lambda, f_{\max} = 0\text{Hz}$, LOS $K = 3\text{dB}, \lambda_G = 32/\text{m}, \lambda_R = 4/\text{m}, P_F = 0.3$).

After 200 trials, the CDF of the the maximum received power difference in difference conditions of correlation factors on array and space axes can be observed in Fig. 3.12. It shows a difference of approximately 2 – 3dB between the maximum and minimum received power over the antenna array, which is normally not investigated in conventional plane wavefront MIMO channel models. Also, the received power difference on the array axis increases as the correlation factor reduces. Similar conclusions on received power imbalance can be found in [1] and [87].

The absolute receiver space CCFs of the wideband ellipse model with different BD

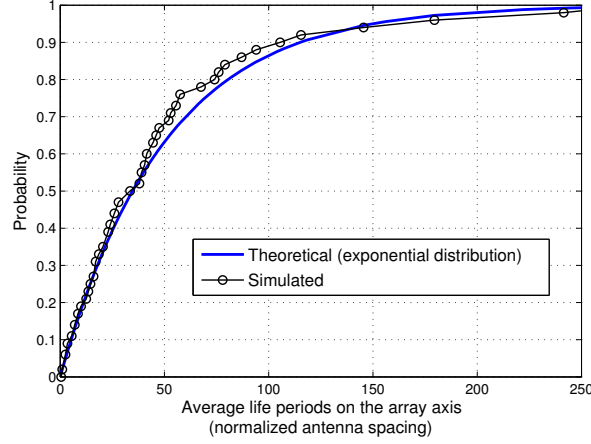


FIGURE 3.11: Cumulative distribution function of average life periods of clusters on the array axis in terms of normalised antenna spacing. ($D_c^a = 30\text{m}$, $D_c^s = 50\text{m}$, $\lambda = 0.15\text{m}$, $\delta_R = 0.5\lambda$, NLOS, $\lambda_G = 80/\text{m}$, $\lambda_R = 4/\text{m}$, $P_F = 0.3$).

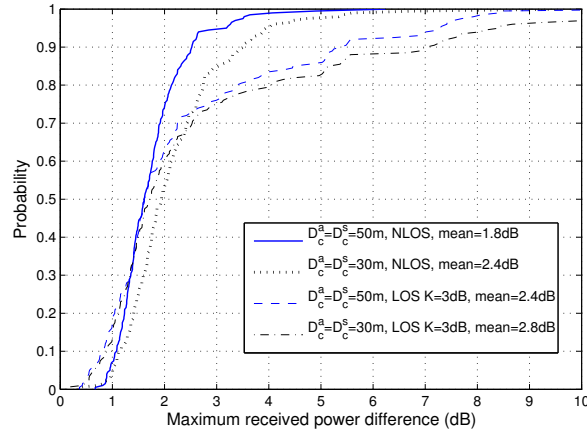


FIGURE 3.12: Cumulative distribution function of the maximum power difference over the antenna array under different LOS/NLOS conditions and correlation factors on array and space axes. ($M_R = 32$, $M_T = 1$, $a_1 = 100\text{m}$, $f = 80\text{m}$, $\beta_R = \beta_T = \pi/2$, $\lambda = 0.15\text{m}$, $\delta_R = 0.5\lambda$, $f_{\max} = 0\text{Hz}$, von Mises distributed AoA).

process configurations is illustrated in Fig. 3.13. It can be observed that the correlation with cluster evolution on the array axis is lower than that without considering array evolution, because a certain number of clusters would fail to survive when they evolve on the array axis. Also, the gap between the two curves increases as the antenna separation grows because of a lower probability for a cluster to survive. Finally, the time-variant characteristic has been shown in Fig. 3.14. It can be observed that the absolute time ACF varies along with time and hence the numerical result demonstrates time non-stationarities of the model.

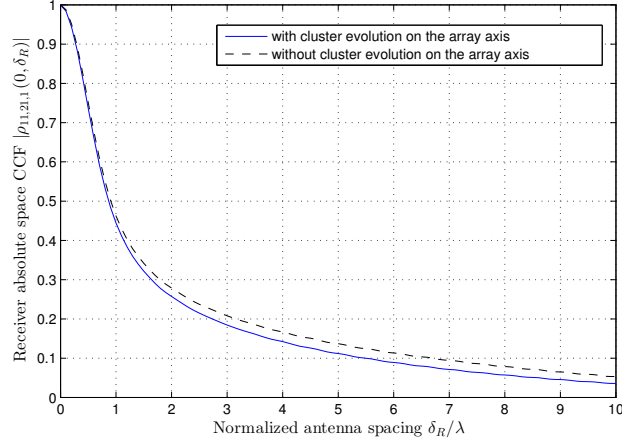


FIGURE 3.13: Absolute receiver space CCF $|\rho_{11,21,1}(0, \delta_R; t)|$ of the wideband ellipse model. ($M_R = 32, M_T = 1, t = 1\text{s}, a_1 = 100\text{m}, f = 80\text{m}, D_c^a = 15\text{m}, D_c^s = 50\text{m}, \beta_R = \beta_T = \pi/2, \lambda = 0.15\text{m}, \delta_R = 0.5\lambda, f_{\max} = 0\text{Hz}, \text{NLOS}, \lambda_G = 80/\text{m}, \lambda_R = 4/\text{m}, P_F = 0.3, \kappa = 5$).

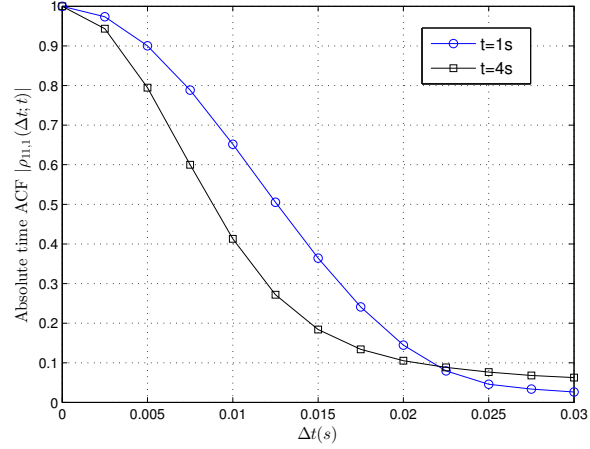


FIGURE 3.14: Absolute time ACF of Cluster₁ $|\rho_{11,1}(\Delta t; t)|$ in (3.56) comparison between $t = 1\text{s}$ and $t = 4\text{s}$ with BD process. ($M_R = 32, M_T = 32, a_1 = 100\text{m}, f = 80\text{m}, D_c^a = 15\text{m}, D_c^s = 50\text{m}, \beta_R = \beta_T = \pi/2, \lambda = 0.15\text{m}, \delta_R = \delta_T = 0.5\lambda, f_{\max} = 33.33\text{Hz}, v_c = 0.5\text{m/s}, \text{NLOS}, \lambda_G = 80/\text{m}, \lambda_R = 4/\text{m}, P_F = 0.3, \kappa = 5$).

Fig. 3.15 compares the FCF between NLOS and LOS scenarios. It can be seen that the FCF of NLOS decreases significantly with the frequency difference whose 50% coherence bandwidth is approximately 1.2 MHz. On the other hand, the LOS scenario has a larger 50% coherence bandwidth because the LOS component dominates the power of the channel.

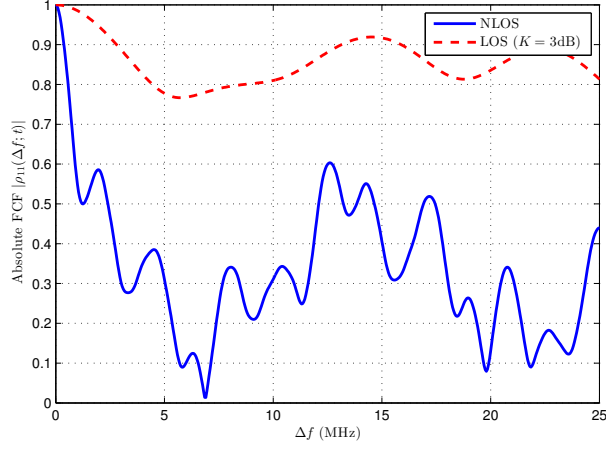


FIGURE 3.15: Absolute FCF $|\rho_{11}(\Delta\xi; t)|$ comparison between NLOS and LOS. ($M_R = 32, M_T = 32, a_1 = 100\text{m}, f = 80\text{m}, D_c^a = 15\text{m}, D_c^s = 50\text{m}, \beta_R = \beta_T = \pi/2, \lambda = 0.15\text{m}, \delta_R = \delta_T = 0.5\lambda, f_{\max} = 33.33\text{Hz}, v_c = 0.5\text{m/s}, \lambda_G = 80/\text{m}, \lambda_R = 4/\text{m}, P_F = 0.3, \kappa = 5.$)

3.6 Summary

A novel 2-D wideband ellipse channel model with non-stationarities on both time and array axes for massive MIMO communication systems has been proposed in this chapter. Spherical wavefront has been assumed in the proposed model illustrating the difference of spatial correlation properties compared with the plane wavefront assumption used in conventional MIMO channel models. It has been demonstrated that WSS properties are not available under the spherical wavefront assumption. Additionally, BD process has been applied to both time and array axes in order to model the non-stationary behaviors of clusters on both axes. In this case, different cluster sets can be observable to different antenna elements in this model. Finally, based on the numerical analysis, the proposed model has shown that there are non-stationarities and dynamic properties of clusters on the antenna array in massive MIMO channels, where similar conclusions have also been drawn in measurements [1] and [87]. For future work, certain parameters of the proposed channel model may be extracted via measurements. Also, since GBSMs do not depend on configurations of antenna arrays, polarised antenna arrays can be employed in future extensions of the channel model.

Chapter 4

A Non-Stationary 3-D Twin-Cluster Model for Massive MIMO Channels

4.1 Introduction

In Chapter 3, a Two-Dimensional (2-D) Geometry-Based Stochastic Model (GBSM) was proposed for massive Multiple-Input Multiple-Output (MIMO) channels. However, it was reported in [49] that scatterers would disperse in elevation (or the vertical plane) and the impact of elevation angles needed to be addressed in realistic channel models. Therefore, Three-Dimensional (3-D) channel models should be developed for massive MIMO systems. Extensive conventional 3-D MIMO models can be found in the literature such as the twin-cluster MIMO model [50], the COST 2100 model [31], [33], 3-D extension of the WINNER model [60], 3-D double-directional radio model [58], and 3-D MIMO Vehicle-to-Vehicle (V2V) channel model [56]. In this chapter, we will extend the twin-cluster MIMO model in [50], where a cluster was divided into two representations of itself (one at the transmitter and the other at the receiver), by incorporating the spherical wavefront assumption, cluster evolution on the time and array axes, and 3-D cluster properties to capture massive MIMO channel characteristics.

The **contributions** of this chapter are summarised as follows:

1. This chapter first proposes a theoretical non-stationary 3-D wideband twin-cluster channel model for massive MIMO systems with carrier frequencies in the order of gigahertz (GHz), i.e., they are not applicable to millimeter wave communication systems. To the best of the authors' knowledge, this is the first 3-D model for massive MIMO channels. An infinite number of scatterers is assumed in the proposed theoretical model (or reference model), which cannot be implemented in hardware or for simulation purposes. Therefore, we also propose a corresponding 3-D simulation model with finite numbers of scatterers. Various statistical properties, such as the Space-Time Correlation Function (STCF), Doppler Power Spectral Density (PSD), and condition number, are studied for both the theoretical and simulation models. Numerical results have demonstrated that the statistical properties of the simulation model can fit those of the theoretical model very well with reasonable complexity. Also, the impact of cluster elevation angles on correlation properties of the proposed massive MIMO channel models is investigated.
2. In the proposed theoretical and simulation massive MIMO channel models, nearfield effects caused by the increasing antenna elements are considered, including the spherical wavefront assumption and the variation of Doppler frequencies over the antenna array.
3. Also, appearance and disappearance of clusters (i.e., cluster evolution) on both the array and time axes are jointly modeled by Birth-Death (BD) processes, which make the proposed massive MIMO channel models essentially non-stationary.

The rest of this chapter is organised as follows. Section 4.2 gives a general description of the proposed theoretical non-stationary 3-D wideband twin-cluster channel model for massive MIMO systems. Statistical properties of the proposed theoretical model are studied in Section 4.3. Section 4.4 presents the corresponding simulation model for the theoretical model. Numerical results are presented in Section 4.5 and conclusions are finally drawn in Section 4.6.

4.2 A Theoretical Non-Stationary 3-D Wideband Twin-Cluster Massive MIMO Channel Model

Let us consider a wideband massive MIMO system with multiple twin clusters in a 3-D space to describe different taps of the channel, as illustrated in Fig. 4.1. For a twin-cluster channel model with N_{total} clusters, each cluster, say Cluster $_n$ ($n = 1, \dots, N_{\text{total}}$), is made of a representation Cluster $_n^T$ at the transmitter side denoting the first bounce and a representation Cluster $_n^R$ at the receiver side denoting the last bounce. The propagation environment between these two representations is abstracted as a virtual link [50].

Let us assume that the transmitter and receiver are equipped with Uniform Linear Arrays (ULAs) with M_T and M_R antenna elements, respectively. It should be mentioned that the calculations of channel coefficients depend only on geometry relationships between objects in the model and are independent to the layout of antenna arrays. Therefore, although co-located ULAs are used in this chapter for presentation convenience, the same modeling approach can be generalised to distributed antenna arrays or 2-D antenna arrays.

The distances between antenna elements are δ_T at the transmitter and δ_R at the receiver. Let the transmitter be the origin of the 3-D space, the distance vector between the transmitter and receiver is $\mathbf{D} = (D, 0, 0)$. Furthermore, both azimuth and elevation angles in the 3-D space are considered for clusters, antenna arrays, movement direction of clusters, and movement direction of antenna arrays as listed in Table 4.1. It should be noticed that the farfield conditions ($D > \frac{2M_T^2\delta_T^2}{\lambda}$, $D > \frac{2M_R^2\delta_R^2}{\lambda}$) for conventional MIMO channels are not assumed in the proposed model. Thus, the wavefront of each wireless link is assumed to be spherical resulting in the fact that the Angles of Arrival (AoAs) and Angles of Departure (AoDs) on the antenna arrays are no longer equal for each antenna element and the phase of each antenna element is determined by geometrical relationships.

Another important characteristic of massive MIMO channel models is the appearance and disappearance of clusters on the antenna array as reported in [1]. Contrary to

conventional MIMO channel models assuming that a cluster is always observable to all the antennas on an antenna array, a cluster may only be observable to a subset of antennas on an antenna array for massive MIMO. To put it another way, *each antenna has its own set of observable clusters*. Examples are shown in Fig. 4.1. Cluster_{*n*+1} is observable to the *k*-th but not observable to the *q*-th ($1 \leq k, q \leq M_R$) receive antenna. Similarly, Cluster_{*n*+2} is observable to the *l*-th but not observable to the *p*-th ($1 \leq l, p \leq M_T$) transmit antenna. On the other hand, Cluster_{*n*} is observable to both the *l*-th transmit antenna and the *k*-th receive antenna. Denote $C_l^T(t)(C_k^R(t))$ as the cluster set in which clusters are observable to the *l*-th transmit antenna (the *k*-th receive antenna) at time instant *t*. Let N_{total} be the total number of clusters that are observable to at least one transmit antenna and one receive antenna. The value of N_{total} can be calculated as

$$N_{\text{total}} = \text{card} \left(\bigcup_{l=1}^{M_T} \bigcup_{k=1}^{M_R} (C_l^T(t) \cap C_k^R(t)) \right). \quad (4.1)$$

where the operator $\text{card}(\cdot)$ denotes the cardinality of a set. Then, a cluster is observable to the *l*-th transmit antenna and the *k*-th receive antenna if and only if this cluster is in the set $\{C_l^T(t) \cap C_k^R(t)\}$. Sets $C_l^T(t)$ and $C_k^R(t)$ are generated based on the cluster evolution (BD process) on both the time and array axes as described in Section 4.2.2.

TABLE 4.1: Definitions of key geometry parameters for the 3-D twin-cluster model.

v_E^R, v_E^T	elevation angles of the receive and transmit antenna arrays
v_A^R, v_A^T	azimuth angles of the receive and transmit antenna arrays
$\xi_{n,i_1}^R, \theta_{n,i_1}^R$	elevation and azimuth angles of the <i>i</i> ₁ -th ray of the <i>n</i> -th cluster at the receiver side
$\xi_{n,i_2}^T, \theta_{n,i_2}^T$	elevation and azimuth angles of the <i>i</i> ₂ -th ray of the <i>n</i> -th cluster at the transmitter side
$\text{Ant}_l^T, \text{Ant}_k^R$	the <i>l</i> -th transmit antenna and the <i>k</i> -th receive antenna
$\mathbf{D}_n^R(t), \mathbf{D}_n^T(t)$	distance vectors between the <i>n</i> -th cluster and the receiver (transmitter)
$\mathbf{D}_{n,i_1}^R(t)$	distance vector between the <i>n</i> -th cluster and the receive antenna array via the <i>i</i> ₁ -th ray
$\mathbf{D}_{kn,i_1}^R(t)$	distance vector between the <i>n</i> -th cluster and Ant_k^R via the <i>i</i> ₁ -th ray
$\mathbf{D}_{n,i_2}^T(t)$	distance vector between the <i>n</i> -th cluster and the transmit antenna array via the <i>i</i> ₂ -th ray
$\mathbf{D}_{ln,i_2}^T(t)$	distance vector between the <i>n</i> -th cluster and Ant_l^T via the <i>i</i> ₂ -th ray
$\mathbf{D}_{kl}^{\text{LOS}}(t)$	distance vector between Ant_k^R and Ant_l^T
\mathbf{v}	velocity vector of the receive antenna array
$\mathbf{v}_n^R, \mathbf{v}_n^T$	velocity vectors of the <i>n</i> -th cluster at the receiver and transmitter side

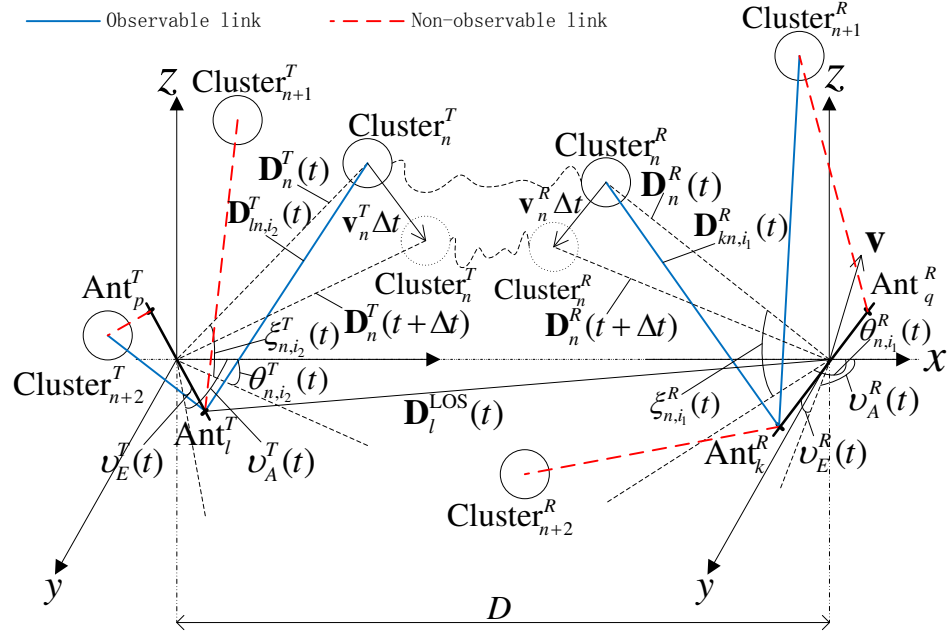


FIGURE 4.1: A 3-D wideband twin-cluster massive MIMO channel model.

4.2.1 Channel impulse response

Next, let us denote the maximum Doppler frequency as f_{\max} , the Line-of-Sight (LOS) Rician factor as K , and the initial phase of the signal at the transmitter as φ_0 . Additionally, let us assume that the power of the n -th cluster is P_n and there are respectively S_1 and S_2 rays within the representation at the receiver side and the representation at the transmitter side. Based on geometrical parameters in Table 4.1, as $S_1, S_2 \rightarrow \infty$, the theoretical model of the wideband massive MIMO channel matrix can be represented as an $M_R \times M_T$ complex matrix $\mathbf{H}(t, \tau) = [h_{kl}(t, \tau)]_{M_R \times M_T}$ where $k = 1, 2, \dots, M_R$ and $l = 1, 2, \dots, M_T$. The multipath complex gains between the l -th transmit antenna and the k -th receive antenna at time t and delay τ , $h_{kl}(t, \tau)$, can be presented as

$$h_{kl}(t, \tau) = \sum_{n=1}^{N_{\text{total}}} h_{kl,n}(t) \delta(\tau - \tau_n(t)) \quad (4.2)$$

-if $\text{Cluster}_n \in \{C_l^T(t) \cap C_k^R(t)\}$,

$$h_{kl,n}(t) = \underbrace{\delta(n-1) \sqrt{\frac{K}{K+1}}}_{\text{LOS}} e^{j(2\pi f_{kl}^{\text{LOS}} t + \varphi_{kl}^{\text{LOS}})}$$

$$+ \underbrace{\sqrt{\frac{P_n}{K+1}} \lim_{S_1, S_2 \rightarrow \infty} \sum_{i_1=1}^{S_1} \sum_{i_2=1}^{S_2} \frac{e^{j(2\pi f_{kn, i_1} t + \varphi_{kl, n, i_1 i_2})}}{\sqrt{S_1 S_2}}}_{\text{NLOS}} \quad (4.3)$$

-if $\text{Cluster}_n \notin \{C_l^T(t) \cap C_k^R(t)\}$,

$$h_{kl, n}(t) = 0. \quad (4.4)$$

The calculation of complex gains can be divided into Non-LOS (NLOS) components and LOS component.

4.2.1.1 For NLOS components

The k -th receive antenna vector $\mathbf{A}_k^R(t)$ and the vector between the n -th cluster and the receive antenna array via the i_1 -th ray $\mathbf{D}_{n, i_1}^R(t)$ can be presented as

$$\mathbf{A}_k^R(t) = \frac{M_R - 2k + 1}{2} \delta_R \begin{bmatrix} \cos v_E^R(t) \cos v_A^R(t) \\ \cos v_E^R(t) \sin v_A^R(t) \\ \sin v_E^R(t) \end{bmatrix}^T + \mathbf{D} \quad (4.5)$$

$$\mathbf{D}_{n, i_1}^R(t) = D_n^R(t) \begin{bmatrix} \cos \xi_{n, i_1}^R(t) \cos \theta_{n, i_1}^R(t) \\ \cos \xi_{n, i_1}^R(t) \sin \theta_{n, i_1}^R(t) \\ \sin \xi_{n, i_1}^R(t) \end{bmatrix}^T + \mathbf{D}. \quad (4.6)$$

Similarly, the l -th transmit antenna vector \mathbf{A}_l^T and the vector between the n -th cluster and the transmit antenna array via the i_2 -th ray $\mathbf{D}_{n, i_2}^T(t)$ can be given as

$$\mathbf{A}_l^T = \frac{M_T - 2l + 1}{2} \delta_T \begin{bmatrix} \cos v_E^T \cos v_A^T \\ \cos v_E^T \sin v_A^T \\ \sin v_E^T \end{bmatrix}^T \quad (4.7)$$

$$\mathbf{D}_{n, i_2}^T(t) = D_n^T(t) \begin{bmatrix} \cos \xi_{n, i_2}^T(t) \cos \theta_{n, i_2}^T(t) \\ \cos \xi_{n, i_2}^T(t) \sin \theta_{n, i_2}^T(t) \\ \sin \xi_{n, i_2}^T(t) \end{bmatrix}^T. \quad (4.8)$$

Then, vectors $\mathbf{D}_{kn,i_1}^R(t)$ and $\mathbf{D}_{ln,i_2}^T(t)$ can be computed as

$$\mathbf{D}_{kn,i_1}^R(t) = \mathbf{D}_{n,i_1}^R(t) - \mathbf{A}_k^R(t) \quad (4.9)$$

$$\mathbf{D}_{ln,i_2}^T(t) = \mathbf{D}_{n,i_2}^T(t) - \mathbf{A}_l^T. \quad (4.10)$$

Next, the delay of the n -th cluster of the twin-cluster model is assumed to be the sum of two components. The first component is calculated according to the geometrical relationships between the antenna arrays and cluster locations. The second component abstracts the delay of the virtual link between the twin clusters. Then, the delay of the n -th cluster $\tau_n(t)$ can be computed as

$$\tau_n(t) = \frac{\|\mathbf{D}_n^T(t)\| + \|\mathbf{D}_n^R(t)\|}{c} + \tilde{\tau}_n(t) \quad (4.11)$$

where the abstracted delay of the virtual link $\tilde{\tau}_n(t)$ is randomly drawn according to the uniform distribution $U(D/c, \tau_{\max})$, and τ_{\max} is the maximum delay ($\tau_{\max} = 1845$ ns for NLOS [30]). The operator $\|\cdot\|$ denotes the Euclidean norm, and c is the speed of light. Then, the phase between the k -th receive antenna and the l -th transmit antenna via the i_1 -th ray at the receiver, the i_2 -th ray at the transmitter, and the n -th cluster, $\varphi_{kl,n,i_1i_2}(t)$, is derived as

$$\varphi_{kl,n,i_1i_2}(t) = \varphi_0 + \frac{2\pi}{\lambda} [\|\mathbf{D}_{kn,i_1}^R(t)\| + \|\mathbf{D}_{ln,i_2}^T(t)\| + c\tilde{\tau}_n(t)]. \quad (4.12)$$

Accordingly, the Doppler frequency of the k -th receive antenna via the i_1 -th ray of the n -th cluster $f_{kn,i_1}(t)$ is presented as

$$f_{kn,i_1}(t) = \frac{f_{\max} \langle \mathbf{D}_{kn,i_1}^R(t), \mathbf{v} \rangle}{\|\mathbf{D}_{kn,i_1}^R(t)\| \|\mathbf{v}\|} \quad (4.13)$$

where $\langle \cdot, \cdot \rangle$ represents the inner product.

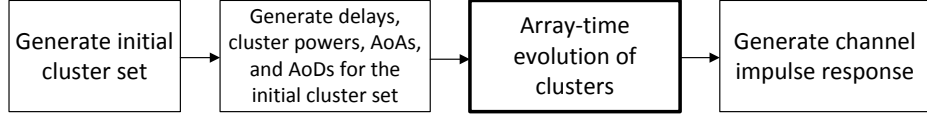


FIGURE 4.2: Algorithm flowchart of the generation of the channel impulse response.

4.2.1.2 For LOS component

In the same way, the Doppler frequency $f_{kl}^{\text{LOS}}(t)$ and phase $\varphi_{kl}^{\text{LOS}}(t)$ of the LOS components can also be calculated as

$$\mathbf{D}_{kl}^{\text{LOS}}(t) = \mathbf{A}_k^R(t) - \mathbf{A}_l^T \quad (4.14)$$

$$f_{kl}^{\text{LOS}}(t) = \frac{f_{\max} \langle \mathbf{D}_{kl}^{\text{LOS}}(t), \mathbf{v} \rangle}{\|\mathbf{D}_{kl}^{\text{LOS}}(t)\| \|\mathbf{v}\|} \quad (4.15)$$

$$\varphi_{kl}^{\text{LOS}}(t) = \varphi_0 + \frac{2\pi}{\lambda} \|\mathbf{D}_{kl}^{\text{LOS}}(t)\|. \quad (4.16)$$

The generation procedure of the channel impulse response consists of the generation of the initial cluster set, generation of parameters (delays, cluster powers, AoAs, and AoDs) for the initial cluster set, array-time evolution of clusters, and the generation of channel impulse response, as presented in Fig. 4.2. This algorithm is a generalised version of the WINNER channel model [30] by adding an extra block of array-time evolution of clusters to capture massive MIMO channel characteristics. The block of array-time evolution of clusters will be discussed in the next section.

4.2.2 Non-stationary properties

The non-stationary process of the proposed massive MIMO channel model is based on the array-time evolution of clusters which can be characterised by two parts. The first part is the generation of cluster sets $C_l^T(t)$ and $C_k^R(t)$ for each antenna based on BD process on both the time and array axes. This aims at modelling not only the phenomena of cluster appearance and disappearance on antenna arrays of massive MIMO, but also non-stationary behaviors of clusters on the time axis. The generation

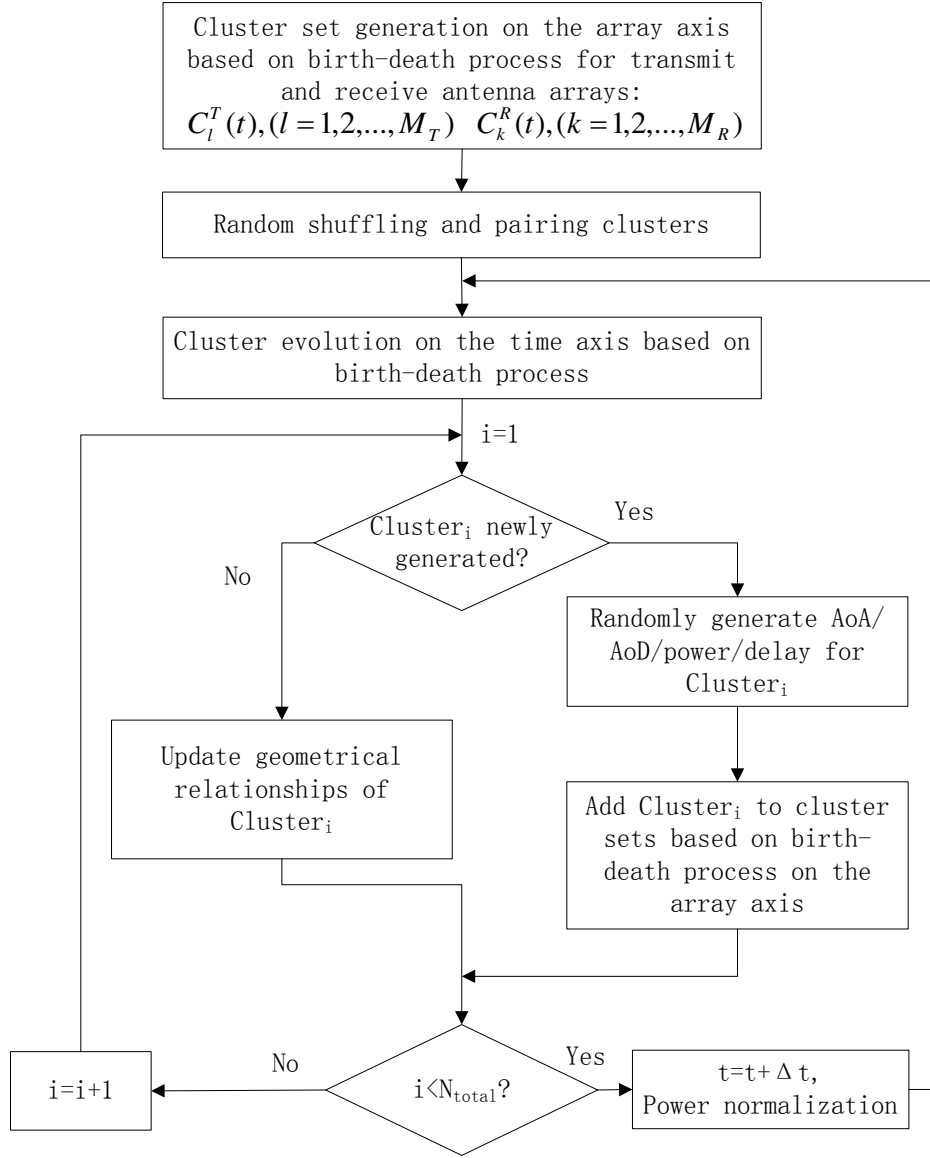


FIGURE 4.3: Algorithm flowchart of array-time evolution of the proposed 3-D twin-cluster model.

procedure is achieved by extending the concept of BD process on the time axis in previous literature [100], [111] to the array axis as well. The outcome of the first part determines the cluster set of each antenna. The second part is the updates of geometrical relationships with respect to the movements of the receiver and clusters. The outcome of the second part determines all parameters for each cluster. The algorithm flowchart describing the array-time cluster evolution is depicted in Fig. 4.3.

Part 1: To describe the algorithm of the array-time cluster evolution, let us first

denote λ_G (per meter) and λ_R (per meter) as the cluster generation rate and recombination rate. Assume the initial number of clusters N and the initial cluster sets of the 1-st transmit and receive antennas $C_1^T = \{c_x^T : x = 1, 2, \dots, N\}$ and $C_1^R = \{c_x^R : x = 1, 2, \dots, N\}$ at the initial time instant t are given, where c_x^T and c_x^R are two representations of Cluster $_x$. Then, these clusters in cluster sets C_1^T and C_1^R evolve according to BD process on the array axis to recursively generate the cluster sets of the rest of antennas at the transmitter and receiver at the initial time instant t , which is expressed as

$$C_{l-1}^T(t) \xrightarrow{\text{E}} C_l^T(t) \quad (l = 2, 3, \dots, M_T) \quad (4.17)$$

$$C_{k-1}^R(t) \xrightarrow{\text{E}} C_k^R(t) \quad (k = 2, 3, \dots, M_R) \quad (4.18)$$

where the operator $\xrightarrow{\text{E}}$ denotes cluster evolution on either the array or time axis. The survival probabilities of the clusters inside the cluster set on array axis at the transmitter P_{survival}^T and the receiver P_{survival}^R can be modeled as exponential functions [115]

$$P_{\text{survival}}^T = e^{-\lambda_R \frac{\delta_T}{D_c^a}} \quad (4.19)$$

$$P_{\text{survival}}^R = e^{-\lambda_R \frac{\delta_R}{D_c^a}} \quad (4.20)$$

where D_c^a is the scenario-dependent correlation factor on the array axis. According to the BD process, the average number of newly generated clusters N_{new}^T and N_{new}^R on the array axis based on the BD process can be computed as [115]

$$\text{E}[N_{\text{new}}^T] = \frac{\lambda_G}{\lambda_R} \left(1 - e^{-\lambda_R \frac{\delta_T}{D_c^a}}\right) \quad (4.21)$$

$$\text{E}[N_{\text{new}}^R] = \frac{\lambda_G}{\lambda_R} \left(1 - e^{-\lambda_R \frac{\delta_R}{D_c^a}}\right) \quad (4.22)$$

where $\text{E}[\cdot]$ designates the expectation. After this process on the array axis, a number of initial clusters may not survive for certain antennas. Meanwhile, new clusters may appear on the array. Each cluster evolves gradually on the antenna array. It can be observed from (4.19) to (4.22) that, if two antenna elements are more separated, the probability that they share the same set of clusters is smaller. To imitate the

TABLE 4.2: Distributions of key geometry parameters for the 3-D twin-cluster model.

Parameters	Distributions	Mean	Standard deviation
ξ_n^T	wrapped Gaussian	0.78rad	0.11rad
θ_n^T	wrapped Gaussian	1.05rad	0.53rad
ξ_n^R	wrapped Gaussian	0.78rad	0.18rad
θ_n^R	wrapped Gaussian	0.78rad	0.91rad
$\mathbf{D}_n^R(t)$	exponential	25m	0.07m
$\mathbf{D}_n^T(t)$	exponential	30m	0.05m
τ_n	exponential	930ns	930ns

complex propagation environment, cluster indices in set $\bigcup_{l=1}^{M_T} C_l^T$ and set $\bigcup_{k=1}^{M_R} C_k^R$ are randomly shuffled and paired to determine to which transmit and receive antennas each cluster is observable. Then, the cluster indices are reassigned from 1 to N_{total} . Moreover, parameters of the initial clusters such as mean AoAs, mean AoDs, delays, and distances are randomly drawn according to distributions listed in Table 4.2. The means and standard deviations for ξ_n^T , θ_n^T , ξ_n^R , θ_n^R , and τ_n in Table 4.2 are generated according to [30]. Also, the power of each cluster is calculated and normalised as in [30].

At the next time instant $t + \Delta t$, the time-axis evolution of clusters is operated as

$$C_l^T(t) \xrightarrow{\text{E}} C_l^T(t + \Delta t) \quad (4.23)$$

$$C_k^R(t) \xrightarrow{\text{E}} C_k^R(t + \Delta t). \quad (4.24)$$

To perform the evolution process of cluster on the time axis as (4.23) and (4.24) show, define the time-dependent channel fluctuation in the time axis at $t + \Delta t$ as $q(t + \Delta t)$. The channel fluctuation measures how much the scattering environment varies within a short period of time. The variation of scattering environment is due to the movements of the receiver and the clusters. Thus, the channel fluctuation is defined by [100]

$$q(t + \Delta t) = q_r(t + \Delta t) + q_c(t + \Delta t) \quad (4.25)$$

where $q_r(t + \Delta t)$ is the channel fluctuation caused by the movement of receiver defined

by $q_r(t + \Delta t) = \|\mathbf{v}\|\Delta t$ and $q_c(t + \Delta t)$ is the channel fluctuation caused by the movement of clusters defined by $q_c(t + \Delta t) = P_F(\|\mathbf{v}_n^T\| + \|\mathbf{v}_n^R\|)\Delta t$ (P_F is the percentage of moving clusters). Given the scenario-dependent space correlation factor D_c^s , each cluster survives with probability P_{survival} on the time axis which can be calculated as [100]

$$P_{\text{survival}}(q(t + \Delta t)) = e^{-\frac{\lambda_R q(t + \Delta t)}{D_c^s}}. \quad (4.26)$$

The mean number of newly generated clusters at time instant $t + \Delta t$ on the time axis $E[N_{\text{new}}(t + \Delta t)]$ is computed according to the BD process [115]

$$E[N_{\text{new}}(t + \Delta t)] = \frac{\lambda_G}{\lambda_R} (1 - e^{-\frac{\lambda_R q(t + \Delta t)}{D_c^s}}). \quad (4.27)$$

After the time evolution process as (4.23)-(4.27) show, all clusters can be categorised as survived clusters or newly generated clusters. The next issue is to decide the set of transmit and receive antennas that are observable to each newly generated cluster. This is determined by the BD process on the array axis, which can be summarised into 4 steps:

Step 1: Randomly generate initial indices \tilde{l} ($1 \leq \tilde{l} \leq M_T$) and \tilde{k} ($1 \leq \tilde{k} \leq M_R$) for the transmit and receive antenna arrays. Then, let the newly generated cluster be observable to the \tilde{l} -th transmit antenna and the \tilde{k} -th receive antenna.

Step 2: Evolve the cluster on the transmit antenna array based on BD process from the $(\tilde{l} - 1)$ -th to the 1-st and from $(\tilde{l} + 1)$ -th to the M_T -th antennas.

Step 3: Evolve the cluster on the receive antenna array based on BD process from the $(\tilde{k} - 1)$ -th to the 1-st and from $(\tilde{k} + 1)$ -th to the M_R -th antennas.

Step 4: Add the cluster to cluster sets whose corresponding antennas can observe the cluster.

Part 2: The remaining issue is the updates of geometry relationships of clusters from t to $t + \Delta t$. The updates of geometry relationships are different for survived clusters and newly generated clusters. Thus, they are described separately.

4.2.2.1 Survived clusters

Regarding survived clusters, their properties such as delays, Doppler frequencies, AoAs and AoDs should be recalculated based on the updates of geometrical relationships from t to $t + \Delta t$. First, the distance vectors are updated due to movements of the receiver and clusters according to

$$\mathbf{D}_n^R(t + \Delta t) = \mathbf{D}_n^R(t) + \mathbf{v}_n^R \Delta t \quad (4.28)$$

$$\mathbf{D}_n^T(t + \Delta t) = \mathbf{D}_n^T(t) + \mathbf{v}_n^T \Delta t \quad (4.29)$$

$$\mathbf{D}_{kn,i_1}^R(t + \Delta t) = \mathbf{D}_{n,i_1}^R(t) - \mathbf{A}_k^R(t) + (\mathbf{v}_n^R - \mathbf{v}) \Delta t \quad (4.30)$$

$$\mathbf{D}_{ln,i_2}^T(t + \Delta t) = \mathbf{D}_{n,i_2}^T(t) + \mathbf{v}_n^T \Delta t - \mathbf{A}_l^T. \quad (4.31)$$

Second, the delay of the n -th cluster at $t + \Delta t$ is expressed as the sum of the updated geometrical delay and the delay of the evolved virtual link,

$$\tau_n(t + \Delta t) = \frac{\|\mathbf{D}_n^T(t + \Delta t)\| + \|\mathbf{D}_n^R(t + \Delta t)\|}{c} + \tilde{\tau}_n(t + \Delta t). \quad (4.32)$$

To describe the evolution of the virtual link, its delay $\tilde{\tau}_n(t + \Delta t)$ is based on a first-order filtering algorithm as $\tilde{\tau}_n(t + \Delta t) = e^{-\frac{\Delta t}{\varsigma}} \tilde{\tau}_n(t) + (1 - e^{-\frac{\Delta t}{\varsigma}})X$ where X is randomly drawn according to the uniform distribution $U(D/c, \tau_{\max})$, ς is a parameter that depends on the coherence of a virtual link and scenarios. Third, the time-variant phase and Doppler frequency are accordingly computed as

$$\varphi_{kl,n,i_1i_2}(t + \Delta t) = \varphi_0 + \frac{2\pi}{\lambda} c \tilde{\tau}_n(t + \Delta t) + \frac{2\pi}{\lambda} [\|\mathbf{D}_{kn,i_1}^R(t + \Delta t)\| + \|\mathbf{D}_{ln,i_2}^T(t + \Delta t)\|] \quad (4.33)$$

$$f_{kn,i_1}(t + \Delta t) = \frac{f_{\max} \langle \mathbf{D}_{kn,i_1}^R(t + \Delta t), \mathbf{v} \rangle}{\|\mathbf{D}_{kn,i_1}^R(t + \Delta t)\| \|\mathbf{v}\|}. \quad (4.34)$$

Last, geometrical relationships of LOS components need to be refreshed as well

$$\mathbf{D}_{kl}^{\text{LOS}}(t + \Delta t) = \mathbf{A}_k^R(t) + \mathbf{v} \Delta t - \mathbf{A}_l^T \quad (4.35)$$

$$f_{kl}^{\text{LOS}}(t + \Delta t) = \frac{f_{\max} \langle \mathbf{D}_{kl}^{\text{LOS}}(t + \Delta t), \mathbf{v} \rangle}{\|\mathbf{D}_{kl}^{\text{LOS}}(t + \Delta t)\| \|\mathbf{v}\|} \quad (4.36)$$

$$\varphi_{kl}^{\text{LOS}}(t + \Delta t) = \varphi_0 + \frac{2\pi}{\lambda} \|\mathbf{D}_{kl}^{\text{LOS}}(t + \Delta t)\|. \quad (4.37)$$

4.2.2.2 Newly generated clusters

On the other hand, for newly generated clusters, their AoAs, AoDs, delays, and distances are initialised according to distributions in Table 4.2. The power of each cluster is calculated and normalised as in [30]. Denote the set of all survived clusters as C_{Survived} and the set of all newly generated clusters as C_{New} after the time-axis evolution. The average total power of survived and newly generated clusters should be normalised as

$$\sum_{\text{Cluster}_i \in C_{\text{Survived}}} P_i + \sum_{\text{Cluster}_j \in C_{\text{New}}} P_j = 1. \quad (4.38)$$

Thus far, the array-time evolution of clusters from t to $t + \Delta t$ is finished. This evolution process can be operated recursively with respect to time.

4.3 Statistical Properties of the Theoretical Massive MIMO Channel Model

4.3.1 STCF

The STCF between the channel gains $h_{kl,n}(t)$ and $h_{k'l',n}(t)$ is defined as [34]

$$\rho_{kl,k'l',n}(\delta_T, \delta_R, \Delta t; t) = \text{E} \left[\frac{h_{kl,n}^*(t) h_{k'l',n}(t + \Delta t)}{|h_{kl,n}^*(t)| |h_{k'l',n}(t + \Delta t)|} \right]. \quad (4.39)$$

As the LOS component and NLOS components are independent, (4.39) can be rewritten as the sum of the STCFs of the LOS component and the NLOS components

$$\rho_{kl,k'l',n}(\delta_T, \delta_R, \Delta t; t) = \rho_{kl,k'l',n}^{\text{LOS}}(\delta_T, \delta_R, \Delta t; t) + \rho_{kl,k'l',n}^{\text{NLOS}}(\delta_T, \delta_R, \Delta t; t) \quad (4.40)$$

where

$$\rho_{kl,k'l',n}^{\text{LOS}}(\delta_T, \delta_R, \Delta t; t) = \frac{K\delta(n-1)}{K+1} e^{j[2\pi f_{k'l'}^{\text{LOS}}(t+\Delta t)(t+\Delta t) - 2\pi f_{kl}^{\text{LOS}}(t)t + \varphi_{k'l'}^{\text{LOS}}(t+\Delta t) - \varphi_{kl}^{\text{LOS}}(t)]} \quad (4.41)$$

$$\rho_{kl,k'l',n}^{\text{NLOS}}(\delta_T, \delta_R, \Delta t; t) = \frac{1}{K\delta(n-1)+1} \mathbb{E} \left[\lim_{S_1, S_2 \rightarrow \infty} \frac{1}{\sqrt{S_1 S_2}} \sum_{i_1=1}^{S_1} \sum_{i_2=1}^{S_2} e^{j\Phi_0} \right] \quad (4.42)$$

with

$$\Phi_0 = 2\pi f_{k'n,i_1}(t+\Delta t)(t+\Delta t) - 2\pi f_{kn,i_1}(t)t + \varphi_{k'l',n,i_1 i_2}(t+\Delta t) - \varphi_{kl,n,i_1 i_2}(t). \quad (4.43)$$

4.3.2 Space CCF

By setting $\Delta t = 0$, the STCF reduces to the space Cross-Correlation Function (CCF)

$$\rho_{kl,k'l',n}(\delta_T, \delta_R; t).$$

$$\rho_{kl,k'l',n}(\delta_T, \delta_R; t) = \mathbb{E} \left[\frac{h_{kl,n}^*(t) h_{k'l',n}(t)}{|h_{kl,n}^*(t)| |h_{k'l',n}(t)|} \right] = \rho_{kl,k'l',n}^{\text{LOS}}(\delta_T, \delta_R; t) + \rho_{kl,k'l',n}^{\text{NLOS}}(\delta_T, \delta_R; t) \quad (4.44)$$

where

$$\rho_{kl,k'l',n}^{\text{LOS}}(\delta_T, \delta_R; t) = \frac{K\delta(n-1)}{K+1} e^{j[2\pi f_{k'l'}^{\text{LOS}}(t)t - 2\pi f_{kl}^{\text{LOS}}(t)t + \varphi_{k'l'}^{\text{LOS}}(t) - \varphi_{kl}^{\text{LOS}}(t)]}. \quad (4.45)$$

Regarding the correlation of the NLOS components, as a cluster has a probability of $e^{-\lambda_R \frac{|l-l'|\delta_T + |k-k'|\delta_R}{D_c^a}}$ to survive when evolving from $h_{kl,n}(t)$ to $h_{k'l',n}(t)$, the space CCF of the NLOS components is scaled by $e^{-\lambda_R \frac{|l-l'|\delta_T + |k-k'|\delta_R}{D_c^a}}$,

$$\rho_{kl,k'l',n}^{\text{NLOS}}(\delta_T, \delta_R; t) = \frac{1}{K\delta(n-1)+1} e^{-\lambda_R \frac{|l-l'|\delta_T + |k-k'|\delta_R}{D_c^a}} \times$$

$$\int_{-\pi}^{\pi} \int_{-\pi}^{\pi} \int_{-\frac{\pi}{2}}^{\frac{\pi}{2}} \int_{-\frac{\pi}{2}}^{\frac{\pi}{2}} e^{j\Phi_1} p_R(\xi_n^R, \theta_n^R) p_T(\xi_n^T, \theta_n^T) d\xi_n^R d\xi_n^T d\theta_n^R d\theta_n^T \quad (4.46)$$

with

$$\Phi_1 = 2\pi f_{k'n}(t)t - 2\pi f_{kn}(t)t + \varphi_{k'l',n}(t) - \varphi_{kl,n}(t). \quad (4.47)$$

As the space CCF $\rho_{kl,k'l',n}(\delta_T, \delta_R; t)$ depends on the values of k, k', l, l' , and can not be reduced to solely be with respect to $|k - k'|$ and $|l - l'|$, the Wide Sense Stationary (WSS) assumption on the array axis for massive MIMO is not valid.

4.3.3 Time ACF

On the other hand, by setting $l = l', k = k'$, the time Autocorrelation Function (ACF) $\rho_{kl,n}(\Delta t; t)$ is obtained.

$$\rho_{kl,n}(\Delta t; t) = \mathbb{E} \left[\frac{h_{kl,n}^*(t) h_{kl,n}(t + \Delta t)}{|h_{kl,n}^*(t)| |h_{kl,n}(t + \Delta t)|} \right] = \rho_{kl,n}^{\text{LOS}}(\Delta t; t) + \rho_{kl,n}^{\text{NLOS}}(\Delta t; t). \quad (4.48)$$

Since the LOS component is uncorrelated to NLOS components, their time ACFs, $\rho_{kl,n}^{\text{LOS}}(\Delta t; t)$ and $\rho_{kl,n}^{\text{NLOS}}(\Delta t; t)$, are calculated separately as

$$\rho_{kl,n}^{\text{LOS}}(\Delta t; t) = \frac{K\delta(n-1)}{K+1} e^{j[2\pi f_{kl}^{\text{LOS}}(t+\Delta t)(t+\Delta t) - 2\pi f_{kl}^{\text{LOS}}(t)t + \varphi_{kl}^{\text{LOS}}(t+\Delta t) - \varphi_{kl}^{\text{LOS}}(t)]}. \quad (4.49)$$

Regarding the correlation of the NLOS components, the survival probability of a cluster is $e^{-\lambda_R \frac{\|\mathbf{v}\| \Delta t + P_F(\|\mathbf{v}_n^T\| + \|\mathbf{v}_n^R\|) \Delta t}{D_c^2}}$ when evolving from $h_{kl,n}(t)$ to $h_{kl,n}(t + \Delta t)$, the time ACF of the NLOS components is scaled by $e^{-\lambda_R \frac{\|\mathbf{v}\| \Delta t + P_F(\|\mathbf{v}_n^T\| + \|\mathbf{v}_n^R\|) \Delta t}{D_c^2}}$,

$$\begin{aligned} \rho_{kl,n}^{\text{NLOS}}(\Delta t; t) &= \frac{1}{K\delta(n-1) + 1} e^{-\lambda_R \frac{\|\mathbf{v}\| \Delta t + P_F(\|\mathbf{v}_n^T\| + \|\mathbf{v}_n^R\|) \Delta t}{D_c^2}} \times \\ &\int_{-\pi}^{\pi} \int_{-\pi}^{\pi} \int_{-\frac{\pi}{2}}^{\frac{\pi}{2}} \int_{-\frac{\pi}{2}}^{\frac{\pi}{2}} e^{j\Phi_2} p_R(\xi_n^R, \theta_n^R) p_T(\xi_n^T, \theta_n^T) d\xi_n^R d\xi_n^T d\theta_n^R d\theta_n^T \end{aligned} \quad (4.50)$$

with

$$\Phi_2 = 2\pi f_{kn}(t + \Delta t)(t + \Delta t) - 2\pi f_{kn}(t)t + \varphi_{kl,n}(t + \Delta t) - \varphi_{kl,n}(t). \quad (4.51)$$

As the time ACF $\rho_{kl,n}(\Delta t; t)$ depends on the values of t , and can not be reduced to solely be with respect to Δt , the WSS assumption on the time axis for the proposed massive MIMO channel model is not valid.

4.3.4 Doppler PSD

The Doppler PSD $S_n(f; t)$ with respect to the Doppler frequency f is the Fourier transform of the time ACF, which can be presented as

$$S_n(f; t) := \int_{-\infty}^{\infty} \rho_{kl,n}(\Delta t; t) e^{-j2\pi f \Delta t} d(\Delta t). \quad (4.52)$$

It should be also noticed that the Doppler PSD is time dependent.

4.3.5 Doppler frequency standard deviation on the antenna array

As spherical wavefronts are assumed in the proposed channel model, different antennas on the same array will experience different Doppler shifts. Namely, Doppler frequencies may vary on the antenna array. To study the variations of Doppler frequency of the receiver on the array axis, the average Doppler frequency on the k -th receive antenna, \bar{f}_{kn} , is calculated as

$$\bar{f}_{kn} = \int_{-\pi - \frac{\pi}{2}}^{\pi} \int_{-\frac{\pi}{2}}^{\frac{\pi}{2}} f_{kn}(\xi_n^R, \theta_n^R) p(\xi_n^R, \theta_n^R) d\xi_n^R d\theta_n^R. \quad (4.53)$$

Next, the average Doppler frequency on the array axis $\mu_{\bar{f}_n}$ is presented as $\mu_{\bar{f}_n} = \mathbb{E}[\bar{f}_{kn}] = \frac{\sum_{k=1}^{M_R} \bar{f}_{kn}}{M_R}$. Finally, the standard deviation of Doppler frequency $\sigma_{\bar{f}_n}$ on the

array axis can be obtained as

$$\sigma_{\bar{f}_n} = \sqrt{\frac{\sum_{k=1}^{M_R} (\bar{f}_{kn} - \mu_{\bar{f}_n})^2}{M_R}}. \quad (4.54)$$

For conventional MIMO channel models, the Doppler frequency on the whole antenna array is assumed to be the same which is equivalent to $\sigma_{\bar{f}_n} = 0$. Conversely, for massive MIMO channel models, $\sigma_{\bar{f}_n}$ may not be 0 and a larger $\sigma_{\bar{f}_n}$ means that the Doppler frequency varies more significantly on the antenna array.

4.3.6 Condition number

Condition number is used to measure the correlation of the channel matrix [22]. A larger condition number implies higher correlation. The condition number is defined by the quotient of maximum eigenvalue and the minimum eigenvalue of the channel matrix

$$\gamma(\text{dB}) = 20 \log_{10} \frac{\lambda_{\max}(\mathbf{H})}{\lambda_{\min}(\mathbf{H})} \quad (4.55)$$

where the operators $\lambda_{\max}(\cdot)$ and $\lambda_{\min}(\cdot)$ represent the maximum eigenvalue and the minimum eigenvalue, respectively.

4.4 A Non-Stationary 3-D Wideband Twin-Cluster Simulation Model for Massive MIMO Channels

Previously, in the proposed channel theoretical model, the number of scatterers is assumed to be infinity ($S_1, S_2 \rightarrow \infty$) which is capable of providing accurate analytic channel characteristic results. However, with respect to a channel simulator, infinite scatterers are not practical as the complexity of implementation is enormous. Therefore, a compromise between accuracy and complexity should be addressed. The

target of this section is to develop a channel simulator with a finite and proper scatterer number while capturing channel characteristics as accurate as possible. The corresponding simulation model of the proposed massive MIMO channel model is obtained by reducing (4.3) as

$$h_{kl,n}(t) = \delta(n-1) \sqrt{\frac{K}{K+1}} e^{j(2\pi f_{kl}^{\text{LOS}} t + \varphi_{kl}^{\text{LOS}})} + \sqrt{\frac{P_n}{K+1}} \sum_{i_1=1}^{S_1} \sum_{i_2=1}^{S_2} \frac{e^{j(2\pi f_{kn,i_1} t + \varphi_{kl,n,i_1 i_2})}}{\sqrt{S_1 S_2}}. \quad (4.56)$$

Let \mathbf{x} be the vector of AoAs and AoDs defined by $\mathbf{x} = (\theta^R, \xi^R, \theta^T, \xi^T)$. In the theoretical model, define $g(\mathbf{x}) = \frac{h_{kl,n}^*(t) h_{k'l',n}(t+\Delta t)}{|h_{kl,n}^*(t)| |h_{k'l',n}(t+\Delta t)|}$ with \mathbf{x} distributed according to the Cumulative Distribution Function (CDF) $F(\mathbf{x})$ of AoAs and AoDs. The STCF $\rho_{kl,k'l',n}(\delta_T, \delta_R, \Delta t; t)$ for the theoretical model in (4.39) is calculated as the expectation of $g(\mathbf{x})$,

$$\rho_{kl,k'l',n}(\delta_T, \delta_R, \Delta t; t) = \mathbb{E}[g(\mathbf{x})] = \int g(\mathbf{x}) dF(\mathbf{x}). \quad (4.57)$$

On the other hand, a simulation model aims at approximating $\rho_{kl,k'l',n}(\delta_T, \delta_R, \Delta t; t)$ with $S_1 S_2$ discrete vectors $\{\mathbf{x}_i\}_{i=1}^{S_1 S_2}$, where each \mathbf{x}_i follows the CDF $F(\mathbf{x})$ and $\mathbf{x}_i = (\theta_i^R, \xi_i^R, \theta_i^T, \xi_i^T)$. Then, the approximated value $\hat{\rho}_{kl,k'l',n}(\delta_T, \delta_R, \Delta t; t)$ can be expressed as

$$\hat{\rho}_{kl,k'l',n}(\delta_T, \delta_R, \Delta t; t) = \mathbb{E}[g(\mathbf{x})] = \frac{1}{S_1 S_2} \sum_{i=1}^{S_1 S_2} g(\mathbf{x}_i). \quad (4.58)$$

The remaining issue is to determine the vector sequence $\{\mathbf{x}_i\}_{i=1}^{S_1 S_2}$ with reasonable computational complexity to approximate $\rho_{kl,k'l',n}(\delta_T, \delta_R, \Delta t; t)$ with $\hat{\rho}_{kl,k'l',n}(\delta_T, \delta_R, \Delta t; t)$. A number of algorithms to calculate $\{\mathbf{x}_i\}_{i=1}^{S_1 S_2}$ such as the Method of Equal Distances (MED), Method of Equal Area (MEA), Method of Exact Doppler Spread (MEDS), and the Monte Carlo Method (MCM) have been introduced in [34]. Here, the MEA is applied to calculating the discrete vectors $\{\mathbf{x}_i\}_{i=1}^{S_1 S_2}$ of the simulation model according to $\int_{\mathbf{x}_{i-1}}^{\mathbf{x}_i} dF(\mathbf{a}) = \frac{1}{S_1 S_2}$ [34]. Since \mathbf{x} is four dimensional in this model, the ‘area’ in MEA in this case is generalised as the probability measure of a set. As a result, $F(\mathbf{x})$ is divided into $S_1 S_2$ sets with the same probability of $\frac{1}{S_1 S_2}$, then \mathbf{x}_i can be computed

as $\mathbf{x}_i = F^{-1}\left(\frac{i}{S_1 S_2}\right)$ where $F^{-1}(\cdot)$ is the inverse function of $F(\cdot)$.

4.5 Numerical Results and Analysis

The distributions of azimuth and elevation angles at the transmitter side and the receiver side are assumed to obey the two dimensional von Mises distribution [118], where azimuth angles and elevation angles are assumed to be mutually independent. Therefore, the Probability Density function (PDF) of angles of the n -th cluster $p_Z(\xi_n^Z, \theta_n^Z)$ with $Z = \{T, R\}$ can be expressed as

$$p_Z(\xi_n^Z, \theta_n^Z) = \frac{\exp[\kappa(\cos(\xi_n^Z - \bar{\xi}_n^Z) + \cos(\theta_n^Z - \bar{\theta}_n^Z))]}{[2\pi I_0(\kappa)]^2} \quad (4.59)$$

where $\bar{\xi}_n^Z$ and $\bar{\theta}_n^Z$ are the mean elevation and azimuth AoD/AoA, and $I_0(\cdot)$ is the zero-th order modified Bessel function. Moreover, $\kappa \geq 0$ controls the width of the distribution functions.

By setting Δt to 0, the absolute values of the space CCF $|\rho_{11,22,1}(\delta_T, \delta_R; t)|$ of the three dimensional twin cluster model are illustrated in Fig. 4.4. A decreasing trend can be observed as the normalised antenna spacings increase at both the transmitter and receiver sides. The absolute values of space CCF drop smoothly when antenna spacing at the transmitter side enlarges. Meanwhile, fluctuations can be seen as antenna spacing at the receiver side increases. These fluctuations are caused by non-stationary properties due to the movements of the receiver.

Next, by setting δ_T and Δt to 0, the impact of cluster elevation angles at the receiver side on the absolute space CCF $|\rho_{11,12,1}(0, \delta_R; t)|$ of the receiver is depicted in Fig. 4.5. The increase in cluster elevation angles at the receiver side results in high receive antenna correlations, because the projected distance of two antenna element in the 3-D space is proportional to the product of the cosine of the azimuth angle and the cosine of the elevation angle. When the elevation angle increases from 0 to $\pi/2$, its cosine value decreases. Besides, the space CCF of the simulation model is compared with the theoretical model, showing that the simulation model is able to capture the

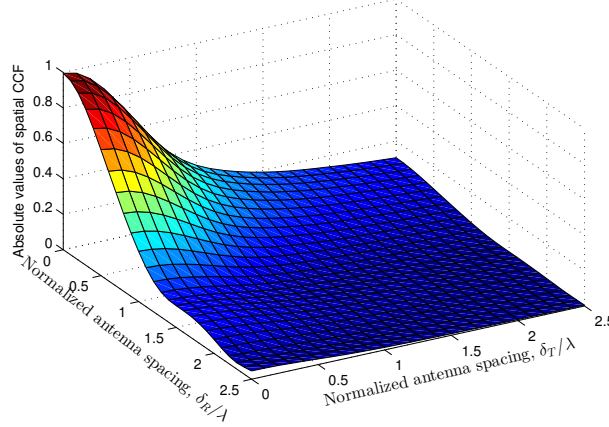


FIGURE 4.4: Absolute values of the space CCF $|\rho_{11,22,1}(\delta_T, \delta_R; t)|$ of the 3-D twin-cluster model. ($M_R = M_T = 32$, $D = 200\text{m}$, $D_c^a = 30\text{m}$, $D_c^s = 50\text{m}$, $v_A^T = \pi/3$, $v_E^T = \pi/6$, $v_A^R = \pi/4$, $v_E^R = \pi/4$, $\bar{\theta}_1^T = -1.03$, $\bar{\xi}_1^T = 1.19$, $\bar{\theta}_1^R = 1.65$, $\bar{\xi}_1^R = 0.16$, $t = 4\text{s}$, $\lambda = 0.15\text{m}$, $f_{\max} = 33.33\text{Hz}$, $\alpha_v = \pi/6$, $\kappa = 5$, NLOS).

channel spatial correlation characteristic at the cost of slightly less accuracy. It should be noticed that the gap between the theoretical model and the simulation model is caused by the MEA mentioned in Section 4.4. There are a infinite number of solutions of discrete vectors $\{\mathbf{x}_i\}_{i=1}^{S_1 S_2}$ of the simulation model such that $\mathbf{x}_i = F^{-1} \left(\frac{i}{S_1 S_2} \right)$. The MEA is applied to the calculations of elevation AoDs, azimuth AoDs, elevation AoAs, and azimuth AoAs independently. However, no optimization is implied in the MEA. Therefore, more complicated searching algorithms for $\{\mathbf{x}_i\}_{i=1}^{S_1 S_2}$ can be used to reduce the gap between the theoretical model and the simulation, but with much higher computational complexity.

The absolute values of the time ACF in terms of cluster elevation angles at the receiver side are analysed in Fig. 4.6. The figure shows that the time ACF decreases slower as the elevation angles become larger. The philosophy is that the Doppler frequency equals the product of f_{\max} , cosine of the azimuth angle, and cosine of the elevation angle. For fixed f_{\max} and azimuth angle, the absolute Doppler frequency is decreasing as the elevation angle increases from 0 to $\pi/2$. Consequently, when the elevation angle reaches $\pi/2$, the absolute Doppler frequency is minimum which results in the slowest decrease of the time ACF. Meanwhile, the normalised Fourier transform of the time ACF, i.e., the PDF of Doppler frequency of the proposed model is illustrated in Fig. 4.7. The PDF of Doppler frequency of the conventional MIMO

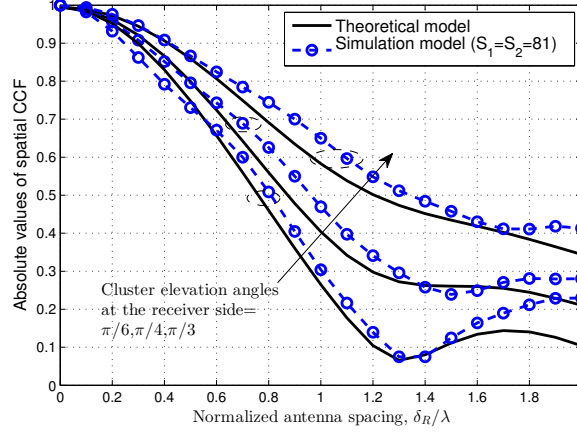


FIGURE 4.5: Absolute values of the receiver space CCF $|\rho_{11,12,1}(0, \delta_R; t)|$ in terms of cluster elevation angles at the receiver side. ($M_R = 32$, $D = 200\text{m}$, $D_c^a = 30\text{m}$, $D_c^s = 50\text{m}$, $\varsigma = 1\text{s}$, $v_A^T = \pi/3$, $v_E^T = \pi/6$, $v_A^R = \pi/4$, $v_E^R = \pi/4$, $\bar{\theta}_1^T = -1.03$, $\bar{\xi}_1^T = 1.19$, $\bar{\theta}_1^R = 1.65$, $t = 4\text{s}$, $\lambda = 0.15\text{m}$, $f_{\max} = 33.33\text{Hz}$, $\alpha_v = \pi/6$, $\kappa = 5$, NLOS).

channel model is symmetrical with respect to 0. However, this may not be necessary for the proposed non-stationary massive MIMO channel model. There are two observations that should be noticed in Fig. 4.7. First, the PDFs of Doppler frequency at different time instants vary because of the non-stationary properties on the time axis. Namely, the WSS condition on the time domain is not available as a consequence of time-variant properties and the inclusion of BD process on the time axis. The factor $e^{-\lambda_R \frac{\|\mathbf{v}\|\Delta t + P_F(\|\mathbf{v}_n^T\| + \|\mathbf{v}_n^R\|)\Delta t}{D_c^s}}$ of the time ACF in (4.50) with respect to Δt is equivalent to a translation in the Fourier transform domain. Moreover, simulation models align well with theoretical models as shown in Fig. 4.6 and Fig. 4.7.

In addition, Fig. 4.8 shows the standard deviation of Doppler frequencies on the antenna array. Conventional MIMO channel models assume farfield condition which results in a constant Doppler frequency on the entire antenna array. Conversely, the nearfield condition is assumed in the proposed massive MIMO channel model. As a result, the Doppler frequencies for different antennas are different. Since the nearfield effect is more significant as the number of antennas grows, the standard deviation increases accordingly.

Furthermore, a comparison of condition numbers between the 2-D and 3-D models is shown in Fig. 4.9. Stronger correlations are observed in the 2-D model than the 3-D

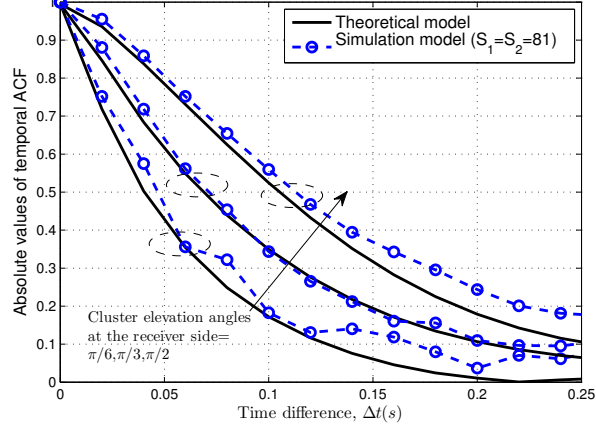


FIGURE 4.6: Absolute values of the time ACF $|\rho_{11,1}(\Delta t; t)|$ in terms of cluster elevation angle at the receiver side ($M_R = 32$, $D = 200\text{m}$, $D_c^a = 30\text{m}$, $D_c^s = 50\text{m}$, $\varsigma = 1\text{s}$, $v_A^T = \pi/3$, $v_E^T = \pi/6$, $v_A^R = \pi/4$, $v_E^R = \pi/4$, $\bar{\theta}_1^T = -1.03$, $\bar{\xi}_1^T = 1.19$, $\bar{\theta}_1^R = 1.65$, $t = 4\text{s}$, $\lambda = 0.15\text{m}$, $\|\mathbf{v}_n^T\| = \|\mathbf{v}_n^R\| = 0.25\text{m/s}$, $P_F = 0.3$, $f_{\max} = 33.33\text{Hz}$, $\alpha_v = \pi/6$, $\kappa = 5$, NLOS).

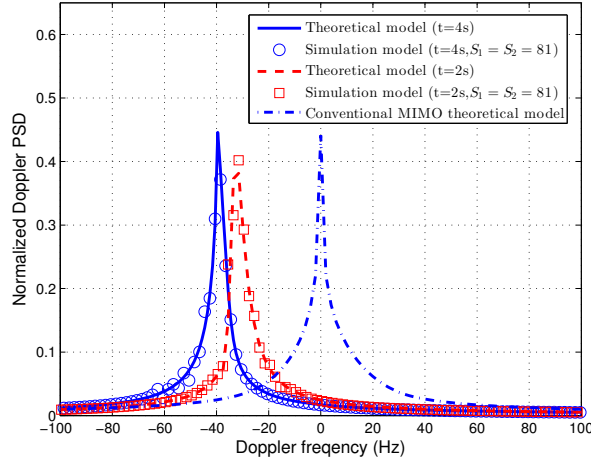


FIGURE 4.7: The normalised Doppler PSD at different time instants ($M_R = 32$, $D = 200\text{m}$, $D_c^a = 30\text{m}$, $D_c^s = 50\text{m}$, $\varsigma = 1\text{s}$, $v_A^T = \pi/3$, $v_E^T = \pi/6$, $v_A^R = \pi/4$, $v_E^R = \pi/4$, $\bar{\theta}_1^T = -1.03$, $\bar{\xi}_1^T = 1.19$, $\bar{\theta}_1^R = 1.65$, $\lambda = 0.15\text{m}$, $\lambda_G = 80\text{m}$, $\lambda_R = 4\text{m}$, $\|\mathbf{v}_n^T\| = \|\mathbf{v}_n^R\| = 0.25\text{m/s}$, $P_F = 0.3$, $f_{\max} = 33.33\text{Hz}$, $\alpha_v = \pi/6$, $\kappa = 5$, NLOS).

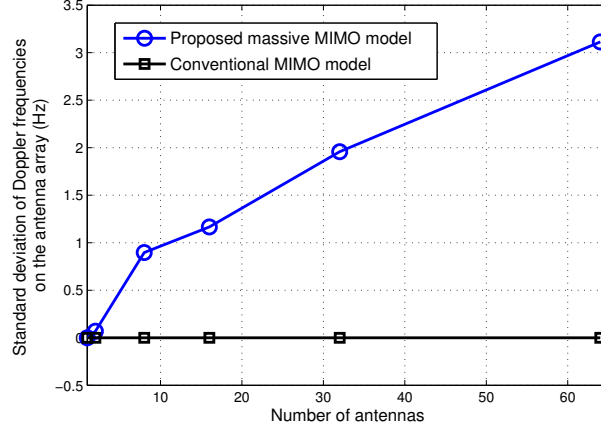


FIGURE 4.8: Standard deviation of the Doppler frequencies on the antenna array ($D = 200\text{m}$, $D_c^a = 30\text{m}$, $D_c^s = 50\text{m}$, $\varsigma = 1\text{s}$, $v_A^T = \pi/3$, $v_E^T = \pi/6$, $v_A^R = \pi/4$, $v_E^R = \pi/4$, $\bar{\theta}_1^T = -1.03$, $\bar{\xi}_1^T = 1.19$, $\bar{\theta}_1^R = 1.65$, $\bar{\xi}_1^R = 0.16$, $\lambda = 0.15\text{m}$, $\|\mathbf{v}_n^T\| = \|\mathbf{v}_n^R\| = 0.25\text{m/s}$, $P_F = 0.3$, $f_{\max} = 33.33\text{Hz}$, $\alpha_v = \pi/6$, $\kappa = 5$, NLOS).

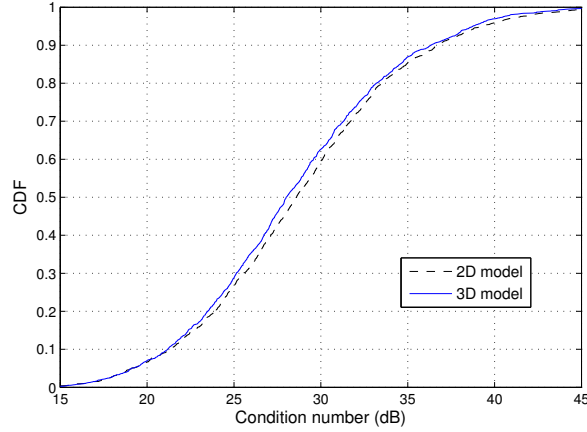


FIGURE 4.9: Comparisons of CDFs of condition numbers between the 2-D and 3-D model ($M_T = 4$, $M_R = 32$, $D = 200\text{m}$, $D_c^a = 30\text{m}$, $D_c^s = 50\text{m}$, $\varsigma = 1\text{s}$, $v_A^T = \pi/3$, $v_E^T = \pi/6$, $v_A^R = \pi/4$, $v_E^R = \pi/4$, $\bar{\theta}_1^T = -1.03$, $\bar{\xi}_1^T = 1.19$, $\bar{\theta}_1^R = 1.65$, $t = 4\text{s}$, $\lambda = 0.15\text{m}$, $\lambda_G = 80\text{m}$, $\lambda_R = 4\text{m}$, $\|\mathbf{v}_n^T\| = \|\mathbf{v}_n^R\| = 0.25\text{m/s}$, $P_F = 0.3$, $f_{\max} = 33.33\text{Hz}$, $\alpha_v = \pi/6$, $\kappa = 5$, NLOS).

model due to the fact that clusters have higher probabilities to be correlated in a 2-D space than a 3-D space. However, this difference is relatively less significant because the random distribution of cluster locations partially averages out the impact.

Fig. 4.10 illustrates the non-stationary properties on the array axis in the form of the receiver Angular Power Spectrum (APS). It should be noticed that the estimated angle here means the angle between the cluster and the receive antenna array. Here, the Multiple Signal Classification (MUSIC) algorithm [120] is applied to AoA estimation.

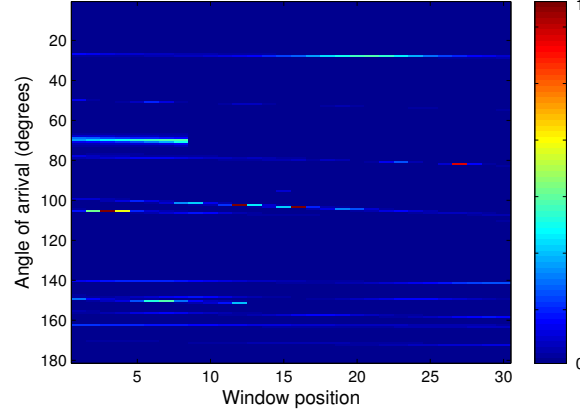


FIGURE 4.10: A snap shot of the angular power spectrum of the receiver antenna array ($M_T = 1$, $M_R = 32$, $D = 200\text{m}$, $D_c^a = 30\text{m}$, $D_c^s = 50\text{m}$, $\varsigma = 1\text{s}$, $v_A^T = \pi/3$, $v_E^T = \pi/6$, $v_A^R = \pi/4$, $v_E^R = \pi/4$, $\bar{\theta}_1^T = -1.03$, $\bar{\xi}_1^T = 1.19$, $\bar{\theta}_1^R = 1.65$, $t = 4\text{s}$, $\lambda = 0.15\text{m}$, $\lambda_G = 80/\text{m}$, $\lambda_R = 4/\text{m}$, $f_{\max} = 0\text{Hz}$, NLOS).

A sliding window formed by 3 consecutive receive antennas is shifted by 1 antenna at a time from the first to the last antenna. Consequently, for a 32-element antenna array, there are in total 30 window positions as Fig. 4.10 shows. Clusters appear and disappear on the array axis, which results in that different antennas may observe different sets of clusters. Additionally, angles of a number of clusters shift on the array axis due to the nearfield effect. Finally, receive power variations can be observed on the antenna array. Similar conclusions on these mentioned features of the proposed model were also observed in measurements in massive MIMO channels in [1].

Regarding cluster evolution on the time axis, an example of cluster sets in different time instants is shown in Fig. 4.11. Clusters evolve according to the BD process. Thus, it can be seen that there are clusters disappearing and new clusters appearing. In this case, the transmit and receive antenna arrays observe a time-variant set of clusters.

It is important to note that in the numerical analysis, parameters such as mean and standard deviation of azimuth AoAs/AoDs of the transmitter and receiver, mean and standard deviation of delays, maximum delay, spatial correlation distance, and cluster powers were generated according to the WINNER II channel model in [30]. The generation and recombination rates of clusters and percentage of moving clusters were adapted from [100] and [111]. However, certain parameters such as cluster distances

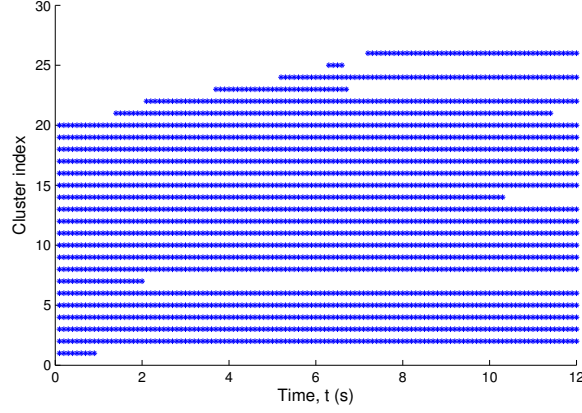


FIGURE 4.11: Cluster evolution on the time axis ($D_c^s = 50\text{m}$, $\varsigma = 1\text{s}$, $\lambda = 0.15\text{m}$, $\lambda_G = 80\text{m}$, $\lambda_R = 4\text{m}$, $\|\mathbf{v}_n^T\| = \|\mathbf{v}_n^R\| = 0.25\text{m/s}$, $P_F = 0.3$, $f_{\max} = 33.33\text{Hz}$, NLOS).

to the transmitter or receiver were given based on reasonable assumptions, since we have not found any relevant measurement data so far. These parameters of the model can be further validated by measurements whenever available in the future.

4.6 Summary

Key characteristics of massive MIMO channels have not been captured by conventional MIMO channel models. In this chapter, we have proposed a novel theoretical non-stationary 3-D wideband twin-cluster channel model along with the corresponding simulation model for massive MIMO systems with carrier frequencies in the order of GHz. Spherical wavefronts have been assumed to characterise nearfield effects resulting in AoA shifts, received power variations, and Doppler frequency variations on the antenna array. The impact of elevation angles of clusters on the correlation properties of the massive MIMO channel model has been studied. Most importantly, non-stationary properties on both the time and array axes have been modeled by BD processes. The proposed massive MIMO channel model is able to describe not only the appearance and disappearance of clusters on the time axis, but also the cluster evolution on the array axis, which is normally not included in conventional MIMO channels. Moreover, it has been shown that the channel characteristics of the simulation model are consistent with those of the theoretical model. In addition, important

channel features of massive MIMO channels are characterised by the proposed models, which may serve as a design framework to model massive MIMO channels. Finally, certain parameters of the proposed channel model need to be further validated by relevant channel measurements, which will be our future work when such channel measurements become available in the literature.

Chapter 5

A Novel KBSM for 5G Massive MIMO Channels

5.1 Introduction

It is of crucial importance to develop efficient small-scale fading channel models which are able to capture massive Multiple-Input Multiple-Output (MIMO) channel characteristics in order to design and evaluate Fifth Generation (5G) massive MIMO systems. Chapter 3 and Chapter 4 proposed Two-Dimensional (2-D) and Three-Dimensional (3-D) non-stationary Geometry-Based Stochastic Models (GBSMs) for 5G massive MIMO channels. However, these channel models are too complicated to provide performance analysis of massive MIMO systems. Instead, CBSMs were more convenient to analyse channel capacities of massive MIMO systems. The classic Independent and Identically Distributed (i.i.d.) Rayleigh fading channels were used in [121] to analyse massive MIMO system performance. However, the i.i.d. assumption may over-simplify the channel model. Conventional Correlation-Based Stochastic Models (CBSMs) are usually utilised to study the performance of MIMO systems with spatial correlation due to their low complexity. The Kronecker-Based Stochastic Model (KBSM) assumes that the correlation matrices of the transmitter and receiver are unrelated [13], [122]. Channel capacities of massive MIMO systems with KBSM were

presented in [13] and [123]. Also, a KBSM with Line-of-Sight (LOS) components was assumed in [73] for capacity analysis of massive MIMO. On the other hand, joint correlation at both the transmitter and receiver was included in the Weichselberger MIMO model [124]. Sum rates of massive MIMO systems with the Weichselberger MIMO model were investigated in [107].

However, it was pointed out in [1] and [87] that all the antennas elements may not observe the same set of scatterers in massive MIMO systems. This property was not included in the abovementioned conventional MIMO CBSMs. A novel CBSM considering massive MIMO channel characteristics should be developed.

The **contributions** of this chapter are listed as below:

1. A novel KBSM with Birth-Death (BD) process on the array axis (KBSM-BD-AA) is proposed for 5G massive MIMO channels. The BD process is abstracted by a survival probability matrix whose rows are values from exponential functions. The survival probability matrix reduces channel correlations.
2. Upper and lower bounds of channel capacities of the proposed KBSM-BD-AA in both the high and low Signal-to-Noise Ratio (SNR) regimes are investigated.

The remainder of this chapter is organised as follows. Section 5.2 describes the system model as well as the proposed KBSM-BD-AA. Channel capacity analysis of the proposed KBSM-BD-AA is derived in Section 5.3. Results and discussions are presented in Section 5.4. Conclusions are drawn in Section 5.5.

5.2 System Model

Let us consider an $M_R \times M_T$ MIMO system. The receiver and transmitter are equipped with M_R and M_T Uniform Linear Arrays (ULAs), respectively. To study the performance of massive MIMO systems, the numbers of receive and transmit antennas are assumed to be unboundedly increasing with a constant ratio, i.e., $M_R, M_T \rightarrow \infty$

and $\gamma = \frac{M_R}{M_T}$. This assumption was widely used in [37], [107], [123], [125]. The MIMO channel can be characterised by an $M_R \times M_T$ complex matrix \mathbf{H} . Then, let \mathbf{s} be the transmitted symbol vector, the received vector \mathbf{y} can be expressed as

$$\mathbf{y} = \mathbf{H}\mathbf{s} + \mathbf{n} \quad (5.1)$$

where \mathbf{n} is the zero-mean unit-variance Additive White Gaussian Noise (AWGN) vector. In addition, we assume that the mean power of the received signal via such an MIMO channel is normalised as $\text{E} [\text{trace}(\mathbf{H}\mathbf{H}^H)] = M_R M_T$, where $\text{E}[\cdot]$ calculates the expected value and $\text{trace}(\cdot)$ calculates the trace of a matrix.

5.2.1 Conventional KBSM

The conventional KBSM assumes that spatial correlation matrices of the receive arrays and transmit arrays are unrelated. Hence, the channel matrix can be expressed as

$$\mathbf{H} = \mathbf{R}_R^{\frac{1}{2}} \mathbf{H}_w \mathbf{R}_T^{\frac{T}{2}} \quad (5.2)$$

where \mathbf{H}_w is an $M_R \times M_T$ matrix with zero-mean unit-variance complex i.i.d. Gaussian entries, \mathbf{R}_R and \mathbf{R}_T are overall spatial correlation matrices at the receiver and transmitter, respectively. Additionally, if ULAs are deployed at the receiver and transmitter sides, \mathbf{R}_R and \mathbf{R}_T are Toeplitz matrices [123]. To avoid repeated analysis, we only analyse the receiver side in this chapter as the analysis of the transmitter side follows the same procedure. Furthermore, let us denote the complex gain between the k th ($k = 1, 2, \dots, \Omega$) scatterer and the m th ($m = 1, 2, \dots, M_R$) antenna as s_{mk}^R , and the complex gain between the k th scatterer and the n th ($n = 1, 2, \dots, M_R$) antenna as s_{nk}^R . Assume that there are infinite scatterers in the scattering environment, i.e., $\Omega \rightarrow \infty$. Let $B_{R,mn}$ be the spatial correlation coefficient between the m th and the n th antennas and the entry of matrix \mathbf{B}_R in the m th row and n th column. Then, $T_{R,mn}$

can be computed as

$$B_{R,mn} = \frac{\mathbb{E} [s_m^R (s_n^R)^*]}{\sqrt{\sum_k |s_{mk}^R|^2 / \Omega} \sqrt{\sum_k |s_{nk}^R|^2 / \Omega}} = \frac{\sum_k s_{mk}^R (s_{nk}^R)^*}{\sqrt{\sum_k |s_{mk}^R|^2} \sqrt{\sum_k |s_{nk}^R|^2}}. \quad (5.3)$$

In the conventional KBSM, the above discussion implies that all the antennas share the same set of scatterers. In this case, \mathbf{R}_R is equivalent to \mathbf{B}_R , i.e., $\mathbf{B}_R = \mathbf{R}_R$. However, the equivalence between \mathbf{B}_R and \mathbf{R}_R may not hold if antennas do not share the same set of scatterers. This will be studied in later paragraphs.

5.2.2 Proposed KBSM–BD–AA

It was reported in [1] and [87] that each antenna on a large antenna array may not observe the same set of scatterers. Scatterers may appear or disappear on the array axis. Examples of scatter set evolution on the array axis are illustrated in Fig. 5.1. The same set of scatterers are observed by all the antenna elements for conventional MIMO as discussed in Section 5.2.1. On the other hand, for massive MIMO, different antennas may observe different scatters. In Fig. 5.1, Antenna 1 in the massive MIMO observes Scatterers 1, 2 and 3, while Antenna k observes Scatterers 1, 4 and 5. Antennas 1 and k only have Scatterer 1 in common. We refer this effect as the evolution of scatterer sets on the *array axis*. Therefore, the proposed KBSM–BD–AA is developed to characterise this effect for massive MIMO channels.

The BD process was applied to cluster evolution on the time axis in [100] and [111]. In this chapter, the BD process is adapted to modelling the evolution of scatterer sets on the array axis. BD process on the array axis consists of two parts. First, scatterers survive during the evolution of the scatterer set on the array axis. Second, new scatterers are generated when the scatterer set evolves. As a result, the scatterers in the scatterer set of the m th antenna may not be the same as those of the n th antenna. Let the scatterer set of the m th antenna be \mathcal{S}_m . The number of scatterers shared by both the m th and n th antennas is determined by the scatterer survival probability. According to the BD process, the survival probability $E_{R,mn}$ of scatterers when they

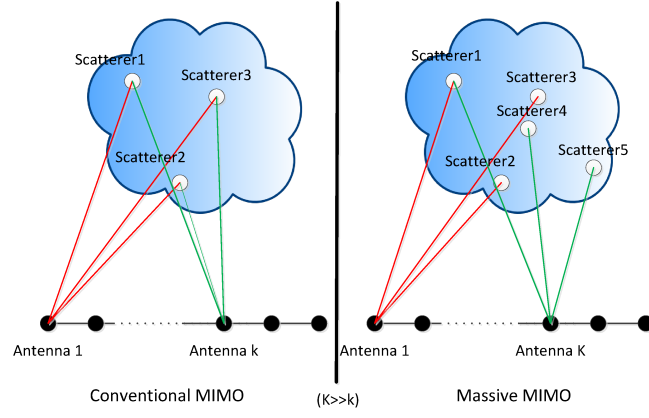


FIGURE 5.1: Diagram of scatterer set evolution on the array axis for massive MIMO.

evolve from the m th antenna to the n th antenna can be modeled as an exponential function [115]

$$\Pr\{s_{nk} \in \mathcal{S}_m\} = E_{R,mn} = e^{-\beta|m-n|}, \quad \forall k \quad (5.4)$$

where $\beta \geq 0$ is a parameter describing how fast a scatterer disappears on the array axis. The value of $E_{R,mn}$ is decreasing if m and n differ more. This implies that less scatterers are shared if two antennas are more separated. Let $B'_{R,mn}$ be the antenna correlation between the m th and n th antennas considering the evolution of scatterer sets on the array axis. Then, $B'_{R,mn}$ can be modeled as

$$\begin{aligned} B'_{R,mn} &= \frac{\mathbb{E} [s_m^R (s_n^R)^*]}{\sqrt{\sum_k |s_{mk}^R|^2 / \Omega} \sqrt{\sum_k |s_{nk}^R|^2 / \Omega}} \\ &= \frac{\sum_k s_{mk}^R (s_{nk}^R)^* \Pr\{s_{nk} \in \mathcal{S}_m\}}{\sqrt{\sum_k |s_{mk}^R|^2} \sqrt{\sum_k |s_{nk}^R|^2}} = E_{R,mn} B_{R,mn}. \end{aligned} \quad (5.5)$$

It can be observed that the antenna correlation of KBSM-BD-AA for massive MIMO is equal to the antenna correlation of KBSM for conventional MIMO multiplied by a factor of $E_{R,mn}$. This is because only $E_{R,mn}$ of the scatterers for the m th antenna are able to survive to be observed by the n th antenna. At the same time, although there may be new scatterers generated according to the BD process, these newly generated

scatterers are uncorrelated to the survived scatterers. Therefore, the newly generated scatterers do not contribute to the antenna correlation.

5.2.3 Discussions

Let us now compare the conventional KBSM and the proposed KBSM–BD–AA. All antennas observe the same set of scatterers for conventional KBSM. The decrease of the spatial correlation function (5.3) of the conventional KBSM is purely determined by the spatial difference between antennas. On the other hand, the spatial correlation function (5.5) of the proposed KBSM–BD–AA is calculated by not only the spatial difference between antennas but also the scatterer set difference. The latter difference is more significant in massive MIMO when the antenna array is large.

Furthermore, the scatterer evolution on the array axis is memoryless. Namely, the survival probability of scatterers evolving from the n th antenna to the m th antenna (denoted as $\Pr\{n \rightarrow m\}$) is equal to that of scatterers evolving from the n th antenna to the m th antenna via an intermediate v th antenna (denoted as $\Pr\{n \rightarrow v \rightarrow m\}$, $n \leq v \leq m$). This can be expressed as

$$\begin{aligned}\Pr\{n \rightarrow v \rightarrow m\} &= \Pr\{n \rightarrow v\} \Pr\{v \rightarrow m\} \\ &= e^{-\beta(m-v)} e^{-\beta(m-n)} = e^{-\beta(m-n)} = \Pr\{n \rightarrow m\}.\end{aligned}\quad (5.6)$$

Let $\mathbf{E}_R = [E_{R,mn}]_{M_R \times M_R}$ ($m, n = 1, 2, \dots, M_R$) and $\mathbf{E}_T = [E_{T,pq}]_{M_T \times M_T}$ ($p, q = 1, 2, \dots, M_T$) denote the survival probability matrices at the receiver side and transmitter side. The overall antenna correlation matrices \mathbf{R}_R and \mathbf{R}_T can be represented as $\mathbf{R}_R = \mathbf{B}_R \circ \mathbf{E}_R$ and $\mathbf{R}_T = \mathbf{B}_T \circ \mathbf{E}_T$ where \circ denotes the Hadamard product.

5.3 Channel Capacity Analysis

In this section, channel capacity of the proposed KBSM–BD–AA in both the low and high SNR regimes will be investigated. The normalised channel capacity without

channel knowledge at the transmitter side can be computed as [13]

$$C(\rho) = \frac{1}{M_R} \log_2 \det \left(\mathbf{I} + \frac{\rho}{M_T} \mathbf{R}_R^{\frac{1}{2}} \mathbf{H}_w \mathbf{R}_T \mathbf{H}_w^H \mathbf{R}_R^{\frac{H}{2}} \right) \quad (5.7)$$

where ρ is designated as SNR and \mathbf{I} is the identity matrix.

For the sake of brevity, the term ‘capacity’ means the normalised capacity (normalised with respect to bandwidth and the number of receive antennas) unless further clarification is provided.

5.3.1 Low SNR approximation

In the low SNR regime, the channel capacity can be analysed with the classic Shannon’s capacity function. However, it was stated in [125] and [37] that the channel capacity can be sufficiently well approximated in the first order with respect to energy per bit to noise ratio $\frac{E_b}{N_0}$ (decibels) in the low SNR regime. Therefore, the low SNR approximation is formulated as [37], [125]

$$\mathcal{C} \left(\frac{E_b}{N_0} \right) \approx \frac{S_0}{M_R} \log_2 \left(\frac{\frac{E_b}{N_0}}{\frac{E_b}{N_0}_{\min}} \right) = \frac{S_0}{10 M_R \log_{10} 2} \left[\frac{E_b}{N_0} (\text{dB}) - \frac{E_b}{N_0}_{\min} (\text{dB}) \right] \quad (5.8)$$

where $\frac{E_b}{N_0}_{\min} = \frac{\ln 2}{M_R}$ is the minimum energy per bit to noise ratio for reliable communications which decreases as the number of receive antennas increases. The capacity slope S_0 is expressed as [37]

$$S_0 = \frac{2 M_T M_R}{M_T \zeta(\mathbf{R}_R) + M_R \zeta(\mathbf{R}_T)} \quad (5.9)$$

where $\zeta(\cdot)$ is the dispersion of a matrix. For a $n \times n$ positive-definite matrix $\mathbf{\Theta}$, its dispersion can be calculated as $\zeta(\mathbf{\Theta}) = \frac{\text{trace}(\mathbf{\Theta}^2)}{n}$ [37]. It can be easily seen in (5.8) that the channel capacity $\mathcal{C} \left(\frac{E_b}{N_0} \right)$ is a linear function of energy per bit to noise ratio $\frac{E_b}{N_0}$ (decibels) in the low SNR regime.

5.3.1.1 Capacity upper bound ($\rho \rightarrow 0$)

Since the dispersion of the correlation matrix $\zeta(\mathbf{R}_R)$ is equal to or larger than 1, the slope S_0 is upper bounded by [37]

$$S_0 \leq \frac{2M_T M_R}{M_T + M_R}. \quad (5.10)$$

As a result, the capacity upper bound $\mathcal{C}^U\left(\frac{E_b}{N_0}\right)$ in the low SNR regime can be shown as

$$\mathcal{C}\left(\frac{E_b}{N_0}\right) \leq \frac{2}{\gamma + 1} \log_2 \left(\frac{\frac{E_b}{N_0}}{\frac{E_b}{N_{0\min}}} \right) = \mathcal{C}^U\left(\frac{E_b}{N_0}\right). \quad (5.11)$$

Equality holds true when the antennas are uncorrelated.

5.3.1.2 Capacity lower bound ($\rho \rightarrow 0$)

Let $E_{R,z} = E_{R,mn}$ and $T_{R,z} = T_{R,mn}$ such that z is the absolute index difference defined by $z = |m - n|$. Then, the dispersion of the correlation matrix \mathbf{R}_R can be calculated as [37]

$$\zeta(\mathbf{R}_R) = 1 + \frac{2}{M_R} \sum_{z=1}^{M_R-1} (M_R - z) |E_{R,z}|^2 |T_{R,z}|^2. \quad (5.12)$$

It should be noticed that the absolute value of spatial correlation between two antennas is less than or equal to 1, i.e., $|T_{R,z}| \leq 1$. Consequently, the dispersion $\zeta(\mathbf{R}_R)$ is upper bounded by

$$\begin{aligned} \zeta(\mathbf{R}_R) &= 1 + \frac{2}{M_R} \sum_{z=1}^{M_R-1} (M_R - z) e^{-2\beta z} |T_{R,z}|^2 \\ &\leq 1 + \frac{2}{M_R} \sum_{z=1}^{M_R-1} (M_R - z) e^{-2\beta z} \rightarrow \frac{1 + e^{-2\beta}}{1 - e^{-2\beta}} \end{aligned} \quad (5.13)$$

as $M_R \rightarrow \infty$. In this case, the slope is bounded by

$$S_0 \geq \frac{2M_TM_R}{M_T + M_R} \left(\frac{1 - e^{-2\beta}}{1 + e^{-2\beta}} \right). \quad (5.14)$$

Consequently, the capacity lower bound $\mathcal{C}^L \left(\frac{\frac{E_b}{N_0}}{\frac{E_b}{N_0 \min}} \right)$ in the low SNR regime can be computed as

$$\mathcal{C} \left(\frac{E_b}{N_0} \right) \geq \frac{2(1 - e^{-2\beta})}{(\gamma + 1)(1 + e^{-2\beta})} \log_2 \left(\frac{\frac{E_b}{N_0}}{\frac{E_b}{N_0 \min}} \right) = \mathcal{C}^L \left(\frac{\frac{E_b}{N_0}}{\frac{E_b}{N_0 \min}} \right). \quad (5.15)$$

Equality holds true when $|T_{R,z}| = 1$, which implies that the antennas are fully correlated and the uncorrelated properties between antennas are solely dominated by the evolution of scatterer sets on the array axis.

5.3.2 High SNR approximation

In the high SNR regime, the channel capacity can be approximated in terms of SNR ρ as [13]

$$C(\rho) \approx C_{\text{iid}}(\rho) + \frac{1}{M_R} [\log_2 \det(\mathbf{R}_R) + \log_2 \det(\mathbf{R}_T)]. \quad (5.16)$$

The channel capacity $C_{\text{iid}}(\rho)$ of an i.i.d. channel with $M_R, M_T \rightarrow \infty$ can be expressed as [36]

$$C_{\text{iid}}(\rho) = \frac{1}{M_R} \log_2 \det \left(\frac{\rho}{M_T} \mathbf{H}_w \mathbf{H}_w^H \right) = \begin{cases} F(1/\gamma, \gamma\rho) & \gamma \leq 1 \\ \frac{1}{\gamma} F(\gamma, \rho) & \gamma \geq 1 \end{cases} \quad (5.17)$$

where

$$\begin{aligned} F(\gamma, \rho) = & \log_2 (1 + \rho(\sqrt{\gamma} + 1)^2) + (\gamma + 1) \log_2 \left(\frac{1 + \sqrt{1 - a}}{2} \right) \\ & - (\log_2 e) \sqrt{\gamma} \frac{1 - \sqrt{1 - a}}{1 + \sqrt{1 - a}} + (\gamma - 1) \log_2 \left(\frac{1 + \alpha}{\alpha + \sqrt{1 - a}} \right) \end{aligned} \quad (5.18)$$

with $a = \frac{4\rho\sqrt{\gamma}}{1 + \rho(\sqrt{\gamma} + 1)^2}$ and $\alpha = \frac{\sqrt{\gamma} - 1}{\sqrt{\gamma} + 1}$.

5.3.2.1 Capacity upper bound ($\rho \rightarrow \infty$)

It was shown in [13] that antenna correlation degrades the channel capacity because $\log_2 \det(\mathbf{R}_R), \log_2 \det(\mathbf{R}_T) \leq 0$. Then, the capacity upper bound $C^U(\rho)$ in the high SNR regime is equivalent to the capacity of i.i.d. channels,

$$C(\rho) \leq C_{\text{iid}}(\rho) = C^U(\rho). \quad (5.19)$$

5.3.2.2 Capacity lower bound ($\rho \rightarrow \infty$)

On the other hand, the capacity lower bound $C^L(\rho)$ in the high SNR regime can be derived from (5.16) as

$$\begin{aligned} C(\rho) &= C_{\text{iid}}(\rho) + \frac{1}{M_R} [\log_2 \det(\mathbf{B}_R \circ \mathbf{E}_R) + \log_2 \det(\mathbf{B}_T \circ \mathbf{E}_T)] \\ &\geq C_{\text{iid}}(\rho) + \frac{1}{M_R} [Q_R + Q_T] \\ &= C^L(\rho) \end{aligned} \quad (5.20)$$

where $Q_R = \max \{\log_2 \det(\mathbf{B}_R), \log_2 \det(\mathbf{E}_R)\}$ and $Q_T = \max \{\log_2 \det(\mathbf{B}_T), \log_2 \det(\mathbf{E}_T)\}$ are derived based on the Schur-Oppenheim inequality [126], [127].

Matrices \mathbf{E}_R and \mathbf{E}_T caused by scatterer set evolution decorrelate antennas in addition to antenna spacings. Since \mathbf{E}_R and \mathbf{E}_T are exponential correlation matrices with a Toeplitz structure and $M_R, M_T \gg 1$, their determinants can be approximated as [128]

$$\det(\mathbf{E}_R) \approx (1 - e^{-2\beta})^{M_R-1} \quad (5.21)$$

$$\log_2 \det(\mathbf{E}_R) \approx (M_R - 1) \log_2 (1 - e^{-2\beta}). \quad (5.22)$$

Moreover, as \mathbf{B}_R and \mathbf{B}_T are large-dimension Toeplitz matrices, the logarithms of their determinants are able to be solved by the Szego's theorem [129] and tend to constants as $M_R, M_T \rightarrow \infty$. Hence, it can be observed in (5.20) that, provided a

scattering environment, the gap between the capacity lower bound and the capacity upper bound does not vary with SNR.

As a special case, we assume that the normalised antenna spacing is 0.5 and the scattering environment is isotropic. Then, the spatial correlation between antennas can be characterised by the zero-th order Bessel function of the first kind $J_0(\cdot)$, i.e., $T_{R,z} = J_0(\pi z)$ [34]. According to the Szego's theorem [129], if the entries of the first column of a large Toeplitz matrix (size tends to infinity) are able to be written as the Fourier transform of a function $f(\omega)$ as

$$T_{R,z} = \frac{1}{2\pi} \int_{-\pi}^{\pi} f(\omega) e^{-iz\omega} d\omega, \quad (5.23)$$

the logarithm of the determinant of the correlation matrix \mathbf{B}_R can then be calculated as [129]

$$\log_2 \det(\mathbf{B}_R) = \frac{M_R}{2\pi} \int_{-\pi}^{\pi} \ln f(\omega) e^{-iz\omega} d\omega \quad (5.24)$$

as $M_R \rightarrow \infty$. The function $f(\omega)$ can be computed by taking the inverse Fourier transform of $T_{R,z}$ [130]. As a result, $f(\omega)$ is computed as

$$f(\omega) = \int_{-\infty}^{\infty} T_{R,z} e^{iz\omega} dz = \int_{-\infty}^{\infty} J_0(\pi z) e^{iz\omega} dz = \frac{2}{\sqrt{\pi^2 - \omega^2}} \quad (|\omega| < \pi). \quad (5.25)$$

Therefore, combining the receiver and transmitter sides, the capacity lower bound of a massive MIMO system with half-wavelength arrays under isotropic scattering environment in the high SNR regime can be derived as

$$\begin{aligned} C^L(\rho) &\approx C_{\text{iid}}(\rho) + \max \left\{ \frac{M_R + M_T}{2\pi M_R} \int_{-\pi}^{\pi} \ln f(\omega) d\omega, \frac{M_R + M_T - 2}{M_R} \log_2(1 - e^{-2\beta}) \right\} \\ &= C_{\text{iid}}(\rho) + \max \left\{ \frac{1 + 1/\gamma}{2\pi} \int_{-\pi}^{\pi} \ln \frac{2}{\sqrt{\pi^2 - \omega^2}} d\omega, \left(1 + \frac{1}{\gamma}\right) \log_2(1 - e^{-2\beta}) \right\} \\ &= C_{\text{iid}}(\rho) + \left(1 + \frac{1}{\gamma}\right) \max \left\{ \log_2\left(\frac{e}{\pi}\right), \log_2(1 - e^{-2\beta}) \right\} \end{aligned} \quad (5.26)$$

as $M_R, M_T \rightarrow \infty$. In this case, the gap between the capacity lower bound and the capacity upper bound is a constant $\left(1 + \frac{1}{\gamma}\right) \max \left\{ \log_2\left(\frac{e}{\pi}\right), \log_2(1 - e^{-2\beta}) \right\}$.

5.4 Results and Discussions

Fig. 5.2 shows the number of scatterers of different antennas shared with Antenna 1. Fewer scatterers are in common as the indices increase. Also, the parameter β controls the survival probability of scatterers. The value of β can be tuned to adapt to different scattering environments.

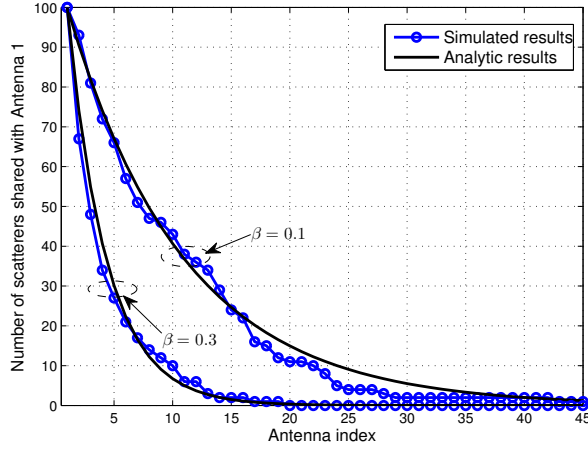


FIGURE 5.2: Number of scatterers shared with Antenna 1 in terms of antenna indices (100 initial scatterers in Antenna 1).

Antenna correlation with BD process of scatterers on the array axis for massive MIMO is compared with antenna correlation of conventional MIMO in Fig. 5.3. Lower antenna correlation with BD process can be observed because of the different scatterer sets between different antennas. The gap enlarges when the normalised antenna spacing increases. Moreover, larger values of β result in more significant drop of antenna correlations.

The capacity analysis of the proposed KBSM-BD-AA in the low SNR regime is depicted in Fig. 5.4. The analytic capacity upper bound is the linear approximation under the i.i.d. channel assumption as derived in (5.11). The linearly approximated capacity upper bound aligns well with the simulated (exact) i.i.d. channel capacity in the low SNR regime. Next, the analytic capacity lower bound of the KBSM-BD-AA is the linear approximation based on the fully correlated channel assumption as derived in (5.15). In this case, the scatterer evolution on the array axis is solely responsible

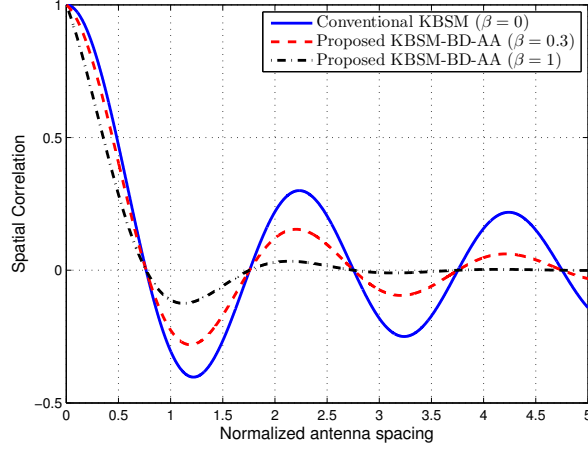


FIGURE 5.3: Antenna spatial correlation for the KBSM-BD-AA (isotropic scattering environment).

for the uncorrelated properties of the channel. It can be observed that the linear approximation of the capacity lower bound of the KBSM-BD-AA has a significantly smaller slope than that of an i.i.d. channel. The decrease of the slope is caused by antenna correlations. It is demonstrated by simulation that the linear approximation of the capacity lower bound matches the exact channel capacity properly. The simulated (exact) capacity of the KBSM-BD-AA in an isotropic scattering environment lies between the upper and lower bounds. It should be noticed that these linear approximations are sufficiently accurate when the SNR tends to 0. As SNR increases, the gap between linear approximations and simulated results enlarges.

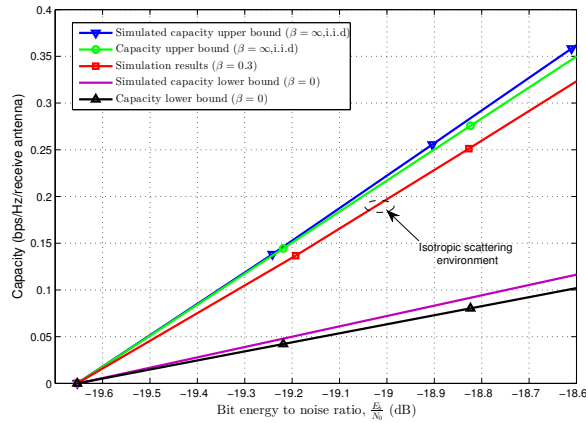


FIGURE 5.4: Capacity analysis in the low SNR regime for the KBSM-BD-AA ($M_R = M_T = 64$).

Fig. 5.5 illustrates the upper and lower capacity bounds of the KBSM–BD–AA in an isotropic scattering environment as well as the simulation results in the high SNR regime. It can be noticed that simulation results match analytic derivations well. In addition, the gap between the upper and lower bounds is constant when the SNR is high. Again, the simulated capacity of the KBSM–BD–AA lies within the upper and lower bounds.

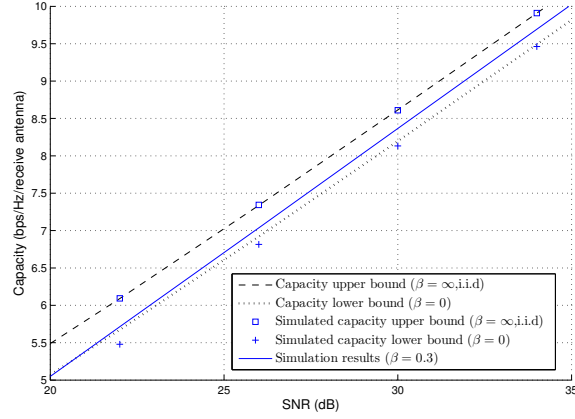


FIGURE 5.5: Capacity analysis in the high SNR regime for the KBSM–BD–AA ($M_R = M_T = 64$, half-wavelength ULAs, isotropic scattering environment).

Cumulative Distribution Functions (CDFs) of capacities of the KBSM–BD–AA in an isotropic scattering environment are shown in Fig. 5.6. SNR is set to be 25 dB. These CDFs of capacities are shifted by different values of β . The gap of capacity medians between $\beta = 0$ and $\beta = \infty$ is approximately 0.55 bps/Hz/receive antenna.

5.5 Summary

A novel KBSM–BD–AA for massive MIMO has been proposed in this chapter. The evolution of scatterer sets on the array axis has been modeled by the BD process. With this consideration, the overall antenna correlation matrix is equivalent to the Hadamard product of the spatial correlation matrix and survival probability matrix. Upper and lower bounds of channel capacities have been analysed in both the high and low SNR regimes when the numbers of transmit and receive antennas are increasing unboundedly with a constant ratio. The BD process on the array axis additionally

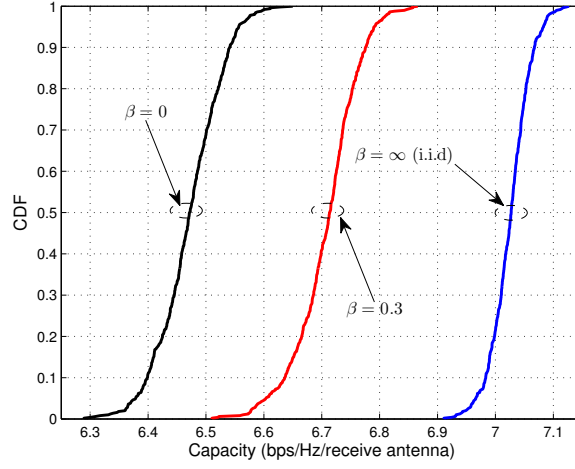


FIGURE 5.6: CDFs of capacities of the KBSM-BD-AA with different values of β (SNR=25dB, $M_R = M_T = 64$, half-wavelength ULAs, isotropic scattering environment).

decreases correlations between antennas since antennas in a large array may observe different sets of scatterers.

Chapter 6

A Unified Framework for 5G Wireless Channel Models

6.1 Introduction

To satisfy the demand of the Fifth Generation (5G) wireless communication networks, known as improved data rate, reduced latency, energy, and cost [131], a number of advanced technologies have been proposed in the literature as potential 5G technologies. Massive Multiple-Input Multiple-Output (MIMO), an enhanced MIMO technique with a large number of antennas, is able to highly improve communication reliability, spectral efficiency, and energy efficiency [22], [23], [103], [132]. It is predicted that each user will possess many interconnected mobile devices. Machine-to-Machine (M2M) communications [27], [133] were proposed in the heterogeneous network architecture of 5G to enable devices to connect mutually without base stations. High-Speed Train (HST) communication also attracts attention for the emerging development of high mobility trains with speed expected to be higher than 500 km/h. Furthermore, Milli-meter Wave (mmWave) frequency bands (30–300 GHz) have been proposed to be used for 5G wireless communications to solve the spectrum crisis problem. The mmWave frequency bands are capable of providing large bandwidth (in the order of GHz) and exploiting polarisation and massive MIMO [134]–[136]. In order to design

and evaluate 5G systems, a channel model which can capture channel characteristics of the above-mentioned potential technologies is essential. Since Geometry-Based Stochastic Models (GBSMs) have widely been used to model small-scale channel fading [34] and are widely standardised [30], [48], [52], we will focus on GBSMs and small-scale fading in this chapter. Recently, the first GBSM for 5G wireless channel models was proposed by the METIS project [47]. However, the METIS GBSM did not sufficiently support channel characteristics of massive MIMO, M2M, and mmWave communications [47, Table 4–1].

6.1.1 Related work I: GBSMs for massive MIMO

A Two-Dimensional (2-D) confocal ellipse massive MIMO channel model was proposed in [113] and [42]. In addition, a Three-Dimensional (3-D) twin-cluster massive MIMO channel model was proposed in [51]. Both the ellipse model and twin-cluster model in [42], [51], [113] employed the spherical wavefront assumption and adapted the cluster Birth-Death (BD) process in [100] and [111] to both the time and array axes to characterise cluster appearance and disappearance. However, the mean power evolution of clusters was ignored in [42], [51], [113]. Also, channel models in [42], [51], [113] were not designed to accommodate mmWave channels.

6.1.2 Related work II: GBSMs for M2M and HST

In M2M channels, the transmitter, scatterers, and receiver can be all moving. They are also known as Vehicle-to-Vehicle (V2V) channels, if high mobility is envisioned. Doppler frequencies at both the transmitter and receiver should be taken into account. Wideband 2-D GBSMs for V2V channels were proposed in [43], [117], [137], where clusters were categorised into mobile scatterers and static clusters. In M2M communications, transmitters and receivers may be lower than clusters on surrounding buildings. Therefore, 3-D clusters were included in [55]–[57]. A 3-D concentric-cylinder V2V channel model was introduced in [55], while 3-D GBSMs combining a two-sphere model and an elliptic-cylinder model were proposed in [57] and [56].

For HST communications, relevant GBSMs can be found in [40] and [2]. The non-stationary channel behavior of HST systems is similar to that of V2V channels with larger Doppler frequencies. However, cluster evolution on the time axis was ignored in [2], [40], [43], [55]–[57], [117], [137]. Thus, it is difficult to track the channel with respect to time in a continuous manner.

6.1.3 Related work III: GBSMs for mmWave

As the supported bandwidth for mmWave is large (in the order of GHz [134]–[136]), GBSMs for mmWave channels need to consider high time resolution, i.e., rays within a cluster may be resolvable and the numbers of rays within clusters may vary. The GBSM of the METIS channel model [47] considered resolvable rays within clusters, but the varying numbers of rays within clusters were not included. The Saleh-Valenzuela (SV) channel model [65] was proposed to satisfy requirements of mmWave channels. In a SV channel model, the number of rays within each cluster was assumed to follow the Poisson distribution. Complex gain and delay were assigned to each ray. The SV channel model has been used to evaluate system performance in the IEEE wireless Personal Area Network (PAN) standard [138]–[141] with the supported bandwidth over 500 MHz. In addition, applications of the SV channel model to mmWave channels can be found in [66], [142], [143]. However, time evolution of the SV channel model has not been sufficiently studied in the literature. Also, GBSMs considering both massive MIMO and mmWave bands are missing.

6.1.4 Contributions

To sum up, the contributions of this chapter can be listed as follows:

1. A unified 3-D non-stationary GBSM framework is proposed, which has the capability to simulate massive MIMO, M2M, HST, and mmWave channels. It also considers time evolution of channels with all the model parameters time varying. The conventional WINNER II channel model is combined with the SV channel

model to support the high time resolution of mmWave channels. Doppler frequencies at both the transmitter and receiver sides are assumed to support M2M features. Spherical wavefront and array-time evolution modeled are included to represent massive MIMO channel characteristics. Array-time evolution includes cluster BD process in both the array and time axes and geometrical relationship updates. The mean power updates of rays are also embedded in the proposal 5G channel model with the assumption of the inverse square law. In addition, polarised directional antennas and 3-D features are taken into account. The proposed unified 5G GBSM framework can serve as a basis for future standardised channel models.

2. The proposed unified 5G GBSM framework can easily be adapted to various scenarios by setting proper channel parameters, which is demonstrated by fitting certain statistical properties to the corresponding measurement data.

The rest of this chapter is organised as follows. Section 6.2 gives a general description of the proposed unified framework for 5G channel models. Statistical properties of the proposed unified 5G GBSM framework are investigated in Section 6.3. Simulation results and analysis are presented in Section 6.4. Conclusions are drawn in Section 6.5.

6.2 A Unified Framework for 5G Wireless Channel Models

Let us consider a MIMO system with M_R receive and M_T transmit antennas communicating at carrier frequency f_c . Let Ant_q^R denote the q th receive antenna and Ant_p^T denote the p th transmit antenna ($1 \leq q \leq M_R, 1 \leq p \leq M_T$). Also, let Cluster_n denote the n th cluster. Uniform linear arrays (ULAs) with receive antenna spacing δ_R and transmit antenna spacing δ_T are assumed for description convenience. It should be mentioned that the calculations of channel coefficients depend only on geometry relationships between objects in the model and are independent to the layout of antenna arrays. Therefore, although co-located ULAs are used in this chapter for presentation

convenience, the same modeling approach can be generalised to distributed antenna arrays or 2-D antenna arrays. Antenna responses can be modified subject to actual antenna settings.

The scattering environment between the transmitter and receiver is abstracted as effective clusters [30], which characterise the first and last bounces of the channel. Multi-bounces between the first and last bounces are abstracted by a virtual link [50]. The proposed unified 3-D 5G GBSM framework is illustrated in Fig. 6.1. It should be noticed that (x_G, y_G, z_G) axes are established as the Global Coordinate System (GCS). This needs to be distinguished from the Local Coordinate System (LCS) when calculating antenna pattern in a 3-D space. Spherical wavefront and cluster appearance and disappearance are assumed in order to support massive MIMO scenarios. In this case, each antenna may have its own set of observable clusters. Let $C_q^R(t)$ and $C_p^T(t)$ represent the cluster sets of Ant_q^R and Ant_p^T at time t , respectively. Then, the total number of clusters $N(t)$ observable by both the transmitter and receiver at time t can be calculated as

$$N(t) = \text{card} \left(\bigcup_{p=1}^{M_T} \bigcup_{q=1}^{M_R} S_{qp}(t) \right) \quad (6.1)$$

where $S_{qp}(t) = C_q^R(t) \cap C_p^T(t)$, $\text{card}(\mathcal{S})$ denotes the cardinality of the set \mathcal{S} , \bigcup and \bigcap denote the union and intersection of sets, respectively. Also, both the transmitter and receiver are assumed to be in motion to support M2M scenarios, which results in Doppler frequencies at both sides. In addition, rays within clusters are considered to be resolvable in order to support the high time resolution in mmWave scenarios. Complex gain and delay should be assigned to each ray.

Here, we define the central azimuth angle as the angle between the projection of the line segment connecting an object and array center on the x - y plane and the positive x -axis, and define the central elevation angle as the complement angle between the projection of the line segment connecting an object and array center on the x - y plane and the positive z -axis. Given the azimuth and elevation angles at both the receiver and transmitter sides, according to the geometrical relationships in Fig. 6.1 and the key geometrical parameters listed in Table 6.1, the position vectors of Ant_q^R and Ant_p^T

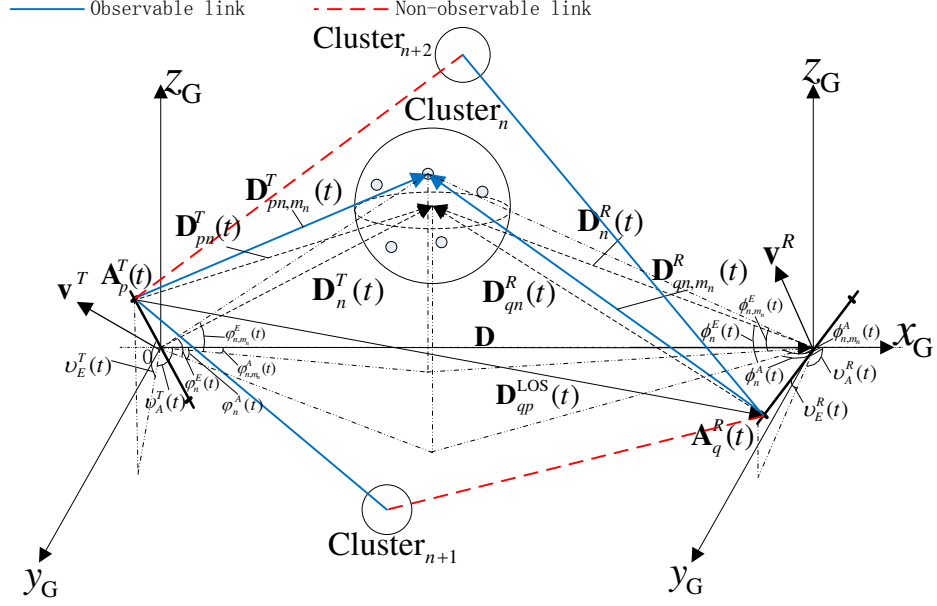


FIGURE 6.1: A unified framework of a 3-D 5G GBSM.

TABLE 6.1: Definitions of key geometry parameters for the 3-D 5G GBSM.

$v_n^R(t), v_n^T(t)$	azimuth and elevation angles of the receive array
$v_A^R(t), v_A^T(t)$	azimuth and elevation angles of the transmit array
$\phi_n^A(t), \phi_n^E(t)$	central azimuth and elevation angles between Cluster _n and the receive array
$\varphi_n^A(t), \varphi_n^E(t)$	central azimuth and elevation angles between Cluster _n and the transmit array
$\phi_{n,m_n}^A(t), \phi_{n,m_n}^E(t)$	central azimuth and elevation angles between the m_n th ray of Cluster _n and the receive array
$\varphi_{n,m_n}^A(t), \varphi_{n,m_n}^E(t)$	central azimuth and elevation angles between the m_n th ray of Cluster _n and the transmit array
$\mathbf{A}_q^R(t), \mathbf{A}_p^T(t)$	3-D position vectors of Ant _q ^R and Ant _p ^T
$\mathbf{D}_n^R(t), \mathbf{D}_n^T(t)$	3-D distance vectors between Cluster _n and the receiver (transmitter) array center
$\mathbf{D}_{n,m_n}^R(t), \mathbf{D}_{n,m_n}^T(t)$	3-D distance vectors between Cluster _n and the receive (transmit) array center via the m_n th ray
$\mathbf{D}_{qn,m_n}^R(t), \mathbf{D}_{pn,m_n}^T(t)$	3-D distance vectors between Cluster _n and Ant _q ^R (Ant _p ^T) via the m_n th ray
$f_{qn,m_n}^R(t), f_{pn,m_n}^T(t)$	Doppler frequencies of Ant _q ^R (Ant _p ^T) via Cluster _n and the m_n th ray
$\mathbf{D}_{qp}^{LOS}(t)$	3-D distance vector of the LOS component between Ant _q ^R and Ant _p ^T
$f_{pq}^{LOS}(t)$	Doppler frequency of the LOS component between Ant _q ^R and Ant _p ^T
$\mathbf{v}_n^R, \mathbf{v}_n^T$	3-D velocity vectors of the receive and transmit arrays
$\mathbf{v}_n^R, \mathbf{v}_n^T$	3-D velocity vectors of the last bounce and first bounce of Cluster _n
$P_{n,m_n}(t)$	mean power of the m_n th ray of Cluster _n
\mathbf{D}	3-D distance vector between the receive and transmit array centers

can be expressed as

$$\mathbf{A}_q^R(t) = \frac{M_R - 2q + 1}{2} \delta_R \begin{bmatrix} \cos v_E^R(t) \cos v_A^R(t) \\ \cos v_E^R(t) \sin v_A^R(t) \\ \sin v_E^R(t) \end{bmatrix}^T + \mathbf{D} \quad (6.2)$$

$$\mathbf{A}_p^T(t) = \frac{M_T - 2p + 1}{2} \delta_T \begin{bmatrix} \cos v_E^T(t) \cos v_A^T(t) \\ \cos v_E^T(t) \sin v_A^T(t) \\ \sin v_E^T(t) \end{bmatrix}^T \quad (6.3)$$

respectively, where \mathbf{D} is assumed to equal $[D, 0, 0]^T$ and D is the initial distance between the transmitter and receiver. The Line-of-Sight (LOS) distance vector $\mathbf{D}_{qp}^{\text{LOS}}(t)$ between Ant_q^R and Ant_p^T is computed as

$$\mathbf{D}_{qp}^{\text{LOS}}(t) = \mathbf{A}_q^R(t) - \mathbf{A}_p^T(t). \quad (6.4)$$

Distance vectors of Cluster _{n} at the transmitter and receiver are calculated as

$$\mathbf{D}_n^R(t) = D_n^R(t) \begin{bmatrix} \cos \phi_n^E(t) \cos \phi_n^A(t) \\ \cos \phi_n^E(t) \sin \phi_n^A(t) \\ \sin \phi_n^E(t) \end{bmatrix}^T + \mathbf{D} \quad (6.5)$$

$$\mathbf{D}_n^T(t) = D_n^T(t) \begin{bmatrix} \cos \varphi_n^E(t) \cos \varphi_n^A(t) \\ \cos \varphi_n^E(t) \sin \varphi_n^A(t) \\ \sin \varphi_n^E(t) \end{bmatrix}^T \quad (6.6)$$

where $D_n^R(t)$ and $D_n^T(t)$ are the Frobenius norms of $\mathbf{D}_n^R(t)$ and $\mathbf{D}_n^T(t)$, respectively. Distance vectors of the m_n th ray of Cluster _{n} to the transmitter and receiver center are calculated as

$$\mathbf{D}_{n,m_n}^R(t) = D_n^R(t) \begin{bmatrix} \cos \phi_{n,m_n}^E(t) \cos \phi_{n,m_n}^A(t) \\ \cos \phi_{n,m_n}^E(t) \sin \phi_{n,m_n}^A(t) \\ \sin \phi_{n,m_n}^E(t) \end{bmatrix}^T + \mathbf{D} \quad (6.7)$$

$$\mathbf{D}_{n,m_n}^T(t) = D_n^T(t) \begin{bmatrix} \cos \varphi_{n,m_n}^E(t) \cos \varphi_{n,m_n}^A(t) \\ \cos \varphi_{n,m_n}^E(t) \sin \varphi_{n,m_n}^A(t) \\ \sin \varphi_{n,m_n}^E(t) \end{bmatrix}^T. \quad (6.8)$$

Distance vectors between the m_n th ray of Cluster $_n$ and antenna elements are calculated as

$$\mathbf{D}_{qn,m_n}^R(t) = \mathbf{D}_{n,m_n}^R(t) - \mathbf{A}_q^R(t) \quad (6.9)$$

$$\mathbf{D}_{pn,m_n}^T(t) = \mathbf{D}_{n,m_n}^T(t) - \mathbf{A}_p^T(t). \quad (6.10)$$

It should be noticed that position vectors are all time dependent. After all vectors are obtained in the 3-D space, the channel impulse response can be derived.

6.2.1 Channel impulse response

Based on the WINNER II and SV channel models, the proposed 5G GBSM at time t with delay τ can be characterised by an $M_R \times M_T$ matrix $\mathbf{H}(t, \tau) = [h_{qp}(t, \tau)]$. The entries of $\mathbf{H}(t, \tau)$ consist of two components, i.e., the LOS component and the Non-LOS (NLOS) component, and can be written as

$$\begin{aligned} h_{qp}(t, \tau) = & \underbrace{\sqrt{\frac{K(t)}{K(t) + 1}} h_{qp}^{\text{LOS}}(t) \delta(\tau - \tau^{\text{LOS}}(t))}_{\text{LOS}} \\ & + \underbrace{\sqrt{\frac{1}{K(t) + 1}} \sum_{n=1}^{N(t)} \sum_{m_n=1}^{M_n(t)} h_{qp,n,m_n}(t) \delta(\tau - \tau_n(t) - \tau_{m_n}(t))}_{\text{NLOS}}. \end{aligned} \quad (6.11)$$

In (6.11), $K(t)$ is the Rician factor, $N(t)$ is the time variant number of clusters, $M_n(t)$ is the number of rays within Cluster $_n$, $\tau_n(t)$ is the delay of Cluster $_n$ and $\tau_{m_n}(t)$ is the relative delay of the m_n th ray in Cluster $_n$. It is important to mention that all the parameters of the proposed 5G GBSM are time-variant, which has the capability to model the time-evolution and high mobility features of channels and is essentially a non-stationary channel model. It is assumed that the Rician factor and relative delays are constants during the generation of channel coefficients, i.e., $K(t) = K$ and $\tau_{m_n}(t) = \tau_{m_n}$. These may not hold in certain scenarios such as the HST cutting scenario where the Rician factor is changing with time [144]. However, the cutting scenario is not frequent in 5G scenarios and it is of high complexity. Therefore, we assume that the Rician factor is unchanged within the interval of channel coefficient

generation to simplify the model. The same principle applies to relative delays. Also, the number of rays within a cluster is assumed to follow a Poisson distribution $\text{Pois}(\tilde{\lambda})$ [143], i.e., $M_n(t) = M_n = \max\{\text{Pois}(\tilde{\lambda}), 1\}$, where $\tilde{\lambda}$ is both the mean and variance of M_n and $\max\{\cdot\}$ calculates the maximum value. Each ray within a cluster has its own complex gain and delay to support mmWave channels in the proposed 5G GBSM. Also, following the assumption in the WINNER II channel model, AoAs and AoDs are independent.

For the LOS component, if polarised antenna arrays are assumed at both the receiver and transmitter sides, the complex channel gain $h_{qp}^{\text{LOS}}(t)$ is presented as

$$h_{qp}^{\text{LOS}}(t) = \begin{bmatrix} F_{p,V}^T(\mathbf{D}_{qp}^{\text{LOS}}(t), \mathbf{A}_p^T(t)) \\ F_{p,H}^T(\mathbf{D}_{qp}^{\text{LOS}}(t), \mathbf{A}_p^T(t)) \end{bmatrix}^T \begin{bmatrix} e^{j\Phi_{\text{LOS}}^{\text{VV}}} & 0 \\ 0 & e^{j\Phi_{\text{LOS}}^{\text{HH}}} \end{bmatrix} \begin{bmatrix} F_{q,V}^R(\mathbf{D}_{qp}^{\text{LOS}}(t), \mathbf{A}_q^R(t)) \\ F_{q,H}^R(\mathbf{D}_{qp}^{\text{LOS}}(t), \mathbf{A}_q^R(t)) \end{bmatrix} \times \\ e^{j2\pi f_{qp}^{\text{LOS}}(t)t} e^{j\Phi_{qp}^{\text{LOS}}(t)} \quad (6.12)$$

where $\Phi_{\text{LOS}}^{\text{VV}}$ and $\Phi_{\text{LOS}}^{\text{HH}}$ are uniformly distributed within $(0, 2\pi)$. The superscripts V and H denote vertical polarisation and horizontal polarisation, respectively. Antenna patterns $F^T(\cdot, \cdot)$ and $F^R(\cdot, \cdot)$ are calculated in Appendix A, and they can be modified according to practical antenna pattern settings. The Doppler frequency $f_{qp}^{\text{LOS}}(t)$ between Ant_q^R and Ant_p^T of the LOS component is expressed as

$$f_{qp}^{\text{LOS}}(t) = \frac{1}{\lambda} \frac{\langle \mathbf{D}_{qp}^{\text{LOS}}(t), \mathbf{v}^R - \mathbf{v}^T \rangle}{\|\mathbf{D}_{qp}^{\text{LOS}}(t)\|} \quad (6.13)$$

where $\langle \cdot, \cdot \rangle$ is the inner product operator, $\|\cdot\|$ calculates the Frobenius norm, and λ is the wavelength of the carrier. Given the initial phase Φ_0 and the speed of light c , the phase $\Phi_{qp}^{\text{LOS}}(t)$ and delay $\tau^{\text{LOS}}(t)$ of the LOS component are computed as

$$\Phi_{qp}^{\text{LOS}}(t) = \Phi_0 + \frac{2\pi}{\lambda} \|\mathbf{D}_{qp}^{\text{LOS}}(t)\| \quad (6.14)$$

$$\tau^{\text{LOS}}(t) = \|\mathbf{D}(t)\| / c. \quad (6.15)$$

For NLOS components, if Cluster_n is observable to Ant_q^R and Ant_p^T , i.e., $\text{Cluster}_n \in S_{qp}(t)$, the complex channel gain is expressed as

$$h_{qp,n,m_n}(t) = \begin{bmatrix} F_{p,V}^T(\mathbf{D}_{n,m_n}^T(t), \mathbf{A}_p^T(t)) \\ F_{p,H}^T(\mathbf{D}_{n,m_n}^T(t), \mathbf{A}_p^T(t)) \end{bmatrix}^T \begin{bmatrix} e^{j\Phi_{n,m_n}^{VV}} & \sqrt{\kappa}e^{j\Phi_{n,m_n}^{VH}} \\ \sqrt{\kappa}e^{j\Phi_{n,m_n}^{HV}} & e^{j\Phi_{n,m_n}^{HH}} \end{bmatrix} \begin{bmatrix} F_{q,V}^R(\mathbf{D}_{n,m_n}^R(t), \mathbf{A}_q^R(t)) \\ F_{q,H}^R(\mathbf{D}_{n,m_n}^R(t), \mathbf{A}_q^R(t)) \end{bmatrix} \times \sqrt{P_{n,m_n}(t)} e^{j2\pi f_{qn,m_n}^R(t)t} e^{j2\pi f_{pn,m_n}^T(t)t} e^{j\Phi_{qp,n,m_n}(t)} \quad (6.16)$$

where κ is the cross polarization power ratio and P_{n,m_n} is the normalised mean power of the m_n th ray in Cluster_n . The normalised mean power of Cluster_n can be calculated as $P_n = \sum_{m_n} P_{n,m_n}$. Random phases $\Phi_{n,m_n}^{VV}, \Phi_{n,m_n}^{VH}, \Phi_{n,m_n}^{HV}, \Phi_{n,m_n}^{HH}$ are uniformly distributed over $(0, 2\pi)$.

Conversely, if Cluster_n is not observable, i.e., $\text{Cluster}_n \notin S_{qp}(t)$, the complex channel gain

$$h_{qp,n,m_n}(t) = 0. \quad (6.17)$$

Accordingly, the Doppler frequencies at the receiver and transmitter are calculated as

$$f_{qn,m_n}^R(t) = \frac{1}{\lambda} \frac{\langle \mathbf{D}_{qn,m_n}^R(t), \mathbf{v}^R - \mathbf{v}_n^R \rangle}{\|\mathbf{D}_{qn,m_n}^R(t)\|} \quad (6.18)$$

$$f_{pn,m_n}^T(t) = \frac{1}{\lambda} \frac{\langle \mathbf{D}_{pn,m_n}^T(t), \mathbf{v}^T - \mathbf{v}_n^T \rangle}{\|\mathbf{D}_{pn,m_n}^T(t)\|}. \quad (6.19)$$

Moreover, the phase $\Phi_{qp,n,m_n}(t)$ and delay $\tau_n(t)$ of the NLOS component are computed as

$$\Phi_{qp,n,m_n}(t) = \Phi_0 + \frac{2\pi}{\lambda} [\|\mathbf{D}_{qn,m_n}^R(t)\| + \|\mathbf{D}_{pn,m_n}^T(t)\|] \quad (6.20)$$

$$\tau_n(t) = [\|\mathbf{D}_n^R(t)\| + \|\mathbf{D}_n^T(t)\|] / c + \tilde{\tau}_n(t) \quad (6.21)$$

where $\tilde{\tau}_n(t)$ is an exponentially distributed random variable representing the virtual

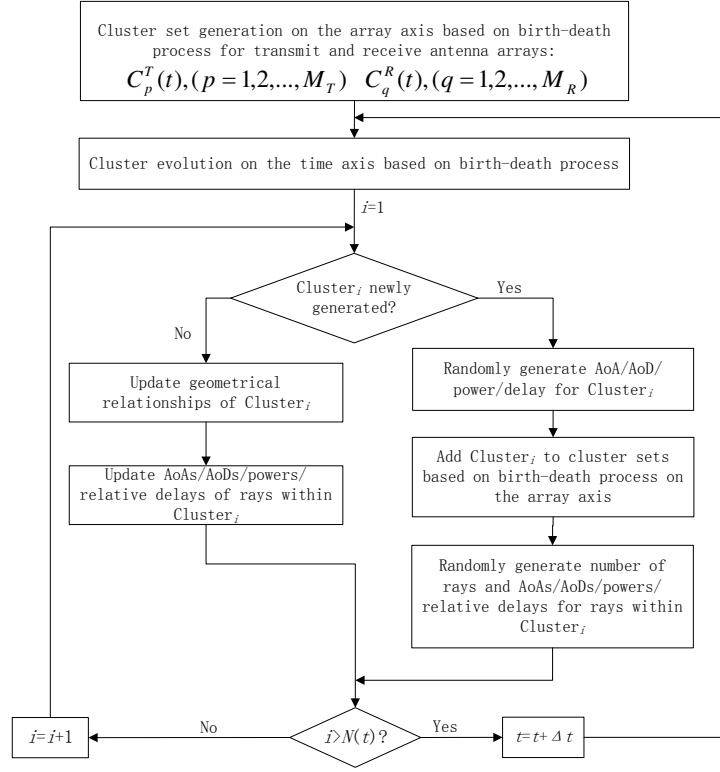


FIGURE 6.2: Flowchart of the array-time cluster evolution for the proposed unified 5G GBSM framework.

delay caused by the virtual link between the first and last bounces of Cluster_n in the scattering environment.

6.2.2 Array-time cluster evolution for the unified 5G GBSM framework

In this chapter, the array-time cluster evolution for the proposed unified 5G GBSM framework is developed based on the BD process and the algorithm described in [51]. However, the proposed algorithm for the unified 5G GBSM framework in Fig. 6.2 improves the one in [51] by including mean power evolution and updates of rays within clusters, as these were not included in [51]. Let us assume the generation and recombination rates of clusters are λ_G and λ_R . Then, the array-time cluster evolution for the unified 5G GBSM framework can be described as follows.

Step 1: An initial set of clusters are generated at time t . The generation procedure of initial clusters will be described in Section 6.2.3.

Step 2: At time $t + \Delta t$, cluster evolution on the time axis is operated. In principle, each cluster should have its own survival probability according to the relative motion. However, for simplicity, mean relative velocities of clusters will be used to calculate survival probabilities of clusters. Mean relative velocities Δv^R and Δv^T are characterised as $\Delta v^R = E[\|\mathbf{v}^R - \mathbf{v}_n^R\|]$ and $\Delta v^T = E[\|\mathbf{v}^T - \mathbf{v}_n^T\|]$. As a result, the survival probability $P_T(\Delta t)$ of a cluster after Δt is computed as

$$P_T(\Delta t) = e^{-\lambda_R \frac{P_F(\Delta v^R + \Delta v^T)\Delta t}{D_c^s}} \quad (6.22)$$

where P_F is the percentage of moving clusters and D_c^s is a scenario-dependent coefficient describing space correlation [51]. The survivability of each cluster at time $t + \Delta t$ is determined by $P_T(\Delta t)$. Geometrical relationships, delays, and mean powers of survived clusters will be updated according to Section 6.2.4. Meanwhile, a random number of new clusters are generated. This random number is generated according to the Poisson distribution with mean

$$E[N_{\text{new}}(t + \Delta t)] = \frac{\lambda_G}{\lambda_R} (1 - P_T(\Delta t)). \quad (6.23)$$

Rays and geometrical parameters will be assigned to these new clusters as described in Section 6.2.3, which also presents the array axis evolution for clusters.

Step 3: When the array-time evolution is finished, the algorithm returns to Step 2 to enter the next time instant.

6.2.3 Generation of new clusters

For a new cluster, say Cluster _{n} , certain parameters such as the number of rays within the cluster, virtual delay, mean power, angular parameters, and relative delays of rays need to be assigned to this cluster. These parameters are randomly generated according to the distributions listed in Table 6.2. The mean power \tilde{P}'_n of clusters is

generated as [30]

$$\tilde{P}'_n = \exp\left(-\tilde{\tau}_n \frac{r_\tau - 1}{r_\tau \mathbb{E}[\tilde{\tau}_n]}\right) 10^{-\frac{Z_n}{10}} \quad (6.24)$$

where r_τ is the delay scalar ($r_\tau = 2.3$ for urban outdoor scenario and $r_\tau = 2.4$ for indoor office scenario [30]) and Z_n follows Gaussian distribution $\mathcal{N}(0, 3)$ [30]. In addition, the mean power generation method of a cluster is extended to compute the mean power of rays within clusters as [143]

$$\tilde{P}'_{n,m_n} = \exp\left(-\tau_{m_n} \frac{r_\tau - 1}{r_\tau \mathbb{E}[\tau_{m_n}]}\right) 10^{-\frac{Z_{n,m_n}}{10}} \quad (6.25)$$

where Z_{n,m_n} follows Gaussian distribution $\mathcal{N}(0, 3)$ [30]. The mean power of rays is then scaled by the cluster power as $\tilde{P}_{n,m_n} = \tilde{P}'_n \frac{\tilde{P}'_{n,m_n}}{\sum_{m_n} \tilde{P}'_{n,m_n}}$. The angular parameters ϕ_n^A , $\phi_n^E, \varphi_n^A, \varphi_n^E$ of Cluster _{n} are assumed to obey wrapped Gaussian distributions. Then, the angular parameters of Cluster _{n} via the m_n th ray can be calculated by adding the angular offset of the ray, i.e.,

$$[\phi_{n,m_n}^A, \phi_{n,m_n}^E, \varphi_{n,m_n}^A, \varphi_{n,m_n}^E]^T = [\phi_n^A, \phi_n^E, \varphi_n^A, \varphi_n^E]^T + [\Delta\phi^A, \Delta\phi^E, \Delta\varphi^A, \Delta\varphi^E]^T \quad (6.26)$$

where $\Delta\phi^A, \Delta\phi^E, \Delta\varphi^A, \Delta\varphi^E$ are angular offsets of the ray, which are assumed to follow Laplace distributions with zero mean and standard deviation of 0.017 radian for simplicity.

TABLE 6.2: Distributions of Parameters of Clusters for the 3-D 5G GBSM.

Parameters	M_n	$\tilde{\tau}_n, \tau_{m_n}, D_n^T, D_n^R$	$\phi_n^A, \phi_n^E, \varphi_n^A, \varphi_n^E$
Distributions	Poisson	Exponential	Wrapped Gaussian

Next, which antennas are able to observe the newly generated cluster should be determined. To avoid repeated description, only the receiver side is presented, the transmitter side follows the same procedure. The survival probability P_A of a cluster evolving from one antenna to an adjacent antenna can be computed as

$$P_A = e^{-\lambda_R \frac{\delta_R}{D_c^{\alpha}}} \quad (6.27)$$

```

1: Generate  $M_n \sim \text{Pois}(\tilde{\lambda})$  rays for the cluster;
2: Generate virtual delay/mean power/distance for the cluster;
3: Generate AoAs/AoDs/relative delays/relative mean powers for the rays within
   the cluster;
4: Generate discrete  $\tilde{q} \sim \text{U}(1, M_R)$  and let  $\tilde{i} = 1, \tilde{j} = 1$ ;
5: while ( $\tilde{u} \sim \text{U}(0, 1) \leq P_A \& \tilde{q} + \tilde{i} \leq M_R$ ) do
6:   Add the cluster to  $C_{(\tilde{q}+\tilde{i})}^R(t)$ ;  $\tilde{i} = \tilde{i} + 1$ ;
7: end while
8: while ( $\tilde{u} \sim \text{U}(0, 1) \leq P_A \& \tilde{q} - \tilde{j} \geq 1$ ) do
9:   Add the cluster to  $C_{(\tilde{q}-\tilde{j})}^R(t)$ ;  $\tilde{j} = \tilde{j} + 1$ ;
10: end while

```

FIGURE 6.3: Psuedo codes for the new cluster generation algorithm.

where D_c^a is the scenario-dependent coefficient normalizing antenna spacings [51]. Then, the newly generated cluster is added to the cluster set of a randomly selected receive antenna. The cluster evolves based on BD process to neighbouring antennas of the selected receive antenna with survival probability P_A . The psuedo codes of new cluster generation algorithm are shown in Fig. 6.3.

6.2.4 Evolution of survived clusters

In order to highlight time evolution of the proposed model, geometrical relationships, virtual delays, and mean powers of survived clusters need to be updated from t to $t + \Delta t$. To begin with, antenna position vectors are updated as

$$\mathbf{A}_q^R(t + \Delta t) = \mathbf{A}_q^R(t) + \mathbf{v}^R \Delta t \quad (6.28)$$

$$\mathbf{A}_p^T(t + \Delta t) = \mathbf{A}_p^T(t) + \mathbf{v}^T \Delta t. \quad (6.29)$$

At the same time, distance vectors of clusters need to be adjusted as

$$\mathbf{D}_n^R(t + \Delta t) = \mathbf{D}_n^R(t) + \mathbf{v}_n^R \Delta t \quad (6.30)$$

$$\mathbf{D}_n^T(t + \Delta t) = \mathbf{D}_n^T(t) + \mathbf{v}_n^T \Delta t. \quad (6.31)$$

Other distance vectors in (6.4)–(6.10) can be updated accordingly. Delay is updated as

$$\tau_n(t + \Delta t) = [\|\mathbf{D}_n^R(t + \Delta t)\| + \|\mathbf{D}_n^T(t + \Delta t)\|] / c + \tilde{\tau}_n(t + \Delta t). \quad (6.32)$$

The random virtual delay $\tilde{\tau}_n(t + \Delta t)$ is modeled as $\tilde{\tau}_n(t + \Delta t) = e^{-\frac{\Delta t}{\varsigma}} \tilde{\tau}_n(t) + (1 - e^{-\frac{\Delta t}{\varsigma}})X$ where X is a random variable independent to $\tilde{\tau}_n$ but identically distributed as $\tilde{\tau}_n$ and ς is a scenario-dependent parameter describing the coherence of virtual links. Thus, the updated delay will carry information of the delay in the previous time instant.

Another important aspect is the evolution of cluster mean power. Constant cluster mean powers were assumed in [42] and [51], which were not sufficient to characterise time evolution of the channel. Therefore, in this chapter, with the assumption that the cluster mean powers satisfy the inverse square law, the time evolution of cluster mean power can be expressed as (Derivations in Appendix B)

$$\tilde{P}_{n,m_n}(t + \Delta t) = \tilde{P}_{n,m_n}(t) \frac{3\tau_n(t) - 2\tau_n(t + \Delta t) + \tau_{m_n}}{\tau_n(t) + \tau_{m_n}}. \quad (6.33)$$

The mean power terms \tilde{P}_{n,m_n} in the mean power evolution in (6.33) are not normalised. They need to be normalised such that $P_{n,m_n} = \tilde{P}_{n,m_n} / \sum_{n,m_n} \tilde{P}_{n,m_n}$ before being plugged into (6.16).

6.2.5 Adaptation to scenarios

The proposed unified 5G GBSM framework can easily be adapted to support various scenarios by adjusting certain parameters of the channel model.

1. By setting the numbers of antennas (M_R and M_T) as relative small numbers, the wavefronts will automatically be approximated by plane wavefronts. Also, the cluster evolution on the array axis will become insignificant. In this case,

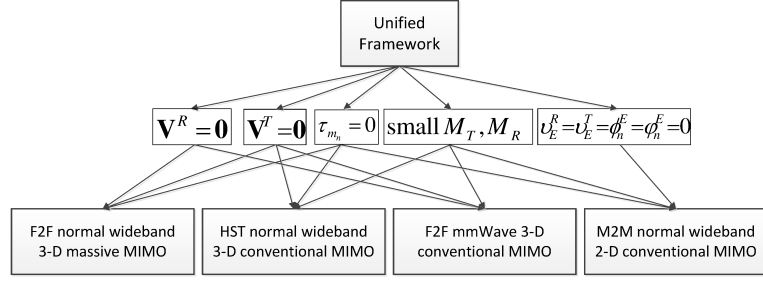


FIGURE 6.4: Diagram of combinations of scenarios from the proposed unified 5G GBSM framework.

the unified 5G GBSM framework is reduced to a conventional MIMO channel model.

2. By setting the velocity of the transmitter $\mathbf{v}^T = \mathbf{0}$, the transmitter will be static. As a result, a Fixed-to-Mobile (F2M) MIMO channel model can be obtained. In the same way, a Fixed-to-Fixed (F2F) MIMO channel model can be formed by setting both the transmitter and receiver static, i.e., $\mathbf{v}^T = \mathbf{v}^R = \mathbf{0}$.
3. By setting the relative delays of rays as 0, i.e., $\tau_{m_n} = 0$, rays within a cluster will become irresolvable. Consequently, the mmWave MIMO channel model is simplified as a normal wideband MIMO channel model.
4. By setting all elevation angles as zeros, i.e., $v_E^R(t) = v_E^T(t) = \phi_n^E(t) = \varphi_n^E(t) = 0$, the impacts of elevation angles are ignored. Then, a 2-D MIMO channel model can be achieved.

Combinations of scenarios can be obtained by properly adjusting these settings. Channel models for F2F normal wideband 3-D massive MIMO, HST normal wideband 3-D conventional MIMO, F2F mmWave 3-D conventional MIMO, and M2M normal wideband 2-D conventional MIMO are shown in Fig. 6.4 as examples.

6.3 Statistical Property Analysis

6.3.1 Time-variant PDP

The time-variant Power Delay Profile (PDP) $\Lambda(t, \tau)$ of the channel can be expressed as [34]

$$\Lambda(t, \tau) = \sum_n^{N(t)} \sum_{m_n}^{M_n} P_{n,m_n}(t) \delta(\tau - \tau_n(t) - \tau_{m_n}). \quad (6.34)$$

The time-variant properties of PDP are caused by the time-dependent mean powers and delays of rays. These are related to the geometrical relationship updates of the scattering environment.

6.3.2 Stationary interval

The stationary interval is utilised in [2] to measure for the estimated period within which the channel can be regarded as stationary. The definition of the stationary interval is the maximum time length within which the autocorrelation function of the PDP exceeds the 80% threshold [2]. It should be noticed that the 80% threshold in [2] is empirical and can be adjusted according to requirements. Also, the definition of stationary interval in [2] would fail to work if the autocorrelation function of the PDP is not monotonically decreasing or has multiple crossing points at the threshold. Therefore, it would be more accurate if the stationary interval is defined as the first point crossing the 80% threshold. An improved definition of the stationary interval $I(t)$ at time t is proposed as

$$I(t) = \inf \{ \Delta t | R_{\Lambda}(t, \Delta t) \leq 0.8 \} \quad (6.35)$$

where $\inf\{\cdot\}$ calculates the infimum of a function and $R_{\Lambda(t, \Delta t)}$ is the normalised autocorrelation function of the PDP defined by [2]

$$R_{\Lambda}(t, \Delta t) = \frac{\int \Lambda(t, \tau) \Lambda(t + \Delta t, \tau) d\tau}{\max \left\{ \int \Lambda(t, \tau) d\tau, \int \Lambda(t + \Delta t, \tau) d\tau \right\}}. \quad (6.36)$$

6.3.3 Time-variant transfer function

The time-variant transfer function $H_{qp}(\xi, t)$ is the Fourier transform of the channel impulse response with respect to delay, which can be expressed as [34]

$$\begin{aligned} H_{qp}(\xi, t) &= \int_{-\infty}^{\infty} h_{qp}(t, \tau) e^{-j2\pi\xi\tau} d\tau \\ &= \sqrt{\frac{K}{K+1}} h_{qp}^{\text{LOS}}(t) e^{-j2\pi\xi\tau^{\text{LOS}}(t)} + \sqrt{\frac{1}{K+1}} \sum_{n=1}^{N(t)} \sum_{m_n=1}^{M_n(t)} h_{qp,n,m_n}(t) e^{-j2\pi\xi[\tau_n(t) + \tau_{m_n}]} \end{aligned} \quad (6.37)$$

where ξ is frequency.

6.3.4 STFCE

To study the correlation properties, the Space-Time-Frequency Correlation Function (STFCE) $\rho_{qp,q'p'}(\delta_T, \delta_R, \Delta\xi, \Delta t; \xi, t)$ can be calculated as [34]

$$\rho_{qp,q'p'}(\delta_T, \delta_R, \Delta\xi, \Delta t; \xi, t) = \text{E} [H_{qp}^*(\xi, t) H_{q'p'}(\xi + \Delta\xi, t + \Delta t)]. \quad (6.38)$$

LOS and NLOS components are assumed uncorrelated for simplicity, (6.38) can be written as the sum of the correlation of the LOS component and the correlation of the NLOS components, i.e.,

$$\rho_{qp,q'p'}(\delta_T, \delta_R, \Delta\xi, \Delta t; \xi, t) = \rho_{qp,q'p'}^{\text{LOS}}(\delta_T, \delta_R, \Delta\xi, \Delta t; \xi, t) + \rho_{qp,q'p'}^{\text{NLOS}}(\delta_T, \delta_R, \Delta\xi, \Delta t; \xi, t). \quad (6.39)$$

The correlation of the LOS component is calculated as

$$\rho_{qp,q'p'}^{\text{LOS}}(\delta_T, \delta_R, \Delta\xi, \Delta t; \xi, t) = \frac{K}{K+1} h_{qp}^{\text{LOS}*}(t) h_{q'p'}^{\text{LOS}}(t + \Delta t) e^{j2\pi\sigma_1} \quad (6.40)$$

with $\sigma_1 = \xi [\tau^{\text{LOS}}(t) - \tau^{\text{LOS}}(t + \Delta t)] + \Delta\xi \tau^{\text{LOS}}(t + \Delta t)$. Similarly, the correlation of the NLOS components is calculated as

$$\begin{aligned} \rho_{qp,q'p'}^{\text{NLOS}}(\delta_T, \delta_R, \Delta\xi, \Delta t; \xi, t) &= \frac{1}{K+1} \times \\ \text{E} \left[\sum_{n=1}^{N(t)} \sum_{n'=1}^{N(t+\Delta t)} \sum_{m_n=1}^{M_n} \sum_{m_{n'}=1}^{M_{n'}} h_{qp,n,m_n}^*(t) h_{q'p',n',m_{n'}}(t + \Delta t) e^{j2\pi\sigma_2} \right] \end{aligned} \quad (6.41)$$

with $\sigma_2 = \xi(\tau_n(t) + \tau_{m_n} - \tau_{n'}(t + \Delta t) - \tau_{m_{n'}}) - \Delta\xi(\tau_{n'}(t + \Delta t) + \tau_{m_{n'}})$. Because cluster evolution is considered in the unified 5G GBSM framework, the mean number of survived cluster shared by $h_{qp,n,m_n}(t)$ and $h_{q'p',n',m_{n'}}(t + \Delta t)$ can be calculated as

$$\text{E} \left\{ \text{card} \left(S_{qp}(t) \cap S_{q'p'}(t + \Delta t) \right) \right\} = P_{\text{survival}} \text{E} \left\{ \text{card} (S_{qp}(t)) \right\} \quad (6.42)$$

where P_{survival} is the cluster survival probability when a cluster evolves from Ant_p^T , Ant_q^R , and t to $\text{Ant}_{p'}^T$, $\text{Ant}_{q'}^R$, and $t + \Delta t$, i.e.,

$$P_{\text{survival}} = e^{-\lambda_R \left[\frac{|q-q'|\delta_R + |p-p'|\delta_T}{D_c^2} + \frac{P_F(\Delta v^R + \Delta v^T)\Delta t}{D_c^2} \right]}. \quad (6.43)$$

Those newly generated clusters from $h_{qp,n,m_n}(t)$ to $h_{q'p',n',m_{n'}}(t + \Delta t)$ are independent to the survived clusters. Therefore, they do not contribute to the correlation coefficient. Then, the STFCF for NLOS components in (6.41) reduces to

$$\begin{aligned} \rho_{qp,q'p'}^{\text{NLOS}}(\delta_T, \delta_R, \Delta\xi, \Delta t; \xi, t) &= \frac{P_{\text{survival}}}{K+1} \times \\ \text{E} \left[\sum_{n=1}^{N(t)} \sum_{n'=1}^{N(t)} \sum_{m_n=1}^{M_n} \sum_{m_{n'}=1}^{M_{n'}} h_{qp,n,m_n}^*(t) h_{q'p',n',m_{n'}}(t + \Delta t) e^{j2\pi\sigma_2} \right]. \end{aligned} \quad (6.44)$$

As the dimension of the STFCF is high, it is difficult to present the STFCF visually. However, by setting $\Delta t = 0$, $\Delta\xi = 0$, and $q = q'$ ($p = p'$), the STFCF is reduced to

the receive (transmit) space Cross-Correlation Function (CCF). Similarly, by setting $q = q'$, $p = p'$, and $\Delta t = 0$, the STFCF is reduced to the time-variant Frequency Correlation Function (FCF).

6.4 Results and Analysis

In the simulation of the channel, we assumed that the generation rate λ_G and the recombination rate λ_R are set as $\lambda_G = 80/\text{m}$ [100] and $\lambda_R = 4/\text{m}$ to fix the mean number of clusters as 20 [30]. The percentage of moving clusters is $P_F = 0.3$ [100]. The estimated cluster parameters are listed in Table 6.3. Their distributions can be referred to Table 6.2. Estimation of cluster parameters is based on the minimum mean squared error (MMSE) criterion. One parameter is estimated via the MMSE criterion while keeping other parameters fixed. The procedure is performed on every parameter. All parameters can be modified subject to measurements.

TABLE 6.3: Simulation parameters for different scenarios.

F2F normal wideband 3-D massive MIMO			HST normal wideband 3-D conventional MIMO		
Parameters	Mean	Standard deviation	Parameters	Mean	Standard deviation
M_n	20	0	M_n	20	0
τ_n	930 ns	930 ns	τ_n	930 ns	930 ns
τ_{m_n}	0 ns	0 ns	τ_{m_n}	0 ns	0 ns
D_n^T	30 m	20 m	D_n^T	30 m	20 m
D_n^R	25 m	15 m	D_n^R	25 m	15 m
ϕ_n^A	0.78 rad	1.15 rad	ϕ_n^A	0.78 rad	0.90 rad
ϕ_n^E	0.78 rad	0.18 rad	ϕ_n^E	0.78 rad	0.18 rad
φ_n^A	1.05 rad	0.54 rad	φ_n^A	1.05 rad	0.54 rad
φ_n^E	0.78 rad	0.11 rad	φ_n^E	0.78 rad	0.11 rad
M2M normal wideband 2-D conventional MIMO			F2F mmWave 3-D conventional MIMO		
Parameters	Mean	Standard deviation	Parameters	Mean	Standard deviation
M_n	20	0	M_n	15	3.87
τ_n	930 ns	930 ns	τ_n	305 ns	305 ns
τ_{m_n}	0 ns	0 ns	τ_{m_n}	3 ns	3 ns
D_n^T	30 m	20 m	D_n^T	5 m	3 m
D_n^R	25 m	15 m	D_n^R	5 m	3 m
ϕ_n^A	0.78 rad	0.91 rad	ϕ_n^A	0.78 rad	0.91 rad
ϕ_n^E	0 rad	0 rad	ϕ_n^E	0.78 rad	0.18 rad
φ_n^A	1.04 rad	0.53 rad	φ_n^A	1.04 rad	0.53 rad
φ_n^E	0 rad	0 rad	φ_n^E	0.78 rad	0.11 rad

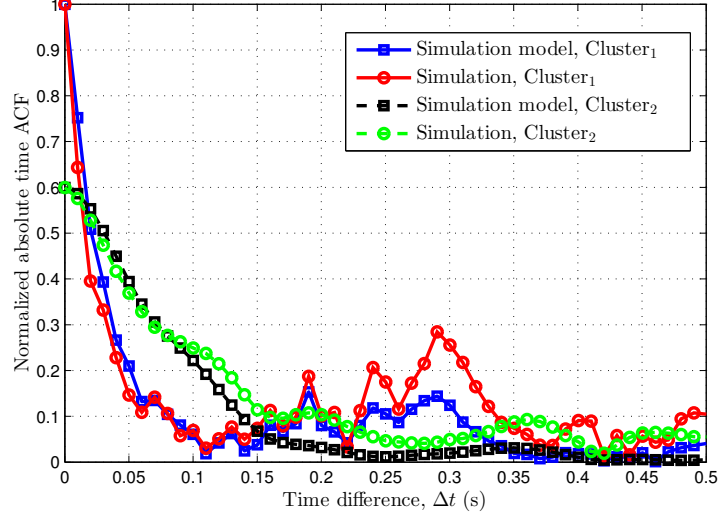


FIGURE 6.5: Comparison between the normalised ACFs of Cluster₁ and Cluster₂ of the normal wideband conventional MIMO channel model ($f_c = 2\text{GHz}$, $\|\mathbf{D}\| = 200\text{m}$, $M_R = M_T = 2$, $\delta_R = \delta_T = 0.5\lambda$, $\Delta v^R = \Delta v^T = 0\text{m/s}$, $|\mathbf{v}^T| = 0, |\mathbf{v}^R| = 5\text{m/s}$, $v_E^T = \frac{\pi}{6}$, $v_A^T = \frac{\pi}{3}$, $v_E^R = v_A^R = \frac{\pi}{4}$, $D_c^a = 50\text{m}$, $M_1 = M_2 = 81$, $\varsigma = 7\text{s}$, NLOS).

To validate the correctness of the proposed unified 5G GBSM framework, the Auto-correlation Functions (ACFs) of the simulation model and simulation of the normal wideband conventional MIMO channel model are compared in Fig. 6.5. It should be noted that these ACFs are normalised with respect to Cluster₁. It can be seen from Fig. 6.5 that the simulated ACFs well align with the ACFs of the simulation model for both Cluster₁ and Cluster₂.

The receiver normalised space CCFs of the F2F normal wideband 3-D massive MIMO channel model are shown in Fig. 6.6. The correlation coefficients drop to a relatively low level when the antenna index difference is larger than 2. In addition, comparison between the space CCF of the channel model and measured space CCF in [1, Fig. 10] is provided. Although the proposed channel model slightly overestimates correlation at the tail, the space CCF of the channel model aligns well with the measured data when the antenna index difference is less than 3.

The Complementary Cumulative Distribution Function (CCDF) of the stationary interval of the HST normal wideband 3-D conventional MIMO channel model is shown in Fig. 6.7. The median of the stationary interval is approximately 40 ms. Meanwhile,

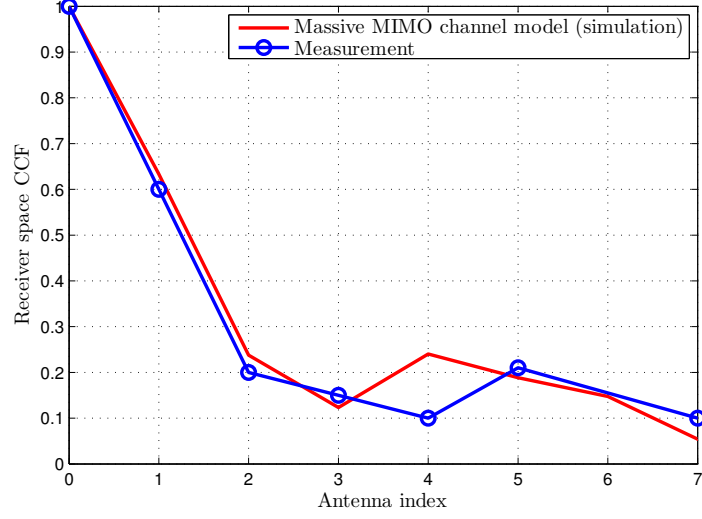


FIGURE 6.6: Receiver normalised space CCFs of F2F normal wideband 3-D massive MIMO channel model and measurement in [1] ($f_c = 2.6\text{GHz}$, $\|\mathbf{D}\| = 200\text{m}$, $M_R = M_T = 32$, $\delta_R = \delta_T = 0.5\lambda$, $\Delta v^R = \Delta v^T = 0\text{m/s}$, $|\mathbf{v}^T| = |\mathbf{v}^R| = 0$, $v_E^T = \frac{\pi}{4}$, $v_A^T = \frac{\pi}{3}$, $v_E^R = v_A^R = \frac{\pi}{4}$, $D_c^a = 30\text{m}$, $\kappa = -8\text{dB}$, polarised antennas, NLOS).

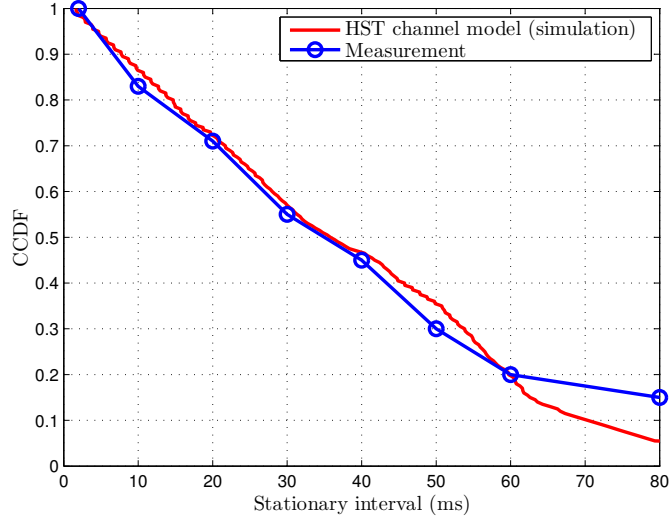


FIGURE 6.7: CCDFs of the HST normal wideband 3-D conventional MIMO channel model and measurement in [2] ($f_c = 932\text{MHz}$, $\|\mathbf{D}\| = 200\text{m}$, $M_R = M_T = 2$, $\Delta v^R = \Delta v^T = 0.5\text{m/s}$, $\|\mathbf{v}^R\| = 60\text{m/s}$, $\|\mathbf{v}^T\| = 0\text{m/s}$, $v_E^T = \frac{\pi}{4}$, $v_A^T = \frac{\pi}{3}$, $v_E^R = v_A^R = \frac{\pi}{4}$, $D_c^a = 100\text{m}$, $\varsigma = 7\text{s}$).

results of the proposed HST channel model are validated by measurements in [2, Fig. 4(a)].

The 90% coherence bandwidth measures the bandwidth in which the channel can be regarded as flat. The Cumulative Distribution Function (CDF) of 90% coherence

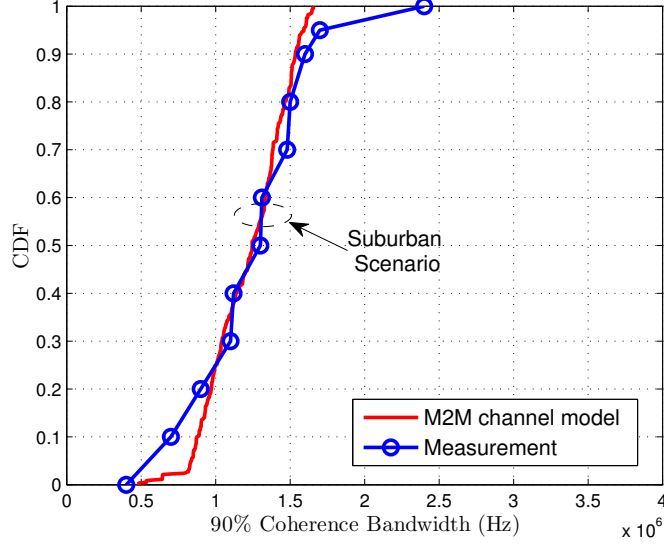


FIGURE 6.8: CDF of 90% coherence bandwidth of the M2M normal wideband 2-D conventional MIMO channel model and measurement (suburban scenario) in [3] ($f_c = 5.9\text{GHz}$, $\|\mathbf{D}\| = 400\text{m}$, $\Delta v^R = \Delta v^T = 0.5\text{m/s}$, $\|\mathbf{v}^T\| = \|\mathbf{v}^R\| = 25\text{m/s}$, $v_A^R = v_E^R = \frac{\pi}{4}$, $v_A^T = \frac{\pi}{3}$, $v_E^R = \frac{\pi}{4}$, $D_c^s = 10\text{m}$, $\varsigma = 5\text{s}$).

bandwidth of the M2M normal wideband 2-D conventional MIMO channel model is illustrated in Fig. 6.8, which is also validated by that of the measured suburban M2M channel in [3, Fig. 5(a)].

A snapshot of normalized Angular Power Spectrum (APS) at the receiver of a mmWave massive MIMO channel is illustrated in Fig. 6.9. The APS is estimated with the Multiple Signal Classification (MUSIC) algorithm [119], [120] using a sliding window of 3 consecutive antennas. It can be observed that the number of clusters is small because of the high carrier frequency of mmWave. Meanwhile, appearance and disappearance of clusters on the array axis can also be seen due to the massive MIMO antenna array.

Fig. 6.10 presents the CCDFs of the Root Mean Squared (RMS) delay spread of the mmWave channel model. The RMS spread of the mmWave channel model is in the order of 10ns. Scenario 1 and Scenario 2 are the Room H scenario and Room F scenario in [4, Fig. 5], respectively. Measurement results for different scenarios in [4, Fig. 5] can be fitted properly by the proposed mmWave channel model.

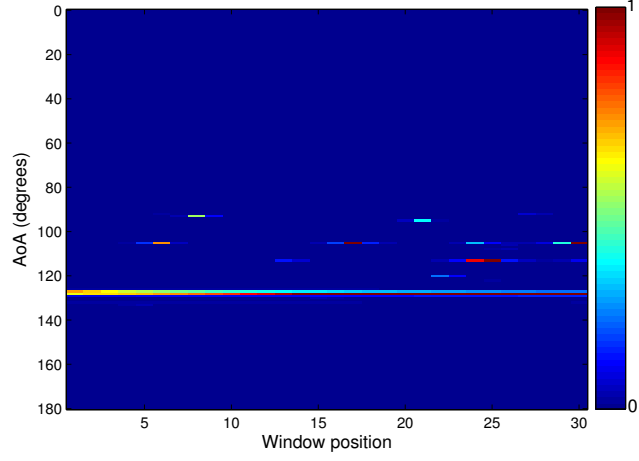


FIGURE 6.9: A snapshot of simulated normalized APS at the receiver of the mmWave 2-D massive MIMO channel model ($f_c = 58\text{GHz}$, $M_T = 2$, $M_R = 32$, $\|\mathbf{D}\| = 6\text{m}$, $\delta_R = \delta_T = 0.5\lambda$, $\Delta v^R = \Delta v^T = 0\text{m/s}$, $|\mathbf{v}^T| = |\mathbf{v}^R| = 0$, $v_E^T = \frac{\pi}{4}$, $v_A^T = \frac{\pi}{3}$, $v_E^R = v_A^R = 0$, $D_c^a = 30\text{m}$, $D_c^s = 100\text{m}$, NLOS).

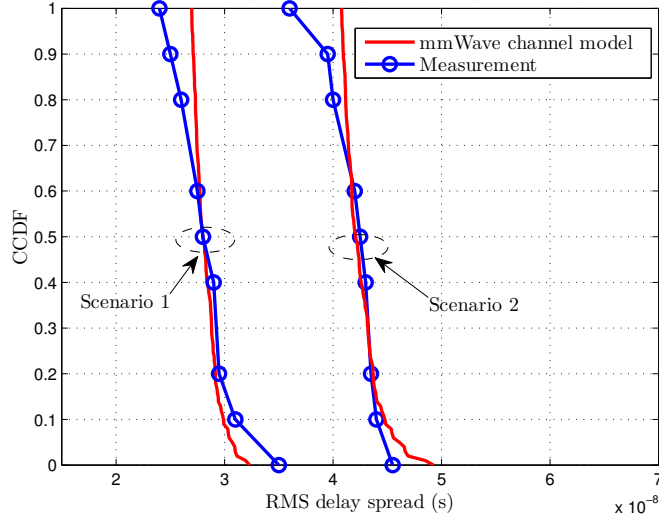


FIGURE 6.10: CCDFs of RMS delay spread of the F2F mmWave 3-D conventional MIMO channel model and measurement in [4] ($f_c = 58\text{GHz}$, $\|\mathbf{D}\| = 6\text{m}$, $\Delta v^R = \Delta v^T = 0\text{m/s}$, $\|\mathbf{v}^T\| = \|\mathbf{v}^R\| = 0\text{m/s}$, $v_A^R = v_E^R = \frac{\pi}{4}$, $v_A^T = \frac{\pi}{3}$, $v_E^T = \frac{\pi}{4}$, $D_c^s = 100\text{m}$, $\varsigma = 7\text{s}$).

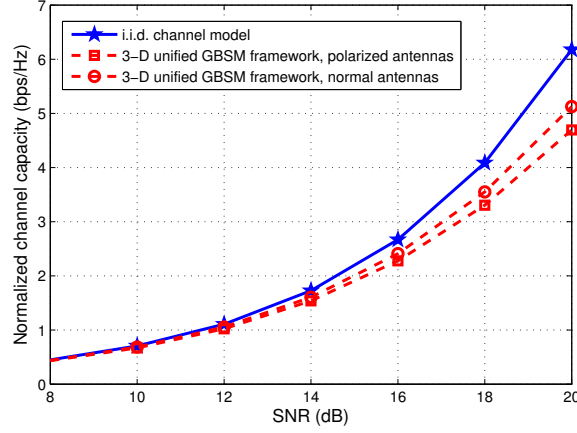


FIGURE 6.11: Comparison of normalized channel capacities of the unified GBSM framework for massive MIMO channel models with normal and polarized antennas ($M_R = 8$, $M_T = 32$, $f_c = 2\text{GHz}$, $\|\mathbf{D}\| = 100\text{m}$, $v_A^R = \frac{\pi}{4}$, $v_A^T = \frac{\pi}{3}$, $D_c^s = 100\text{m}$, $\varsigma = 7\text{s}$, $v_E^R = \frac{\pi}{4}$, $v_E^T = \frac{\pi}{4}$, $\kappa = -8\text{dB}$).

Channel capacities of the unified GBSM framework with normal and polarized antennas are shown in Fig. 6.11. The channel capacity with polarized antennas is lower than that with normal antennas. However, the dimensions of antenna arrays are halved because of the use of polarized antennas.

Fig. 6.12 depicts the channel capacities of the i.i.d. massive MIMO channel model, the 2-D ellipse massive MIMO channel model, the 3-D twin-cluster massive MIMO channel model, the reduced 2-D twin-cluster massive MIMO channel model, the KBSM–BD–AA with isotropic scattering environment, the 3-D unified GBSM framework, and the reduced 2-D unified GBSM framework. The channel capacities of these channel models are computed using the capacity of frequency selective MIMO channels in [13]. The channel capacities of those three GBSMs slightly vary with elevation angles considered. The i.i.d. channel capacity serves as the upper bound of channel capacities while the capacity of the KBSM–BD–AA with isotropic scattering environment lies between the i.i.d. channel capacity and the capacities of GBSMs.

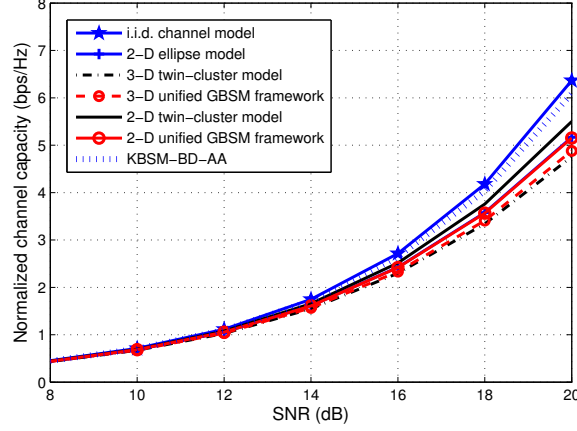


FIGURE 6.12: Comparison of normalized channel capacities of massive MIMO channel models ($M_R = 8$, $M_T = 32$, $f_c = 2\text{GHz}$, $\|\mathbf{D}\| = 100\text{m}$, $v_A^R = \frac{\pi}{4}$, $v_A^T = \frac{\pi}{3}$, $D_c^s = 100\text{m}$, $\varsigma = 7\text{s}$, $v_E^R = \frac{\pi}{4}$ (3-D models only), $v_E^T = \frac{\pi}{4}$ (3-D models only)).

6.5 Summary

In this chapter, a unified framework for 5G channel models has been proposed. The WINNER II and SV channel model have been combined in the unified framework. The proposed unified 5G GBSM framework can be adapted to various scenarios by properly setting certain parameters. Simulated statistical properties of the proposed unified 5G GBSM framework have been compared with measurements. In addition, 3-D features and polarised directional antennas are included. Another important issue is the modelling of time evolution of the channel, which includes cluster evolution on the time axis, geometrical relationship updates, and evolution of delays and powers of rays. For future work, applications of the proposed channel model to 5G system simulators need to be considered. Also, cooperative MIMO channel model with multi-link correlation and parameters for HST channel model in tunnel scenarios are potential directions.

Chapter 7

Conclusions and Future Work

This thesis has presented a wealth of comprehensive research on wireless channel modelling and simulation for massive MIMO communication systems (i.e., GBSMs in Chapter 3 and Chapter 4, KBSM in Chapter 5, and a unified framework for 5G channels in Chapter 6). The importance of our research has been proved and introduced in detail. In this concluding chapter, the key findings of my PhD research are summarised and several potential future research directions are proposed as well.

7.1 Summary of Results

7.1.1 GBSMs for massive MIMO channels

In Chapter 3, a novel non-stationary wideband multi-confocal ellipse 2-D GBSM for massive MIMO channels has been proposed. Spherical wavefront has been assumed in the proposed model to characterise the nearfield effect caused by the increase in the number of antennas. It has been demonstrated that WSS properties are not available under the spherical wavefront assumption. In addition, the BD process has been used in the proposed model to capture the array-time evolution of clusters. Statistical properties of the channel model such as the STFCF, space CCF, APS, average life periods of clusters on the array axis, time ACF, FCF, and power imbalance on the

antenna array have been studied. The impact of the spherical wavefront assumption on the statistical properties of the channel model has been investigated. Furthermore, numerical analysis has shown that the proposed channel model is able to capture specific characteristics of massive MIMO channel as observed in measurements.

In Chapter 4, we have proposed a novel non-stationary 3-D wideband twin-cluster channel model along with the corresponding simulation model for massive MIMO systems with carrier frequencies in the order of GHz. Nearfield effects instead of farfield effects have been considered in the proposed model. These include the spherical wavefront assumption and a BD process to model non-stationary properties of clusters such as cluster appearance and disappearance on both the array and time axes, AoA shifts, received power variations, and Doppler frequency variations on the antenna array. The impact of elevation angles of clusters on space CCF, time ACF of the massive MIMO channel model has been studied. Additionally, the Doppler PSD, standard deviation of Doppler frequencies on the large array, APS, and condition number of the channel have been investigated. Moreover, it has been shown that the channel characteristics of the simulation model are consistent with those of the theoretical model.

7.1.2 KBSM for massive MIMO channels

In Chapter 5, we have proposed a novel KBSM–BD–AA for massive MIMO channels. The evolution of scatterer sets on the array axis has been abstracted by a survival probability matrix based on the BD process. With this consideration, the overall antenna correlation matrix is equivalent to the Hadamard product of the spatial correlation matrix and the survival probability matrix. Upper and lower bounds of channel capacities have been analysed in both the high and low SNR regimes when the numbers of transmit and receive antennas are increasing unboundedly with a constant ratio. The evolution of scatterer sets on the array axis has been shown to decrease spatial correlations of KBSM channels.

7.1.3 A unified framework for 5G channel models

In Chapter 6, a unified framework for 5G channel models has been proposed. The proposed unified 5G GBSM framework can be adapted to various scenarios by properly setting certain parameters, such as massive MIMO systems, HST communications, M2M communications, and mmWave communications. The proposed 5G channel model framework is a 3-D non-stationary channel model based on the WINNER II and SV channel models considering array-time cluster evolution. In addition, 3-D features and polarised directional antennas have been included. Another important issue is the modelling of time evolution of the channel, which includes cluster evolution on the time axis, geometrical relationship updates, and evolution of delays and powers of rays. Statistical properties of the proposed 5G channel model such as time ACF, space CCF, APS, CCDF of stationary intervals, CDF of 90% coherence bandwidth, and CCDF of RMS delay have been investigated to demonstrate its capability of capturing channel characteristics of various scenarios, with excellent fitting to certain corresponding measurements.

7.2 Future Research Directions

There are several potential directions of this thesis that can be further expanded.

7.2.1 COST 2100 model for massive MIMO channels

The COST 2100 channel model, a cluster-based GBSM, introduced Visibility Regions (VRs) to model the spatially-variant nature of massive MIMO channels, i.e., cluster appearance and disappearance on the array axis [53]. A VR is a region in space corresponding to a cluster. A cluster is observable to an antenna element if this antenna element lies within the VR of the cluster. Different antenna elements on a large array may lie within various VRs. Then, each antenna element may observe its own set of clusters.

The modelling of spatial variance via VRs in the COST 2100 channel model is fundamentally different from the method based on BD processes introduced in the twin-cluster and ellipse channel models in [42], [51], [113]. The COST 2100 channel model is able to jointly model time and array evolutions with VRs. Also, it was reported in [53] that parameters of VRs could be estimated based on measured data. For modelling massive MIMO effects at the transmitter and receiver, visibility regions can be applied to both the BS and UE.

However, the current assumption of a VR is a circular region on the azimuth plane in [31]–[33], [53]. This may fail to model the 3-D scattering environment, especially when the transmitter or receiver moves vertically or vertical beamforming for skyscraper scenario is considered. A potential solution for this is to generalise circular region of a VR to a sphere in a 3-D space. Meanwhile, the complexity of the COST 2100 channel modelling for massive MIMO is still under investigation.

7.2.2 Map-based massive MIMO channels

Besides the GBSM discussed in Chapter 3, Chapter 4, and Chapter 6, the METIS project proposed a novel modelling method for massive MIMO channels named as the Map-Based Channel Model (MBCM) [47]. The METIS MBCM was established based on ray tracing techniques. It aimed at tracking each ray from the transmitter to the receiver. Interactions between rays and shadowing/scattering objects such as diffraction, specular reflection, diffuse scattering, and blocking were considered. These shadowing/scattering objects can be randomly generated in the environment or obtained from a specific scenario.

Since each ray is tracked by the MBCM, massive MIMO channel characteristics such as spherical wavefront and non-stationary properties of clusters are included in the model. Additionally, having considered Doppler frequencies at both the transmitter and receiver sides, the METIS MBCM is able to support scenarios where M2M communications with massive MIMO. However, the ray tracing nature of the MBCM results in high complexity [47]. The practicality of MBCM is to be justified.

7.2.3 Correlation-based massive MIMO channel model

The adaptation of BD to KBSMs can be achieved without extra complexity, because antenna spatial correlation matrices for KBSMs can be separated easily. However, The adaptation of BD to Weichselberger or VCR requires further investigations, which will be an interesting research direction in the future. Further, general CBSM [124] with extension of BD process on the array axis for massive MIMO channel modelling may be developed.

7.2.4 Standardised 5G channel model

As standardised 5G channel models are still missing in the literature, attentions should be paid to the development of standardised models. To achieve this goal, a model capturing key characteristics of massive MIMO and mmWave channels with reasonable complexity needs to be considered. The unified framework for 5G wireless channels in Chapter 6 can be used as a starting point. Additionally, large-scale fading, i.e., pathloss and shadow fading for massive MIMO should be included in the standardised massive MIMO channel model. Moreover, other scenarios such as cooperative communications and HST communications in tunnels should be considered as well.

Appendix A

Antenna Pattern Calculation

In a 3-D space, the geometry of antenna pattern depends on the orientation of antennas. A LCS is constructed along the horizontal polarization, vertical polarization, and antenna broadside as Fig. A.1 shows. The LCS is obtained by a sequence of rotations from the GCS [145]. First, a rotation of α^T about x_G axis is operated. Second, a rotation of β^T about the new y_G axis is operated. Third, a rotation of γ^T about the new z_G axis is operated. These three operations can be expressed as [145]

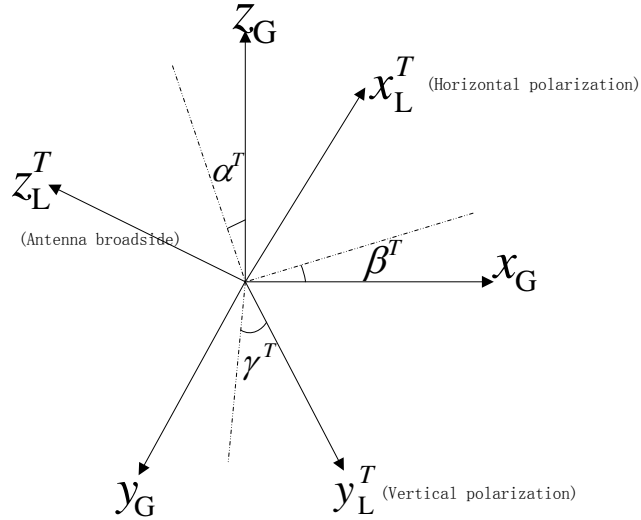


FIGURE A.1: Diagram of LCS and GCS in the 3-D space.

$$\mathbf{R} = \begin{bmatrix} \cos \gamma^T & -\sin \gamma^T & 0 \\ \sin \gamma^T & \cos \gamma^T & 0 \\ 0 & 0 & 1 \end{bmatrix} \begin{bmatrix} \cos \beta^T & 0 & \sin \beta^T \\ 0 & 1 & 0 \\ -\sin \beta^T & 0 & \cos \beta^T \end{bmatrix} \begin{bmatrix} 1 & 0 & 0 \\ 0 & \cos \alpha^T & -\sin \alpha^T \\ 0 & \sin \alpha^T & \cos \alpha^T \end{bmatrix}. \quad (\text{A.1})$$

Let \mathbf{a} and \mathbf{b} be positions vectors in the GCS, and let $(\tilde{x}, \tilde{y}, \tilde{z})^T$ be the coordinates of $\mathbf{a} - \mathbf{b}$ in the LCS. Then, $(\tilde{x}, \tilde{y}, \tilde{z})^T = \mathbf{R}(\mathbf{a} - \mathbf{b})$. Let $w(x, y)$ be the four-quadrant inverse tangent function [146] of x and y , and let $\tilde{\theta} = w(\tilde{y}, \tilde{x})$ and $\tilde{\phi} = w(\tilde{z}, \sqrt{\tilde{x}^2 + \tilde{y}^2})$. Then, the antenna patterns can be computed as $F_H(\mathbf{a}, \mathbf{b}) = G(\tilde{\theta}, \tilde{\phi}) \cos \tilde{\theta}$ and $F_V(\mathbf{a}, \mathbf{b}) = G(\tilde{\theta}, \tilde{\phi}) \sin \tilde{\theta}$. In Chapter 6, dipole antennas are assumed at the transmitter side. In this case [147],

$$G(\tilde{\theta}, \tilde{\phi}) = \sqrt{1.64} \frac{\cos\left(\frac{\pi}{2} \cos \tilde{\phi}\right)}{\sin \tilde{\phi}}. \quad (\text{A.2})$$

At the receiver side, calculation follows a similar procedure. Omnidirectional antennas are assumed at the receiver side. In this case, $G(\tilde{\theta}, \tilde{\phi}) = 1$. The rotation angles α^T , α^R , β^T , β^R , γ^T , and γ^R are all set as $\frac{\pi}{15}$ for simplicity, which can be modified according to realistic settings.

Appendix B

Time Evolution of Ray Mean Powers

Let us consider the time interval between t and $t + \Delta t$, where Δt is small. Then, the cluster mean power difference $\Delta \tilde{P}_{n,m_n}(t)$ between these two time instants is computed as

$$\Delta \tilde{P}_{n,m_n}(t) = \tilde{P}_{n,m_n}(t + \Delta t) - \tilde{P}_{n,m_n}(t). \quad (\text{B.1})$$

With the assumption of the inverse power law, the cluster mean power is inversely proportional to the η th ($\eta > 1$) power of travel distance, i.e.,

$$\tilde{P}_{n,m_n}(t) = \frac{\mathcal{C}}{[\tau_n(t) + \tau_{n,m_n}]^\eta c^\eta} \quad (\text{B.2})$$

where \mathcal{C} is a constant. The derivative of $\tilde{P}_{n,m_n}(t)$ with respect to t is obtained by

$$\begin{aligned} \frac{\Delta \tilde{P}_{n,m_n}(t)}{\Delta t} &= \left(\frac{\mathcal{C}}{[\tau_n(t) + \tau_{n,m_n}]^\eta c^\eta} \right)' = -\eta \frac{\mathcal{C}}{[\tau_n(t) + \tau_{n,m_n}]^{\eta+1} c^\eta} (\tau_n(t))' \\ &= -\eta \frac{\mathcal{C}}{[\tau_n(t) + \tau_{n,m_n}]^{\eta+1} c^\eta} \frac{[\tau_n(t + \Delta t) - \tau_n(t)]}{\Delta t}. \end{aligned} \quad (\text{B.3})$$

Thus, the cluster mean power evolution in terms of time can be derived as

$$\frac{\Delta \tilde{P}_{n,m_n}(t)}{\tilde{P}_{n,m_n}(t)} = \frac{-\eta}{\tau_n(t) + \tau_{n,m_n}} \frac{[\tau_n(t + \Delta t) - \tau_n(t)]}{\Delta t} \Delta t. \quad (\text{B.4})$$

Re-ordering the above equation, the update formula is

$$\tilde{P}_{n,m_n}(t + \Delta t) = \tilde{P}_{n,m_n}(t) \frac{(\eta + 1)\tau_n(t) - \eta\tau_n(t + \Delta t) + \tau_{n,m_n}}{\tau_n(t) + \tau_{n,m_n}}. \quad (\text{B.5})$$

With the assumption of the inverse square law ($\eta = 2$), (6.33) is obtained.

References

- [1] S. Payami and F. Tufvesson, “Channel measurements and analysis for very large array systems at 2.6GHz,” in *Proc. of the 6th European Conference on Antennas and Propagation*, Prague, Czech Republic, Mar. 2012.
- [2] C. Chen, Z. Zhong, and B. Ai, “Stationarity intervals of time-variant channel in high speed railway scenario,” *J. China Commun.*, vol. 9, no. 8, pp. 64–70, Aug. 2012.
- [3] L. Cheng, B. Henty, R. Cooper, D. D. Stancil, and F. Bai, “Multi-path propagation measurements for vehicular networks at 5.9 GHz,” in *Proc. WCNC’08.*, Las Vegas, US, Apr. 2008, pp. 1239–1244.
- [4] P. F. M. Smulders and A. G. Wagemans, “Frequency-domain measurement of the millimeter wave indoor radio channel,” *IEEE Trans. Instrum. Meas.*, vol. 44, no. 6, pp. 1017–1022, Dec. 1995.
- [5] Nokia Networks. Looking ahead to 5G. White Paper. Available:
http://networks.nokia.com/sites/default/files/document/5g-white-paper_0.pdf.
- [6] 5GNOW. 5G cellular communications scenarios and system requirements. White Paper. Available:
http://www.5gnow.eu/wp-content/uploads/2015/04/5GNOW_D2.1_v1.0_0.pdf.

- [7] METIS. Scenarios, requirements and KPIs for 5G mobile and wireless system. Available:
https://www.metis2020.com/wp-content/uploads/deliverables/METIS_D1.1_v1.pdf.
- [8] IMT-2020 Promotion Group. 5G visions and requirements. White Paper. Available:
http://euchina-ict.eu/wp-content/uploads/2015/03/IMT-20205GPG-WHITE-PAPER-ON-5G-VISION-AND-REQUIREMENTS_V1.0.pdf.
- [9] E. Dahlman, G. Mildh, S. Parkvall, J. Peisa, J. Sachs, and Y. Selen, “5G radio access,” *Ericsson Review*, vol. 6, pp. 1–7, 2014.
- [10] Samsung. 5G vision. White Paper. Available:
<http://www.samsung.com/global/business-images/insights/2015/Samsung-5G-Vision-0.pdf>.
- [11] Qualcomm. 1000x data challenge. White Paper. Available:
<https://www.qualcomm.com/invention/technologies/1000x>.
- [12] Huawei. 5G a technology vision. White Paper. Available:
<http://www.huawei.com/5gwhitepaper/>.
- [13] A. Paulraj, R. Nabar, and D. Gore, *Introduction to Space-Time Wireless Communications.*, Cambridge University Press, Cambridge, 2008.
- [14] IEEE 802.16 WG, *802.16m Evaluation methodology document*, 802.16m-08/004r5, Jan. 1999.
- [15] S. Sesia, I. Toufik, and M. Baker, *LTE–The UMTS Long Term Evolution: From Theory to Practice.*, 2nd ed., John Wiley & Sons, West Sussex, 2011.
- [16] G. J. Foschini and M. J. Gans, “On limits of wireless communications in a fading environment when using multiple antennas,” *Wireless Pers. Commun.*, vol. 6, no. 3, pp. 311–335, Mar. 1998.
- [17] D. Gesbert, M. Shafi, D. Shiu, P. J. Smith, and A. Naguib, “From theory to practice: an overview of MIMO space-time coded wireless systems,” *IEEE J. Sel. Areas Commun.*, vol. 21, no. 3, pp. 281–302, Apr. 2003.

- [18] G. J. Foschini, “Layered space-time architecture for wireless communication in a fading environment when using multielement antennas,” *Bell Labs Tech. J.*, pp. 41–59, Autumn 1996.
- [19] 3GPP T.S. 36.211, *Physical Channels and Modulation*, V12.1.0, 2014.
- [20] A. Chockalingam and B. Sundar Rajan, *Large MIMO Systems.*, Cambridge University Press, Cambridge, 2014.
- [21] D. Tse and P. Viswanath, *Fundamentals of Wireless Communication.*, Cambridge Univ. Press, Cambridge, UK, 2005.
- [22] E. G. Larsson, F. Tufvesson, O. Edfors, and T. L. Marzetta, “Massive MIMO for next generation wireless systems”, *IEEE Commun. Mag.*, vol.52, no. 2, pp.186–195, Feb. 2014.
- [23] F. Rusek, D. Persson, B. K. Lau, E. G. Larsson, T. L. Marzetta, O. Edfors, and F. Tufvesson, “Scaling up MIMO: opportunities and challenges with very large arrays,” *IEEE Signal Processing Mag.*, vol. 30, no. 1, pp. 40–60, Jan. 2012.
- [24] Z. Ma, Z. Q. Zhang, Z. G. Ding, P. Z. Fan, and H. C. Li, ”Key techniques for 5G wireless communications:network architecture, physical layer, and MAC layer perspectives,” *SCIENCE CHINA Information Sciences.*, vol. 58, pp. 1–20, Apr. 2015.
- [25] V. Jungnickel, K. Manolakis, W. Zirwas, B. Panzner, V. Braun, M. Lossow, M. Sternad, R. Apelfröjd, and T. Svensson, “The role of small cells, coordinated multipoint, and massive MIMO in 5G,” *IEEE Commun. Mag.*, vol. 52, no. 2, pp. 44–51, May 2014.
- [26] A. Osseiran, F. Boccardi, V. Braun, *et al.*, “Scenarios for 5G mobile and wireless communications: the vision of the METIS project,” *IEEE Commun. Mag.*, vol. 52, no. 5, pp. 26–35, May 2014.
- [27] C.-X. Wang, F. Haider, X. Gao, X.-H. You, Y. Yang, D. Yuan, H. Aggoune, H. Haas, S. Fletcher, and E. Hepsaydir, “Cellular architecture and key technologies

- for 5G wireless communication networks,” *IEEE Commun. Mag.*, vol. 52, no. 2, pp. 122–130, Feb. 2014.
- [28] B. N. Getu and J. B. Andersen, “The MIMO cube – a compact MIMO antenna,” *IEEE Trans. Wireless Commun.*, vol. 4, no. 3, pp. 1136–1141, May 2005.
- [29] A. L. Moustakas, H. U. Baranger, L. Balents, A. M. Sengupta, and S. H. Simon, “Communication through a diffusive medium: coherence and capacity,” *Science*, vol. 287, no. 5451, pp. 287–290, Jan. 2000.
- [30] P. Kyosti, *et al.*, “WINNER II channel model”, ver 1.1, Sept. 2007. Available: <http://www.ist-winner.org/WINNER2-Deliverables/D1.1.2v1.1.pdf>.
- [31] L. Liu, C. Oestges, J. Poutanen, K. Haneda, P. Vainikainen, F. Quitin, F. Tufvesson, and P. D. Doncker, “The COST 2100 MIMO channel model,” *IEEE Commun. Mag.*, vol. 19, no. 6, pp. 92–99, Dec. 2012.
- [32] M. F. Zhu, G. Eriksson, and F. Tufvesson, “The COST 2100 channel model: parameterization and validation based on outdoor MIMO measurements at 300 MHz,” *IEEE Trans. Wireless Commun.*, vol. 12, no. 2, pp. 888–897, Feb. 2013.
- [33] R. Verdone and A. Zanella, *Pervasive Mobile and Ambient Wireless Communications: COST Action 2100.*, Springer, London, 2012.
- [34] M. Patzold, *Mobile Radio Channels.*, 2nd ed., John Wiley & Sons, West Sussex, 2012.
- [35] A. J. Grant, “Performance analysis of transmit beamforming,” *IEEE Trans. Commun.*, vol. 53, no. 4, pp. 738–744, Apr. 2005.
- [36] A. M. Tulino and S. Verdú, *Random Matrix Theory and Wireless Communications.*, Foundations and Trends ® in Communications and Information Theory, vol. 1, no. 1, pp. 1–182, June 2004. doi: 10.1561/01000000001.
- [37] A. Lozano, A. M. Tulino, and S. Verdú, “Multiple-antenna capacity in the low-power regime,” *IEEE Trans. Inf. Theory*, vol. 49, no. 10, pp. 2527–2544, Oct. 2003.

- [38] A. G. Zajić and G. L. Stüber, “Space-time correlated mobile-to-mobile channels: modelling and simulation,” *IEEE Trans. Veh. Technol.*, vol. 57, no. 2, pp. 715–726, Mar. 2008.
- [39] M. Patzold, B. O. Hogstad, and N. Youssef, “Modeling, analysis, and simulation of MIMO mobile-to-mobile fading channels,” *IEEE Trans. Wireless. Commun.*, vol. 7, no. 2, pp. 510–520, Feb. 2008.
- [40] A. Ghazal, C.-X. Wang, B. Ai, D. Yuan, and H. Haas, “A non-stationary wideband MIMO channel model for high-mobility intelligent transportation systems,” *IEEE Trans. Intell. Transp. Syst.*, vol. 16, no. 2, pp. 885–897, Apr. 2015.
- [41] B. O. Hogstad, M. Patzold, and A. Chopra, “A study on the capacity of narrow- and wideband MIMO channel models,” in *Proc. IST’06*, Myconos, Greece, June 2006, pp. 1–6.
- [42] S. Wu, C. -X. Wang, H. Haas, el-H. M. Aggoune, M. M. Alwakeel, and B. Ai, “A non-stationary wideband channel model for Massive MIMO communication systems,” *IEEE Trans. Wireless Commun.*, vol. 14, no. 3, pp. 1434–1446, Mar. 2015.
- [43] X. Cheng, C. -X. Wang, D. I. Laurenson, S. Salous, and A. V. Vasilakos, “An adaptive geometry-based stochastic model for non-isotropic MIMO mobile-to-mobile channels,” *IEEE Trans. Wireless Commun.*, vol. 8, no. 9, pp. 4824–4835, Sep. 2009.
- [44] X. Cheng, C.-X. Wang, B. Ai, and H. Aggoune, “Envelope level crossing rate and average fade duration of non-isotropic vehicle-to-vehicle Ricean fading channels,” *IEEE Trans. Intell. Transp. Syst.*, vol. 15, no. 1, pp. 62–72, Feb. 2014.
- [45] X. Cheng, C.-X. Wang, H. Wang, X. Gao, X.-H. You, D. Yuan, B. Ai, Q. Huo, L. Song, and B. Jiao, “Cooperative MIMO channel modeling and multi-link spatial correlation properties,” *IEEE J. Sel. Areas Commun.*, vol. 30, no. 2, pp. 388–396, Feb. 2012.

- [46] 3GPP T.S. 25.996, *Spatial channel model for multiple input multiple output (MIMO) simulations*, V11.0.0, 2012.
- [47] L. Raschkowski, *et al.*, “METIS Channel Models”. Available: https://www.metis2020.com/wp-content/uploads/deliverables/METIS_D1.4_v1.0.pdf.
- [48] Report ITU-R M.2135-1, “Guidelines for evaluation of radio interface technologies for IMT-Advanced”, 2009.
- [49] A. Kuchar, J. -P. Rossi, and E. Bonek, “Directional macro-cell channel characterization from urban measurements,” *IEEE Trans. Antennas Propag.*, vol. 48, no. 2, pp. 137–146, Feb. 2000.
- [50] H. Hofstetter, A. F. Molisch, and N. Czink, “A twin-cluster MIMO channel model,” in *Proc. IEEE EuCAP’06*, Nice, France, Nov. 2006, pp. 1–8.
- [51] S. Wu, C. -X. Wang, el-H. M. Aggoune, M. M. Alwakeel, and Y. He, “A non-stationary 3-D wideband twin-cluster model for 5G massive MIMO channels,” *IEEE J. Sel. Areas Commun.*, vol. 32, no. 6, pp. 1207–1218, June 2014.
- [52] N. Czink and C. Oestges, “The COST 273 MIMO channel model: three kinds of clusters,” in *Proc. ISSSTA’08*, Bologna, Italy, Aug. 2008, pp. 282–286.
- [53] X. Gao, F. Tufvesson, and O. Edfors, “Massive MIMO channels-measurements and models,” in *Proc. ASILOMAR’13*, Pacific Grove, USA, Nov. 2013, pp. 280–284.
- [54] A. G. Zajić and G. L. Stüber, “Three-dimensional modeling, simulation, and capacity analysis of space-time correlated mobile-to-mobile channels,” *IEEE Trans. Veh. Technol.*, vol. 57, no. 4, pp. 2042–2054, July 2008.
- [55] A. G. Zajić and G. L. Stüber, “Three-dimensional modeling and simulation of wideband MIMO mobile-to-mobile channels,” *IEEE Trans. Wireless Commun.*, vol. 8, no. 3, pp. 1260–1275, Mar. 2009.
- [56] Y. Yuan, C.-X. Wang, X. Cheng, B. Ai, and D. I. Laurenson, “Novel 3D geometry-based stochastic models for non-isotropic MIMO vehicle-to-vehicle

- channels,” *IEEE Trans. Wireless Commun.*, vol. 13, no. 1, pp. 298–309, Jan. 2014.
- [57] Y. Yuan, C. -X. Wang, Y. He, el-H. M. Aggoune, and M. M. Alwakeel, “Novel 3D wideband non-stationary geometry-based stochastic models for non-isotropic MIMO vehicle-to-vehicle channels,” *IEEE Trans. Wireless Commun.*, accepted for publication.
- [58] K. Kalliola, H. Laitinen, P. Vainikainen, M. Toeltsch, J. Laurila, and E. Bonek, “3-D double-directional radio channel characterization for urban macrocellular applications,” *IEEE Trans. Antennas Propag.*, vol. 51, no. 11, pp. 3122–3133, Nov. 2003.
- [59] A. Kammoun, H. Khanfir, Z. Altman, M. Debbah, and M. Kamoun, “Preliminary results on 3D channel modeling: from theory to standardization,” *IEEE J. Sel. Areas Commun.*, vol. 32, no. 6, pp. 1219–1229, June 2014.
- [60] T. A. Thomas, F. W. Vook, E. Visotsky, E. Mellios, G. S. Hilton, and A. R. Nix, “3D Extension of the 3GPP/ITU channel model.” in *Proc. IEEE VTC’13-Spring*, Dresden, Germany, June 2013, pp. 1–5.
- [61] D. S. Baum, J. Hansen, and J. Salo, “An interim channel model for beyond-3G systems: extending the 3GPP spatial channel model (SCM),” in *Proc. IEEE VTC’05 Spring*, vol. 5, Stockholm, Sweden, May 2005, pp. 3132–3136.
- [62] P. Heino, *et al.*, “WINNER+ final channel models”, ver 1.0, June 2010. Available:
http://projects.celtic-initiative.org/winner+/WINNER+%20Deliverables/D5.3_v1.0.pdf.
- [63] 3GPP T.R. 36.814, *Further advancements for E-UTRA physical layer aspects*, V9.0.0, 2010.
- [64] M. Wu, B. Yin, G. Wang, C. Dick, J. R. Cavallaro, and C. Studer, “Large-scale MIMO detection for 3GPP LTE: algorithms and FPGA implementations,” *IEEE J. Sel. Topics Signal Process.*, vol. 8, no. 5, pp. 916–929, Oct. 2014.

- [65] A. A. M. Saleh and R. A. Valenzuela, “A statistical model for indoor multipath propagation,” *IEEE J. Sel. Areas Commun.*, vol. 5, no. 2, pp. 128–137, Feb. 1987.
- [66] A. Maltsev *et al.*, “Channel models for 60 GHz WLAN systems”. Available: <https://mentor.ieee.org/802.11/dcn/09/11-09-0334-06-00ad-channel-models-for-60-ghz-wlan-systems.doc>.
- [67] L. Zheng and D. N. C. Tse, “Diversity and multiplexing: a fundamental trade-off in multiple-antenna channels,” *IEEE Trans. Inf. Theory.*, vol. 49, no. 5, pp. 1073–1096, May 2003.
- [68] S. K. Mohammed and E. G. Larsson, “Per-antenna constant envelope precoding for large multi-user MIMO systems,” *IEEE Trans. Commun.*, vol. 61, no. 3, pp. 1059–1071, Mar. 2013.
- [69] J. Zhang, X. Yuan, and L. Ping, “Hermitian precoding for distributed MIMO systems with individual channel state information,” *IEEE J. Sel. Areas Commun.*, vol. 31, no. 2, pp. 241–250, Feb. 2013.
- [70] R. Couillet and M. Debbah, *Random Matrix Methods for Wireless Communications.*, Cambridge University Press, Cambridge, 2011.
- [71] S. Noh, M. D. Zoltowski, and D. J. Love, “Pilot beam pattern design for channel estimation in massive MIMO systems,” *IEEE J. Sel. Topics in Signal Processing.*, vol. 8, no. 5, pp. 787–801, May 2014.
- [72] R. Couillet, M. Debbah, and J. W. Silverstein, “A deterministic equivalent for the analysis of correlated MIMO multiple access channels,” *IEEE Trans. Inf. Theory*, vol. 57, no. 6, pp. 3493–3514, June 2011.
- [73] G. Taricco, “Asymptotic mutual information statistics of separately correlated Rician fading MIMO channels,” *IEEE Trans. Inf. Theory*, vol. 54, no. 8, pp. 3490–3504, Aug. 2008.

- [74] E. Riegler and G. Taricco, “Asymptotic statistics of the mutual information for spatially correlated Rician fading MIMO channels with interference,” *IEEE Inf. Theory*, vol. 56, no. 4, pp. 1542–1559, Apr. 2010.
- [75] C. K. Wen, S. Jin, and K. K. Wong, “On the sum-rate of multiuser MIMO uplink channels with jointly-correlated Rician fading,” *IEEE Trans. Commun.*, vol. 59, no. 10, pp. 2883–2895, Oct. 2011.
- [76] H. Özcelik, N. Czink, and E. Bonek, “What makes a good MIMO channel model,” in *Proc. VTC’05*, Stockholm, Sweden, May 2005, pp. 156–160.
- [77] V. V. Veeravalli, Y. Liang, and A. M. Sayeed, “Correlated MIMO wireless channels: capacity, optimal signaling, and asymptotics,” *IEEE Inf. Theory*, vol. 51, no. 6, pp. 2058–2072, June 2005.
- [78] A. M. Sayeed, “Deconstructing multiantenna fading channels,” *IEEE Trans. Signal Process.*, vol. 50, no. 10, pp. 2563–2579, Oct. 2002.
- [79] J. Li and Y. Zhao, “Channel characterization and modeling for large-scale antenna systems,” in *Proc. ISCIT’14*, Incheio, Sep. 2014, pp. 559–563.
- [80] X. Gao, O. Edfors, F. Rusek, and F. Tufvesson, “Linear pre-coding performance in measured very-large MIMO channels,” in *Proc. VTC’11-Fall*, San Francisco, USA, Sep. 2011, pp. 1–5.
- [81] J. Hoydis, C. Hoek, T. Wild, and S. ten Brink, “Channel measurements for large antenna arrays,” in *Proc. IEEE ISWCS’12*, Paris, France, Aug. 2012, pp. 811–815.
- [82] C. Shepard, H. Yu, N. Anand, L. E. Li, T. Marzetta, R. Yang, and L. Zhong, “Argos: Practical many-antenna base stations,” in *Proc. ACM Int. Conf. Mobile Computing and Networking*, Aug. 2012.
- [83] A. Bernland and M. Gustafsson, “Estimation of spherical wave coefficients from 3-D positioner channel measurements,” *IEEE Antennas Wireless Propag. Lett.*, vol. 11, pp. 608–611, 2012.

- [84] F. Rusek, O. Edfors, and F. Tufvesson, "Indoor multi-user MIMO: measured user orthogonality and its impact on the choice of coding," in *Proc. EuCAP'12*, Prague, Czech Republic, Mar. 2012, pp. 2289–2293.
- [85] S. Payami and F. Tufvesson, "Delay spread properties in a measured massive MIMO system at 2.6 GHz," in *Proc. PIMRC'13*, London, United Kingdom, Sep. 2013, pp. 53–57.
- [86] X. Gao, O. Edfors, F. Rusek, and F. Tufvesson, "Massive MIMO in real propagation environments," *IEEE Trans. Wireless Commun.*, accepted for publication.
- [87] X. Gao, F. Tufvesson, O. Edfors, and F. Rusek, "Measured propagation characteristics for very-large MIMO at 2.6 GHz," in *Proc. of the 46th Annual Asilomar Conference on Signals, Systems, and Computers*, Pacific Grove, California, USA, Nov. 2012, pp. 295–299.
- [88] C. Y. Chiu, J. B. Yan, and R. D. Murch, "24-port and 36-port antenna cubes suitable for MIMO wireless communications," *IEEE Trans. Antennas Propag.*, vol. 56, no. 4, pp. 1170–1176, Apr. 2008.
- [89] X. Gao, O. Edfors, J. Liu, and F. Tufvesson, "Antenna selection in measured massive MIMO channels using convex optimization," in *Proc. Globecom'13*, Atlanta, USA, Dec. 2013, pp. 129–134.
- [90] J. Vieira, F. Rusek, and F. Tufvesson, "Reciprocity calibration methods for massive MIMO based on antenna coupling," in *Proc. Globecom'14*, Austin, USA, Dec. 2014, pp. 3708–3712.
- [91] J. Vieira, S. Malkowsky, K. Nieman, Z. Miers, N. Kundargi, L. Liu, I. Wong, V. Owall, O. Edfors, and F. Tufvesson, "A flexible 100-antenna testbed for massive MIMO," in *Proc. Globecom'14*, Austin, USA, Dec. 2014, pp. 1–7.
- [92] S. Y. Poon and M. Ho, "Indoor multiple-antenna channel characterization from 2 to 8 GHz," in *Proc. ICC'03*, Anchorage, USA, May, 2003, pp. 3519–3523.

- [93] X. Gao, A. A. Glazunov, J. Weng, C. Fang, J. Zhang, and F. Tufvesson, "Channel measurement and characterization of interference between residential femto-cell systems," in *Proc. EuCAP'11*, Rome, Italy, Apr. 2011, pp. 3769–3773.
- [94] A. A. Glazunov, S. Prasad, and P. Handel, "Experimental characterization of the propagation channel along a very large virtual array in a reverberation chamber," *Progress In Electromagnetics Research B*, vol. 59, pp. 205–217, 2014.
- [95] J. Koivunen, P. Almers, V. M. Kolmonen, J. Salmi, A. Richter, F. Tufvesson, P. Suvikunnas, A. F. Molisch, and P. Vainikainen, "Dynamic multi-link indoor MIMO measurements at 5.3 GHz," in *Proc. EuCAP'07*, Edinburgh, UK, No. 2007, pp. 1–6.
- [96] Z. Pi and F. Khan, "A millimeter-wave massive MIMO system for next generation mobile broadband," in *Proc. ASILOMAR'12*, Pacific Grove, USA, Nov. 2012, pp. 693–698.
- [97] A. D. Yaghjian, "An overview of near-field antenna measurements," *IEEE Trans. Antennas Propag.*, vol. 34, no. 1, pp. 30–45, Jan. 1986.
- [98] J. -S. Jiang and M. A. Ingram, "Spherical-wave model for short-range MIMO," *IEEE Trans. Commun.*, vol. 53, no. 9, pp. 1534–1541, Sep. 2005.
- [99] F. Bohagen, P. Orten, and G. E. Oien, "Modeling of line-of-sight 2x2 MIMO channels spherical versus plane waves," in *Proc. IEEE PIMRC'06*, Helsinki, Finland, Sep. 2006, pp. 1–5.
- [100] T. Zwick, C. Fischer, D. Didascalou, and W. Wiesbeck, "A stochastic spatial channel model based on wave-propagation modeling," *IEEE J. Sel. Areas Commun.*, vol. 18, no. 1, pp. 6–15, Jan. 2000.
- [101] C. C. Chong, C. M. Tan, D. I. Laurenson, S. McLaughlin, and M. A. Beach, "A novel wideband dynamic directional indoor channel model based on a Markov process," *IEEE Trans. Wireless Commun.*, vol. 4, no. 4, pp. 1539–1552, July 2005.

- [102] F. Babich and G. Lombardi, “A Markov model for the mobile propagation channel,” *IEEE Trans. Veh. Technol.*, vol. 48, no. 1, pp. 63–73, Jan. 2000.
- [103] L. Lu, G. Y. Li, A. L. Swindlehurst, A. Ashikhmin, and R. Zhang, “An overview of massive MIMO benefits and challenges,” *IEEE J. Sel. Signal Process.*, vol. 8, no. 5, pp. 742–758, Oct. 2014.
- [104] J. C. Liberti and T. S. Rappaport, “A geometrically based model for line-of-sight multipath radio channels,” in *Proc. IEEE VTC’96*, Atlanta, USA, Apr. 1996, pp. 844–848.
- [105] A. G. Zajić, G. L. Stüber, T. G. Pratt, and S. T. Nguyen, “Wideband MIMO mobile-to-mobile channels: geometry-based statistical modeling with experimental verification,” *IEEE Trans. Veh. Technol.*, vol. 58, no. 2, pp. 517–534, Feb. 2009.
- [106] C.-X. Wang, X. Hong, H. Wu, and W. Xu, “Spatial temporal correlation properties of the 3GPP spatial channel model and the Kronecker MIMO channel model,” *EURASIP J. Wireless Commun. and Networking*, vol. 2007, Article ID 39871, 9 pages, 2007. doi:10.1155/2007/39871.
- [107] C. K. Wen, S. Jin, and K. K. Wong, “On the sum-rate of multiuser MIMO uplink channels with jointly-correlated Rician fading,” *IEEE Trans. Commun.*, vol. 59, no. 10, pp. 2883–2895, Oct. 2011.
- [108] C. A. Balanis, *Antenna Theory Analysis and Design.*, 3rd ed, John Wiley & Sons, New Jersey, 2005.
- [109] S. R. Saunders and A. Aragon-Zavala, *Antennas and Propagation for Wireless Communication Systems.*, 2nd ed, John Wiley & Sons, West Sussex, 2007.
- [110] F. Bohagen, P. Orten, and G. E. Oien, “Design of capacity-optimal high-rank line-of-sight MIMO channels,” Univ. of Oslo, Research Rep. 352, Mar. 2007.
- [111] T. Zwick, C. Fischer, and W. Wiesbeck, “A stochastic multipath channel model including path directions for indoor environments,” *IEEE J. Sel. Areas Commun.*, vol. 20, no. 6, pp. 1178–1192, Aug. 2002.

- [112] H. Xiao, A. G. Burr, and L. Song, "A time-variant wideband spatial channel model based on the 3GPP model," in *Proc. IEEE VTC'06 Fall*, Montreal, Canada, Sep. 2006, pp. 1–5.
- [113] S. Wu, C. -X. Wang, and el-H. Aggoune, "Non-stationary wideband channel models for massive MIMO systems," in *Proc. WSCN'13*, Jeddah, Saudi Arabia, Dec. 2013, pp. 1–8.
- [114] Y. Chen and V. K. Dubey, "Dynamic simulation model of indoor wideband directional channels," *IEEE Trans. Veh. Technol.*, vol. 55, no. 2, pp. 417–430, Mar. 2006.
- [115] A. Papoulis and S. U. Pillai, *Probability, Random Variables, and Stochastic Processes.*, 4th ed, McGraw–Hill, New York, 2002.
- [116] A. Abdi, J. A. Barger, and M. Kaveh, "A parametric model for the distribution of the angle of arrival and the associated correlation function and power spectrum at the mobile station," *IEEE Trans. Veh. Technol.*, vol. 51, no. 3, pp. 425–434, May 2002.
- [117] X. Cheng, Q. Yao, M. Wen, C. -X. Wang, L. Song, and B. Jiao, "Wideband channel modeling and ICI cancellation for vehicle-to-vehicle communication systems," *IEEE J. Sel. Areas Commun.*, vol. 31, no. 9, pp. 434–448, Sep. 2013.
- [118] A. Abdi and M. Kaveh, "A space-time correlation model for multielement antenna systems in mobile fading channels," *IEEE J. Sel. Areas Commun.*, vol. 20, no. 3, pp. 550–560, Apr. 2002.
- [119] L. C. Godara, "Application of antenna arrays to mobile II: beam-forming and direction-of-arrival considerations," in *Proc. of the IEEE.*, vol. 85, no. 8, pp. 1195–1245, Aug. 1997.
- [120] A. F. Molisch, *Wireless Communications.*, 2nd ed, John Wiley & Sons, West Sussex, 2005.

- [121] K. R. Kumar, G. Caire, and A. L. Moustakas, "Asymptotic performance of linear receivers in MIMO fading channels," *IEEE Trans. Inf. Theory*, vol. 55, no. 10, pp. 4398–4418, Oct. 2009.
- [122] X. Hong, C.-X. Wang, B. Allen, and W. Malik, "A correlation based double-directional stochastic channel model for multiple-antenna UWB systems," *IET Microwaves, Antennas and Propagation*, vol. 1, no. 6, pp. 1182–1191, Dec. 2007.
- [123] C.-N. Chuah, D. N. C. Tse, J. M. Kahn, and R. A. Valenzuela, "Capacity scaling in MIMO wireless systems under correlated fading," *IEEE Trans. Inf. Theory*, vol. 48, no. 3, pp. 637–650, Mar. 2002.
- [124] W. Weichselberger, M. Herdin, H. Ozelcelik, and E. Bonek, "A stochastic MIMO channel model with joint correlation of both link ends," *IEEE Trans. Commun.*, vol. 5, no. 1, pp. 90–100, Jan. 2006.
- [125] S. Verdú, "Spectral efficiency in the wideband regime," *IEEE Trans. Inf. Theory*, vol. 48, no. 6, pp. 1319–1343, June 2002.
- [126] G. P. H. Styan, "Hadamard products and multivariate statistical analysis," *Linear Algebra Appl.* 6, pp. 217–240, 1973.
- [127] Z. Yang and X. Feng, "New lower bound of the determinant for Hadamard product on some totally nonnegative matrices," *Springer J. Appl. Math. & Computing.*, vol. 25, no. 1–2, pp. 169–181, 2007.
- [128] S. L. Loyka, "Channel capacity of MIMO architecture using the exponential correlation matrix," *IEEE Commun. Lett.*, vol. 5, no. 9, pp. 369–371, Sep. 2001.
- [129] M. Miranda and P. Tilli, "Asymptotic spectra of Hermitian block Toeplitz matrices and preconditioning results," *SIAM J. Matrix Anal. Appl.*, vol. 21, no. 3, pp. 867–881, Feb. 2000.
- [130] N. Sun and J. Wu, "Maximizing spectral efficiency for high mobility systems with imperfect channel state information," *IEEE Trans. Wireless Commun.*, vol. 13, no. 3, pp. 1462–1470, Mar. 2014.

- [131] J. G. Andrews, S. Buzzi, W. Choi, S. V. Hanly, A. Lozano, A. C. K. Soong, and J. C. Zhang, “What will 5G be?,” *IEEE J. Sel. Areas Commun.*, vol. 32, no. 6, pp. 1065–1082, June 2014.
- [132] K. Zheng, S. Ou, and X. Yin, “Massive MIMO channel models: a survey,” *Hindawi International J. of Antennas and Propagat .*, vol. 2014, Article ID 848071, 10 pages, June 2014.
- [133] P. Stenumgaard, J. Chilo, J. Ferrer-Coll, and P. Ängskog, “Challenges and conditions for wireless machine-to-machine communications in industrial environments,” *IEEE Commun. Mag.*, vol. 51, no. 6, pp. 187–192, June 2013.
- [134] Z. Pi and F. Khan, “An introduction to millimeter-wave mobile broadband systems,” *IEEE Commun. Mag.*, vol. 49, no. 6, pp. 101–107, June 2011.
- [135] T. S. Rappaport, S. Sun, R. Mayzus, H. Zhao, Y. Azar, K. Wang, G. N. Wong, J. K. Schulz, M. Samimi, and F. Gutierrez, “Millimeter wave mobile communications for 5G cellular: it will work!,” *IEEE Access.*, vol. 1, pp. 335–349, May 2013.
- [136] J. Brady, N. Behdad, and A. M. Sayeed, “Beamspace MIMO for millimeter-wave communications: system architecture, modeling, analysis, and measurements,” *IEEE Trans. Antennas Propag.*, vol. 61, no. 7, pp. 3814–3827, July 2013.
- [137] J. Karedal, F. Tufvesson, N. Czink, A. Paier, C. Dumard, T. Zemen, C. F. Mecklenbräuker, and A. F. Molisch, “A geometry-based stochastic MIMO model for vehicle-to-vehicle communications,” *IEEE Trans. Wireless Commun.*, vol. 8, no. 7, pp. 3646–3657, July 2009.
- [138] A. F. Molisch, *et al.*, “IEEE 802.15.4a channel model - final report”. Available: <https://mentor.ieee.org/802.15/dcn/04/15-04-0662-04-004a-channel-model-final-report-r1.pdf>.
- [139] D. Porcino and W. Hirt, “Ultra-wideband radio technology: potential and challenges ahead,” *IEEE Commun. Mag.*, vol. 41, no. 7, pp. 66–74, July 2003.

- [140] A. Fort, J. Ryckaert, C. Desset, P. De Doncker, P. Wambacq, and L. Van Biesen, “Ultra-wideband channel model for communication around the human body,” *IEEE J. Sel. Areas Commun.*, vol. 24, no. 4, pp. 927–933, Apr. 2006.
- [141] A. F. Molisch, J. R. Foerster, and M. Pendergrass, “Channel models for ultrawideband personal area networks,” *IEEE Wireless Commun.*, vol. 10, no. 6, pp. 14–21, Feb. 2004.
- [142] C. Liu, E. Skafidas, T. S. Pollock, and R. J. Evans, “Angle of arrival extended S-V model for the 60 GHz wireless desktop channel,” in *Proc. PIMRC’06.*, Helsinki, Finland, Sep. 2006, pp. 1–6.
- [143] M. R. Akdeniz, Y. Liu, M. K. Samimi, S. Sun, S. Rangan, T. S. Rappaport, and E. Erkip, “Millimeter wave channel modeling and cellular capacity evaluation,” *IEEE J. Sel. Areas Commun.*, vol. 32, no. 6, pp. 1164–1179, June 2014.
- [144] R. He, Z. Zhong, B. Ai, J. Ding, Y. Yang, and A. F. Molisch, “Short-term fading behavior in high-speed railway cutting scenario: measurements, analysis, and statistical model,” *IEEE Trans. Antennas Propag.*, vol. 61, no. 4, pp. 2209–2222, Apr. 2013.
- [145] 3GPP T.R. 36.873, *Study on 3D channel model for LTE*, V2.0.0, 2014.
- [146] T. H. Glisson, Jr., *Introduction to Circuit Analysis and Design.*, Springer, 2011.
- [147] R. S. Elliott, *Antenna Theory and Design: Revised Edition.*, John Wiley & Sons, New Jersey, 2003.